Title
Earthquake Surface Fault Rupture Interaction with Building Foundations

Author
Oettle, Nicolas Karl

Publication Date
2013

Peer reviewed|Thesis/dissertation

Earthquake Surface Fault Rupture Interaction with Building Foundations

By

Nicolas Karl Oettle

A thesis submitted in partial satisfaction of the

requirements for the degree of

Doctor of Philosophy

in

Engineering – Civil and Environmental Engineering

in the

Graduate Division

of the

University of California, Berkeley

Committee in charge:

Professor Jonathan D. Bray, Chair
Professor Raymond B. Seed
Professor Douglas S. Dreger

Fall 2013

Earthquake Surface Fault Rupture Interaction with Building Foundations

by
Nicolas Karl Oettle

Abstract

Earthquake Surface Fault Rupture Interaction with Building Foundations

by

Nicolas Karl Oettle

Doctor of Philosophy in Engineering – Civil and Environmental Engineering

University of California, Berkeley

Professor Jonathan D. Bray, Chair

Recent earthquakes have provided numerous examples of the devastating effects of earthquake surface fault rupture on structures. Several major cities are built in areas containing active faults that can break the ground surface (e.g., Los Angeles, Salt Lake City, San Diego, San Francisco, and Seattle). Along with the often spectacular observations of damage, examples of satisfactory performance of structures were also observed. These examples of satisfactory performance indicate that similar to other forms of ground failure, effective design strategies can be developed to address the hazards associated with surface fault rupture. However, at present, no design guidance exists for implementing many of the potential strategies for building near faults.

To address this issue, a comprehensive set of numerical simulations, which were initially validated with centrifuge test results, has been undertaken to analyze potential design strategies for building in the vicinity of active faults. The numerical simulations capture fully this problem as a soil–structure–fault interaction problem where the influence of the structure has been explicitly included. A modified nonlinear, effective stress, elasto-plastic soil constitutive model has been developed and implemented in an explicit finite-difference framework to capture the soil and structural responses to fault rupture.

For the first time, the effects of prior earthquake ruptures through soil (e.g., pre-existing shear bands and the in situ stress state) were investigated. Additionally, the effects of fault type on soil response was analyzed and was found to be primarily a result of varying stress paths in normal, reverse, and vertical faults. The effects of dynamic soil–fault–structure interaction were analyzed in a systematic manner for the first time and procedures to account for these effects were developed.

Hazard mitigation strategies were developed and systematically evaluated and compared. Three main categories of fault-resistant design were identified: (1) spreading fault displacement over a large area, such as with engineered fill; (2) enabling the structure to respond with rigid-body movement, e.g., by using a stiff mat foundation; and (3) diverting fault rupture through soil using stiff structural elements or by strengthening the foundation soil. These strategies were found to be effective at minimizing structural damage during surface fault rupture events. Their use allows for improved designs and retrofits in the active fault regions, which reduce risk while preserving design flexibility.

TABLE OF CONTENTS

ACKNOWLEDGMENTS

My advisor, Prof. J. Bray, provided the overall direction and many helpful and useful comments throughout the duration of this project which significantly improved this work. Committee members Prof. R. Seed and Prof. D. Dreger provided helpful comments and suggestions throughout the project. Prof. K. Konagai and Mr. K. Kelson collaborated on a case history of surface fault rupture interaction with a structure in Japan; although not included herein, it was helpful in the development of some of the concepts presented in this thesis. A number of UC Berkeley graduate students in the geotechnical engineering program provided review and suggestions for portions of this work. Anonymous reviewers during the journal review process for Chapters 4 and 5 also contributed to the improvement of this research. My mentors, Dr. N. Matasovic and Prof. J. Hanson, contributed significantly to my development prior to coming to UC Berkeley.

I would like to thank Profs. G. Gazetas and I. Anastasopoulos for sharing the results of the centrifuge experiments conducted by Prof. M. Bransby and others as part of their research effort to investigate the effects of surface fault rupture on soil and structures. Further, I would like to thank Prof. P. Byrne and Dr. M. Beaty for sharing their code for UBCSAND and providing insights for its use.

The National Science Foundation (NSF) provided the financial support for this project under Grant CMMI-0926473. The opinions, findings, conclusions, and recommendations expressed herein do not necessarily reflect the views of the NSF.

CHAPTER 1: INTRODUCTION

1.1 Overview

Recent earthquakes have provided numerous examples of the devastating effects of earthquake surface fault rupture on structures. Several major cities are built in areas containing active faults that can break the ground surface (e.g., Los Angeles, Salt Lake City, San Diego, San Francisco, and Seattle). Along with the often spectacular observations of damage, examples of satisfactory performance of structures were also observed. These examples of satisfactory performance indicate that similar to other forms of ground failure, effective design strategies can be developed to address the hazards associated with surface fault rupture. However, at present, no design guidance exists for implementing many of the potential strategies for building near faults. The objective of this thesis is to investigate some of the most promising geotechnical mitigation strategies to develop insights that aid in the evaluation of the surface fault rupture hazard and to improve the available numerical techniques for estimating structural damage from surface fault rupture.

A key to developing a rational design and mitigation framework for this hazard is to understand fully the mechanics involved in the surface fault rupture process. Previous physical and numerical simulations have assumed that the soil deposit had at-rest stress conditions without a weak shear band at critical state or with slicken-sided properties (e.g., Anastasopoulos et al. 2007; Gazetas et al. 2008; Loukidis et al. 2009). This assumption is true for engineered fill placed over a fault, such as in the case of earth dams (Bray et al. 1992) or for the case of young unfaulted soils (as possibly occurred in the 2010 Darfield earthquake). However, most faults are located by excavating trenches and identifying evidence of prior ruptures. The concept that fault-induced ruptures typically follow previous shear rupture zones is a well-known concept (e.g., Sibson 1977), and most faults have ruptured multiple times. The analogous effect in unconsolidated sediment, however, has not been explored fully.

The prevailing strategy for mitigating the surface fault rupture hazard is to avoid building on or near active fault traces (Bryant 2010). However, in certain cases, this may be difficult to achieve, and sometimes when the amount of fault displacement is relatively minor, it may be unnecessary. Structures can be built safely on or near active faults when the hazard is well defined and manageable and the structure is designed appropriately (e.g., Cluff et al. 2003; Johansson and Konagai 2006; Gazetas et al. 2008; Bray 2009). In fact, several projects have been completed in active fault zones. A residential development in Southern California was designed utilizing numerical simulations to establish rational setback locations and mechanically stabilized soil in combination with post-tensioned mats to mitigate damage from anticipated bedrock fault rupture offsets of 3 cm (Bray 2001). The California Memorial Stadium, which is situated on top of the Hayward Fault, was recently retrofitted using “fault sliding blocks” to accommodate a design strike-slip fault movement on the order of 2 m (Vignos et al. 2009).

There many other cases where geologists and engineers have worked together to identify and characterize surface faulting and to apply sound engineering principles in developing robust designs that mitigate the hazards associated with surface faulting. Surface fault rupture is a ground deformation hazard that can be mitigated geotechnically and structurally by employing

design strategies that are routinely applied to address other ground deformation hazards, such as mining subsidence, landsliding, lateral spreading, and expansive soils.

Lastly, the effect of dynamically applied fault motion on calculating permanent ground deformation has not generally been investigated by previous researchers using either physical or numerical techniques. That is, analysis of soil–structure–fault interaction has generally been conducted pseudostatically. Yet permanent fault movement occurs quite rapidly. In fact, studies have indicated that the average velocity over which permanent fault offset occurs can be on the order of 0.5 to 1.0 m/s (Dreger et al. 2011; Abrahamson 2001; Somerville et al. 1999). Further, damage to the structure from the vibratory component of ground shaking has typically been considered separately from structural loads resulting from permanent ground deformation. This is a "decoupled" approach. This decoupling approach has been studied by Goel and Chopra (2009a,b) and was shown to be a reasonable approximation. The decoupled approach was therefore used throughout this thesis.

1.2 Scope

The scope of this thesis has two main constraints: the analytical work assumes some amount of sandy soil overlies a fault in bedrock and the only types of faults considered are dip-slip faults. Sandy soil is used because the majority of physical model testing completed to date has been done for sand. Dip-slip faults are analyzed because they form plane-strain problems and do not require three-dimensional analysis. Strike-slip faults would require three-dimensional analysis. Further, limited physical testing has been completed for them.

1.3 Organization

This thesis is organized as follows: Chapter 2 provides a review of relevant literature on the subject. Lazarte (1996) conducted a similar literature review; therefore, only research published since that time is included in Chapter 2. Chapter 3 covers the development and validation of numerical analysis procedures used herein for modeling surface fault rupture interaction with structures. Centrifuge test data are compared against results of the numerical model. Insights on the soil mechanics of surface fault rupture are presented. Chapter 4 develops a numerical model that accounts for the effects of prior earthquake ruptures (e.g., pre-existing shear bands and the in-situ soil stress state). The effect of fault type and stress path on soil response is also analyzed.

Chapter 5 analyzes potential hazard mitigation strategies. Fault-resistant design strategies are categorized into three main types: (1) spreading fault displacement over a large area using engineered fill; (2) prompting the structure to respond with rigid-body movement, e.g., by using a stiff mat foundation; and (3) diverting fault rupture through soil using stiff structural elements or by strengthening the foundation soil. A number of such strategies are analyzed for their capacity to allow for safe developments and retrofits in fault zones. Chapter 6 evaluates the potential effect of conducting a fully dynamic analysis rather than a pseudostatic analysis of soil–structure–fault interaction. Procedures are developed to reasonably account for such dynamic effects. Chapter 7 provides a summary of the conclusions from this thesis.

CHAPTER 2: LITERATURE REVIEW

2.1 Introduction

A significant amount of research has been conducted since the literature review of Lazarte (1996) on surface fault rupture, soil–fault–structure interaction, field performance of structures in fault zones, and engineering design of structures near faults. A summary will be presented here of relevant literature published after Lazarte (1996) on topics relevant to this thesis. This review will include laboratory test data, field case histories, numerical modeling of fault rupture, and engineering strategies for addressing the hazards associated with surface fault rupture.

2.2 Existing Laboratory Test Data

Relevant experimental work performed to provide insights on the surface fault rupture hazard since Lazarte (1996) is a series of centrifuge tests of normal and reverse fault rupture conducted by Bransby (2008a and 2008b). Figure 2-1 shows the general layout of these tests. Baseline free-field conditions were tested for both normal and reverse faults. These baseline configurations were then modified by adding a relatively rigid steel strip plate on top of the ground surface to represent a structure with a shallow foundation near the expected fault rupture plane. A series of additional tests were then conducted to assess the effects of changing a single aspect of the structural configuration.

These tests for both normal and reverse faults were conducted on Fontainebleau Sand (Bransby et al., 2008a,b). The properties of Fontainebleau Sand estimated by Bransby et al. (2008a) are reported in Table 2-1. The sand was prepared dry by pluviation to a relative density of approximately 60% (which is equivalent to a dry unit weight of 15.7 kN/m^3).

Data from the centrifuge tests was captured primarily by digital camera and interpreted using the computer software Geo-PIV. Bransby (2008a and 2008b) conducted a total of twelve centrifuge tests, half reverse fault and half normal fault (some duplicate free-field cases were also conducted). The parameters of each test are provided below in Table 2-2 and Table 2-3 for reverse and normal fault tests, respectively. The variable test conditions include free field, baseline foundation, lighter foundation, wider foundation, flexible foundation, and different foundation locations. All of the tests were conducted with a fault dip angle of 60° at the bedrock level.

Results of the centrifuge tests indicate that shallow foundations with large loadings can affect the fault propagation through sand by “moving” the fault slip plane away from the free-field location. Lightly loaded foundations rotated and developed a large “gap” underneath the foundation due to fault offset while heavier foundations tilted less significantly. Moving the foundation significantly affected the soil–structure interaction. A wider foundation caused the fault movement to be spread throughout the structure and prevented significant fault diversion. A flexible foundation caused less fault diversion to occur.

Another set of centrifuge tests were also conducted on deep foundations (Loli et al. 2011, 2012). In these centrifuge tests, two experiments were performed with caisson foundations, one for a normal fault and one for a reverse fault. The caisson foundation significantly diverted the

fault rupture due to its increased rigidity. The foundation blocked and diverted much of the fault rupture but still rotated significantly itself.

2.3 Existing Data from Field Case Histories

Several earthquakes have produced surface fault rupture since the literature review of Lazarte (1996). The characteristics of many of these surface fault rupture events have been documented in the literature. Additionally, some older events have been investigated further recently. A summary of the available literature is provided in Table 2-4. A brief synopsis of the available data and key observations is made for each surface fault rupture event.

1906 San Francisco, California Earthquake

The 1906 San Francisco Earthquake ruptured more than 370 km along the San Andreas Fault (Bray and Kelson, 2006). Typical surface manifestation at the main fault trace was one of three phenomenon: (i) "mole tracking" where local uplift occurred; (ii) "trench phase" where local subsidence occurred; and (iii) "echelon phase" where neither uplift nor subsidence occurred but non-intersecting cracks approximately 45° from the fault line were observed. "Echelon phase" was observed exclusively in wet alluvium. Figure 2-2 shows examples of primary surface rupturing along linear fault strands from the 1906 Earthquake and the 1999 Kocaeli Earthquake for comparison. The primary fault rupture zones were typically on the order of several meters wide.

Prevalent secondary faulting and warping was observed (Bray and Kelson 2006). On the order of one-half of the total lateral displacement was observed to take place outside the narrow, main fault strand. Measurements of the fault displacement distribution were made from tree lines, fences, and roads at multiple points along the 1906 rupture. Data from two such points are reproduced in Figure 2-3. In general, secondary displacement occurred on both sides of the fault; however, displacement was observed to concentrate on one side of the fault at certain locations. Evidence of secondary lateral displacement was observed at up to several hundred meters away from the primary fault strand including a 670 m-wide fault zone observed near San Andreas Lake. Evidence of surfacing faulting could be easily identified in cohesive marsh deposits but evidence of fault rupture was difficult to detect in sand dune deposits.

The effects of secondary fault rupture on structures, and possibly vice-a-versa, are illustrated by the damage to the forebay structure shown in Figure 2-4 (Bray and Kelson 2006). The circular, brick forebay rested just adjacent to the primary fault strand, but nevertheless, was pulled into a more oval shape and heavily damaged by the earthquake. The extension and deformation of the forebay may have been caused by warping of the near fault ground. Furthermore, it would appear that secondary fault ruptures tended to propagate around the perimeter of well-built reinforced concrete structure, as shown in Figure 2-4.

1939 Erzincan, Turkey Earthquake

The 1939 Erzincan, Turkey Earthquake occurred as an M_w 7.8 along the North Anatolian Fault Zone (Gursoy et al. 2012). Strike-slip movement of about 1.5 to 7.5 m of fault movement

was observed with 0.5 to 2.0 m of vertical movement. Data for this event are presented in Figure 2-5. Additional information on rupture along this fault is presented in Fraser et al. (2012).

1992 Landers, California Earthquake

The 1992 Landers Earthquake (M_w 7.3, strike-slip) produced well-defined surface fault rupture. The fault crossed several residences producing damage in some and leaving others intact (Murbach et al. 1999). The extent of secondary ruptures was observed to be narrow in areas of shallow soil deposits and greater in areas of deeper alluvium.

Trenches were constructed near structures affected by the 1992 Landers Earthquake (Murbach et al. 1999). The authors found it difficult to identify the shear zone in the trench even where the fault line was clearly visible on the surface. The authors used a number of techniques including trench cleaning, curing, brushing, blowing, and ultraviolet light over a period of several months to try to identify the shear zones.

Eventually, the shear zones were identified as shown in Figure 2-6 for the Lannom Residence. In this area, depth to bedrock was approximately 15 m and the soil was mostly silty-sand alluvium. The shear zones were observed to widen from the base of the trench to the ground surface, i.e., a "flower" or splaying structure.

1999 Kocaeli, Turkey Earthquake

The Kocaeli Earthquake was largely a strike-slip event, but normal faulting was also observed at a number of step-overs. The fault interacted with many structures and, as a result, a number of investigators documented and analyzed many of the cases of fault–structure interaction in this earthquake (e.g., Faccioli et al. 2008; Anastasopoulos and Gazetas 2007a,b).

Highlights of some of the available case histories are provided in Anastasopoulos and Gazetas (2007a). Trench and boring data are available for some of these case histories. A majority of the available data relates to cases of soil–structure interaction near Golcuk, Turkey. Some of the buildings near the fault rupture are shown in Figure 2-7. Back calculations some of these events have been conducted (Anastasopoulos and Gazetas 2007b). Figure 2-8 shows the numerical models used for five of the case histories presented in Anastasopoulos and Gazetas (2007b). Reasonable agreement between the numerical model and field observations were obtained. These cases illustrate the effects of structure and foundation type on the performance of engineered facilities in the vicinity of a surface rupture.

1999 Duzce, Turkey Earthquake

The 1999 Duzce Earthquake followed the Kocaeli Earthquake by approximately 3 months (Ulusay et al. 2001). The surface rupture from the Duzce Earthquake largely passed through rural areas and therefore did not intersect as many buildings as the Kocaeli Earthquake. However, a number of smaller buildings and other types of infrastructure (e.g., pipes, roads) crossed the fault.

Major damage occurred on the Bolu Viaduct, a major bridge crossing the fault. The bridge shortened by approximately 1.5 m as a result of fault movement (Priestley and Calvi

2002). Shear keys were found to have been critical in preventing the collapse of the bridge during the earthquake (Park et al. 2004).

1999 Chi-Chi, Taiwan Earthquake

The 1999 Chi-Chi Earthquake produced large amounts of reverse surface fault rupture (1 to 4 m). Many structures for human occupancy intersected the main rupture of the causative fault for this earthquake (e.g., Anastaspolouos and Gazetas 2007; Lettis et al. 2000b; Dong et al. 2004). Three examples of structural damage from fault rupture during this earthquake are provided below in Figure 2-9 to Figure 2-11. Back calculations of some of the structures impacted by fault rupture were documented in Faccioli et al. (2008).

Several surveys were conducted across the fault in alluvial settings. Variable rupture responses at the ground surface were recorded. In one location, very broad ground deformation was observed (over 100 m wide). The ground was especially deformed on the hanging wall, as shown in Figure 2-12, with limited deformation on the footwall side of the fault. At this site, discrete fault ruptures at the ground surface tended to developed on the edges of structures situated in the hanging wall deformation zone, as shown in Figure 2-12. At other sites along this fault rupture, complicated fault rupture was observed including sites with multiple fault traces and two cases where a "hump" in the ground surface was recorded (Kelson et al. 2001a,b). However, at most locations along the fault, relatively simple, narrow deformation zones were observed (with zones tens of meters wide).

1999 Hector Mine, California Earthquake

The Hector Mine Earthquake caused fault deformation not only on the causative fault, but also on adjacent faults (Fialko et al. 2002). These movements on nearby faults were attributed to elastic deformations due to static Coulomb stress change caused by the Hector Mine Earthquake. The authors attribute the deformation concentrated in previously existing fault zones to be due to the reduced elastic modulus in these zones relative to adjacent intact rock.

2002 Denali, Alaska Earthquake

The M_w 7.9 Denali Earthquake ruptured long portions of the Denali Fault. This rupture largely occurred in the free-field (Koehler et al. 2011). However, the earthquake also ruptured across the Trans-Alaska Pipeline, which was designed to accommodate surface fault rupture (Cluff et al. 2003; Sorensen and Meyer 2003). The pipeline was built on steel–Teflon shoes designed to slide over concrete grade beams in the event of fault rupture. The pipeline configuration is shown in Figure 2-13. The pipeline performed as designed during the earthquake with strike-slip fault movement on the order of 5.5 m and vertical movement on the order of 0.8 m. The zone over which the deformation occurred was approximately 200 m wide. Alluvium at the site was estimated to be at least 100 m thick. The precise location of the fault was not known beforehand due to active erosion and deposition of the alluvium.

2004 Parkfield, California Earthquake

Surface fault rupture during the 2004 Parkfield Earthquake was largely expressed as an increased rate of creep after the earthquake rather than as co-seismic deformation. Since this fault was well instrumented, a significant amount of data is available for this event including continuous GPS and a number of alignment arrays. The amount of surface slip recorded along the length of the fault is shown in Figure 2-14 as a function of time.

2008 Wenchuan, China Earthquake

Surface fault rupture interacted with several buildings during the 2008 Wenchuan Earthquake (e.g., Ran et al. 2010). Zhou et al. (2010) reports that buildings that were directly on top of the fault either collapsed or were "partially destroyed." One building that narrowly avoided the main scarp is shown in Figure 2-15. Estimations of the slip that occurred along the fault were made with InSAR, GPS, and field data (Tong et al. 2010).

2010 Darfield, New Zealand Earthquake

The 2010 Darfield, New Zealand Earthquake caused a large amount of surface fault movement on a previously unknown fault (Van Dissen et al. 2011; Quigley et al. 2011; Barrell et al. 2011; Villamor et al. 2012; Duffy et al. 2013; Van Dissen et al. 2013). The surface rupture occurred in an area of young, unfaulted soil. The fault interacted at several locations with small buildings including the structure shown in Figure 2-18. No collapsed buildings were reported.

Surface deformation did intersect more than 100 fences, roads, power lines, and similar linear features. This allowed for careful documentation of the fault displacement and distribution of fault movement at these locations (e.g., Barrell et al. 2011; Duffy et al. 2013; Van Dissen et al. 2013). Deformation away from the fault was distributed over a 30 to 300 m zone. Off-fault deformation was distributed over a greater distance at fault step-overs. The off-fault deformation observed along the Darfield Fault trace was at least partly attributed to the relatively deep soil deposits along the fault which consisted of up to 0.5 km of Quaternary gravel deposits with loose gravel near the surface (Van Dissen et al. 2013).

Recommendations for estimating future off-fault deformation were developed based upon observations during the Darfield Earthquake (Van Dissen et al. 2013). These steps consisted of (1) estimating the primary fault rupture displacement; (2) determine whether a step-over is expected at the site of interest; (3) estimate whether distributed deformation is expected based upon near surface soil conditions; (4) use curves based on the Darfield Earthquake data to estimate expected off-fault deformation (Van Dissen et al. 2013).

2010 Yushu, China Earthquake

An M_w 6.9 strike-slip event occurred on 14 April 2010 in the Tibetan Plateau. The fault rupture consisted mostly of free-field response. This surface fault rupture event is documented in Lin et al. (2011) and Tobita et al. (2011).

11 April 2011 Aftershock of the Great Tohoku, Japan Earthquake

An M_w 6.6 aftershock of the Great Tohoku Earthquake with surface fault rupture occurred on 11 April 2011, exactly one month after the main shock (GEER 2011). Nearly vertical surface rupture was observed with displacements on the order of 0.8 to 2.3 m. The surface fault rupture intersected several structures, including a middle school gymnasium and a pool. The affected structures did not collapse but were damaged by the underlying ground movement. Free-field rupture from this earthquake is shown in Figure 2-19. A comprehensive record of the amount of surface deformation along the strike of the fault is provided by Kelson et al. (2012).

The fault was typically localized in a narrow fault zone for much of its length, but on the top of a ridge, the fault did not rupture the ground surface but instead caused very broad deformation to occur (GEER 2011). This change in surface expression was attributed to diffusion through the near surface soil (Oettle et al. 2013).

Chihshang Fault, Taiwan

Some data (boreholes, trenches, and survey data) were collected for a creeping fault cutting through gravelly alluvium in Taiwan (Mu et al. 2011). In certain areas, the fault branched into several surface breaks. These breaks were interpreted by the authors to have occurred within the shallow (roughly 100 m deep) alluvium. Figure 2-20 reproduces the interpreted cross section where branching occurred.

2.4 Previous Numerical Modeling Efforts

Numerical modeling of surface fault rupture through soil and its interaction with structures has been performed by several researchers and documented in numerous publications. Most of these numerical models are described in the literature reviews of Bray (1989) and Lazarte (1996). Since then, the most important numerical modeling of surface fault rupture has been completed by a group of researchers at the National Technical University of Athens (e.g., Anastasopoulos et al. 2007).

Anastasopoulos et al. (2007) used an elasto-plastic Mohr-Coulomb based constitutive model with straining softening. Strain softening was implemented by decreasing the mobilized friction angle with the accumulation of plastic shear strain. This modeling was implemented in ABAQUS using a user-defined constitutive model. Because strain softening causes analysis results to be dependent on the size of the mesh, Anastasopoulos et al. (2007) attempted to adjust their model parameters to roughly account for some of the limitations caused by mesh dependency. They accomplished this by adjusting the plastic strain over which an element will become fully softened based on the size of the mesh. Anastasopoulos et al. (2008a) added elastic beam elements to the model to simulate the effects of buildings with mat foundations. Strip foundations were analyzed in Anastasopoulos et al. (2009), bridges with deep foundations in Anastasopoulos et al. (2008b), and caissons in Loli et al. (2011, 2012).

Another group of researchers at the Univeristy of Patras also performed numerical analysis of surface fault rupture (e.g., Athanasopoulos et al. 2007). Their model consisted of an elasto-plastic constitutive model with a Mohr-Coulomb failure criterion. This model was

implemented in PLAXIS. Mat foundations were included in their numerical simulations. Athanasopoulos (2009) argued that strain softening was not necessary to model surface fault rupture because adequate results for many aspects of surface fault rupture can be achieved with an elastic-perfectly plastic model. Most other researchers would disagree with this assessment (e.g., Bray et al. 1994).

Another team of researchers (Loukidis et al. 2009) employed a constitutive model in FLAC which allow for elasto-plastic soil response with a Mohr-Coulomb failure surface and strain softening. Bray (2001) used the programs GeoFEAP and SSCOMPPC with the Duncan et al. (1980) hyperbolic model to evaluate mitigation strategies for a project site in Ventura County, California. The model included geogrids to form ductile engineered fills.

2.5 Previous Research on Surface Fault Rupture Mitigation for Buildings

The prevailing strategy for mitigating surface fault rupture is to avoid building on or near active fault traces (Bryant 2010). However, in certain cases, this may be difficult to achieve, and sometimes when the amount of fault displacement is relatively minor, it may be unnecessary. Surface fault rupture is a ground deformation hazard that can be mitigated geotechnically and structurally by employing design strategies that are routinely applied to address other ground deformation hazards, such as mining subsidence, land sliding, lateral spreading, and expansive soils. Structures can be built safely on or near active faults when the hazard is well defined and manageable and the structure is designed appropriately (e.g., Cluff et al. 2003; Johansson and Konagai 2006; Gazetas et al. 2008; Bray 2009).

Recent studies have directly modeled the response of structures to fault rupture propagation through soil deposits. For example, using the same soil constitutive models that were employed in the free-field analyses, Anastasopoulos et al. (2008a) included structures by adding structural elements with a specified stiffness and surcharge pressure at the ground surface. Their numerical simulations replicated reasonably well the results of the centrifuge tests conducted by Bransby et al. (2008a,b).

These studies, and previous studies, have led to several recommendations regarding the design of structures near or on active faults. They include the use of non-arbitrary setbacks (Bray 2001), mechanically stabilized earth fills beneath structures (Bray et al. 1993), decoupling slip layers beneath foundation elements (Bray 2001), strong basement walls (Duncan and Lefebvre 1973), strong mat-type foundations (Bray 2001; Gazetas et al. 2008), building weight to divert or diffuse fault movement (Berrill 1983; Gazetas et al. 2008), and simply-supported bridge spans (Gazetas et al. 2008; see also Goel and Chopra 2009a,b).

In fact, several projects have been completed in active fault zones. A residential development in Southern California was designed utilizing numerical simulations to establish rational setback locations and mechanically stabilized soil in combination with post-tensioned mats to mitigate damage from anticipated minor bedrock fault rupture offsets of 3 cm (Bray 2001). The California Memorial Stadium, which is situated on top of the Hayward Fault, was recently retrofitted using “fault sliding blocks” to accommodate a design strike-slip fault movement on the order of 2 m (Vignos et al. 2009).

However, comprehensive investigations of the response of structures to surface fault rupture are limited, and additional work in this relatively novel field of study is warranted.

Specifically, the effectiveness of geotechnical mitigation strategies has not yet been assessed comprehensively for realistic structures. This is the primary aim of this study.

Table 2-1. Properties of Fontainebleau Sand (Bransby et al., 2008ab).

Material Parameter	**Parameter Value**
D_{50}	0.3 mm
Maximum Density	1703 kg/m^3
Minimum Density	1440 kg/m^3
Critical Effective Friction Angle	30.2°
Peak Effective Friction Angle	35°
Dilation Angle	6° (at normal stress of 200 kPa)

Table 2-2. Test configurations for reverse fault tests conducted in Bransby et al. (2008b).

Test Identifier	**Footing Width (B)**	**Bearing Pressure**	**Relative Density**	**Fault Position s, (s/B)**
28	-	-	60.8%	-
29	10 m	91 kPa	64.0%	5.9 m (0.59)
30	10 m	37 kPa	72.0%	5.9 m (0.59)
19	10 m	91 kPa	61.6%	0.8 m (0.08)
21	15 m	91 kPa	60.8%	8.28 m (0.55)
23	9.43 m, flexible foundation	91 kPa	60.3%	5.9 m (0.59)

B and *s* as defined in Figure 2-1a

Table 2-3. Test configurations for normal fault tests conducted in Bransby et al. (2008a).

Test Identifier	**Footing Width (B)**	**Bearing Pressure**	**Relative Density**	**Fault Position s, (s/B)**
12	-	-	60.2%	-
14	10 m	91 kPa	62.5%	3.0 m (0.3)
15	10 m	37 kPa	59.2%	3.1 m (0.31)
18	10 m	91 kPa	63.7%	8.5 m (0.85)
20	25 m	91 kPa	56.0%	10.9 m (0.44)
22	9.43 m, flexible foundation	91 kPa	55.7%	3.2 m (0.34)

B and *s* as defined in Figure 2-1a

Table 2-4. Summary of available surface fault rupture field reconnaissance data published since Lazarte (1996).

Earthquake	M_w	Fault Type	Approx. Movement	Structural Interaction
1906 San Francisco, CA[a]	7.9	SS	2.5-4.5 m	Yes
1939 Erzincan, Turkey[b]	7.8	SS	1.5-7.5 m (0.5-2.0 vert.)	No
1989 Afar Sequence, Ethiopa and Djibouti[c]	5.5-6.3	Normal	30 cm	No
1999 Kocaeli, Turkey[d]	7.5	SS and Normal (at step overs)	1-5 m (SS) 2.5 m (normal)	Yes
1999 Duzce, Turkey[e]	7.1	SS		Yes
1999 Chi Chi, Taiwan[f]	7.6	Reverse	1-4 m	Yes
1999 Hector Mine, California[g]	7.1	SS	mm to cm on adjacent faults	No
2001 El Salvador[h]	6.6	SS	0.4 m	Yes
2002 Denali, Alaska[i]	7.9	SS	2-9 m	No
2004 Parkfield, California[j]	6.0	SS	30-35 cm (as creep)	No
2008 Wenchuan, China[k]	7.9	Reverse	4-9 m	Yes
2009 L'Aquila, Italy[l]	6.3	Normal	10 cm	Yes
2010 Darfield, New Zealand[m]	7.1	SS	2.5 m	Yes
2010 Yushu, China[n]	6.9	SS	1-2 m	No
2010 El Mayor-Cucapah, Mexico[o]	7.2	SS	1-4 m	No
2011 April 11 Aftershock of Tohoku, Japan[p]	6.6	Normal	0.0-2.3 m	Yes

[a] Bray and Kelson 2006

[b] Gursoy et al. 2012; Fraser et al. 2012

[c] Jacques et al. 2011

[d] Ulusay et al. 2000; Lettis et al. 2000a,b; Lettis et al. 2002; Anastasolouos and Gazetas 2007a; Anastasolouos and Gazetas 2007a; Faccioli et al. 2008; Gasperini et al. 2011

[e] Ulusay et al. 2000; Faccioli et al. 2008

[f] Dong et al. 2004; Kelson et al. 2001a,b; Faccioli et al. 2008; Priestley and Calvi 2002; Park et al. 2004

[g] Fialko et al. 2002; Vidale and Li 2003

[h] Canora et al. 2010

[i] Koehler et al. 2010; Cluff et al. 2003; Sorensen and Meyer 2003

[j] Lienkaemper et al. 2006

[k] Zhou et al. 2010; Ran et al. 2010; Du et al. 2012

[l] Guerrieri et al. 2010

[m] Barrell et al. 2011; Quigley et al. 2011; Van Dissen et al. 2011; Villamor et al. 2012; Duffy et al. 2013

[n] Lin et al. 2011; Tobita et al. 2011

[o] GEER 2010; Oskin et al. 2012

[p] GEER 2011; Kelson et al. 2012; Oettle et al. 2013

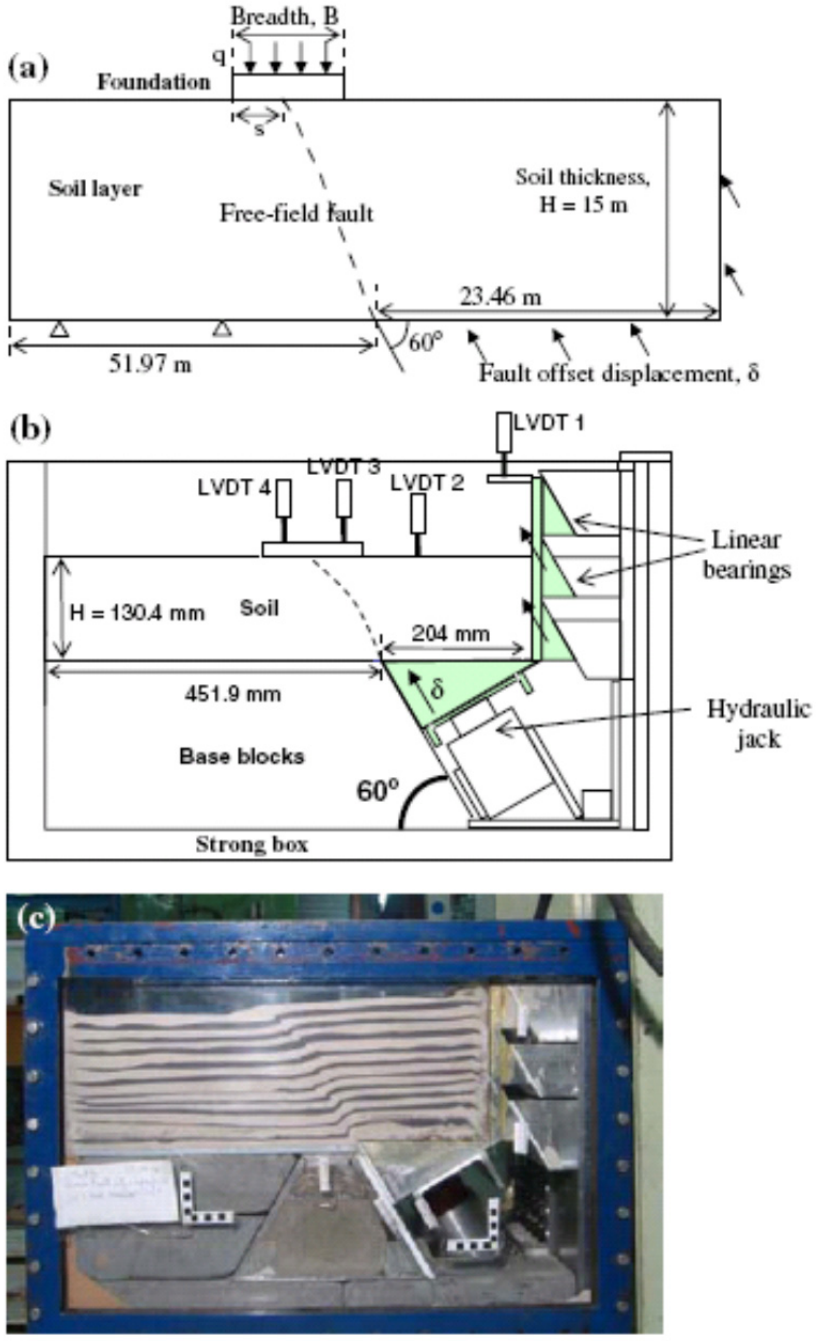

Figure 2-1. The configuration of centrifuge tests conducted in Bransby et al. (2008a,b): (a) schematic of the test geometry; (b) schematic of the centrifuge box; and (c) photograph of a reverse fault test (Bransby et al. 2008a).

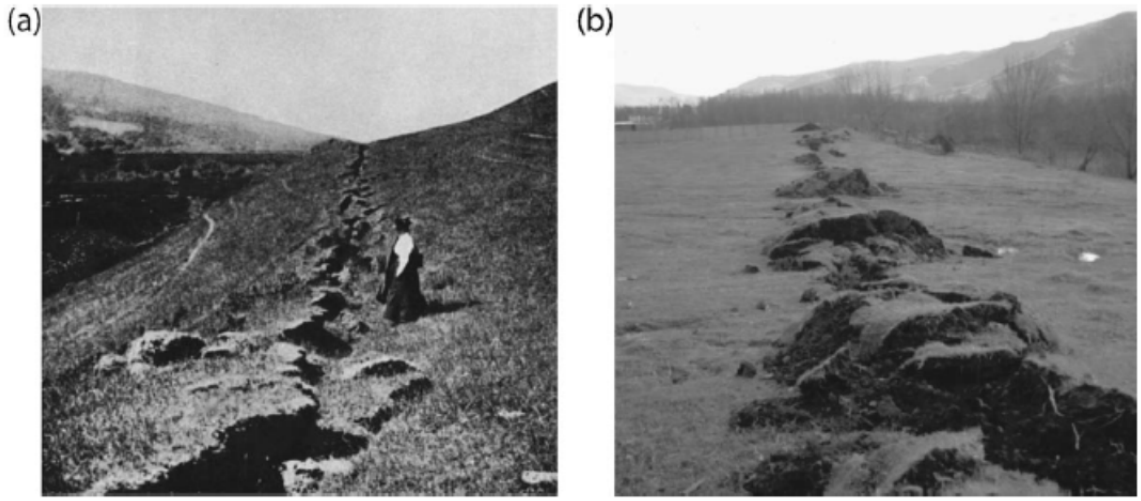

Figure 2-2. Relatively narrow zones of primary fault rupture: (a) the 1906 San Francisco Earthquake; and (b) the 1999 Kocaeli Earthquake (Bray and Kelson 2006).

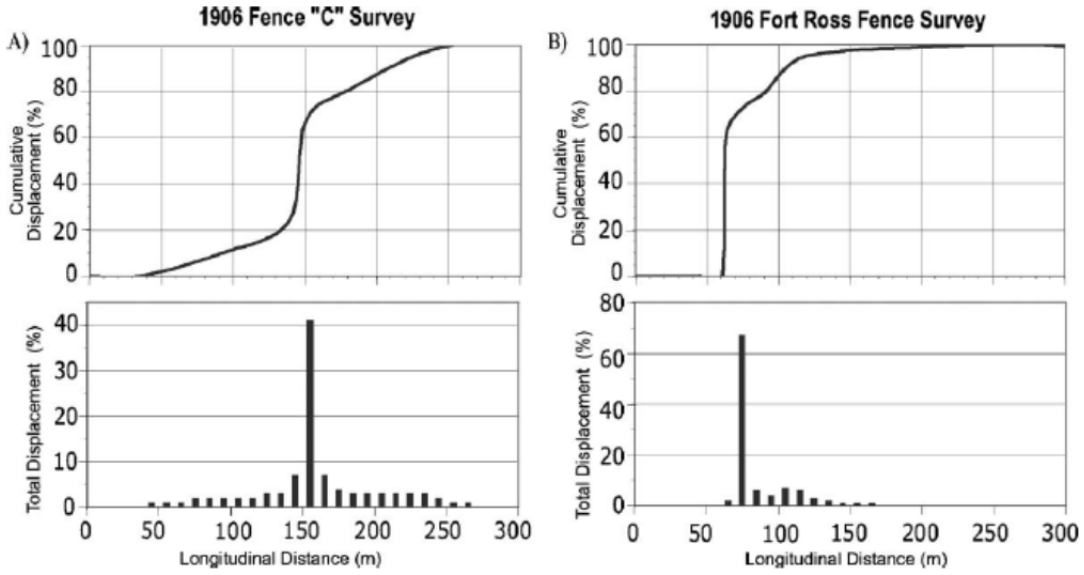

Figure 2-3. Measured distribution of lateral displacement along two sections of the San Andreas Fault in the 1906 San Francisco Earthquake (Bray and Kelson 2006).

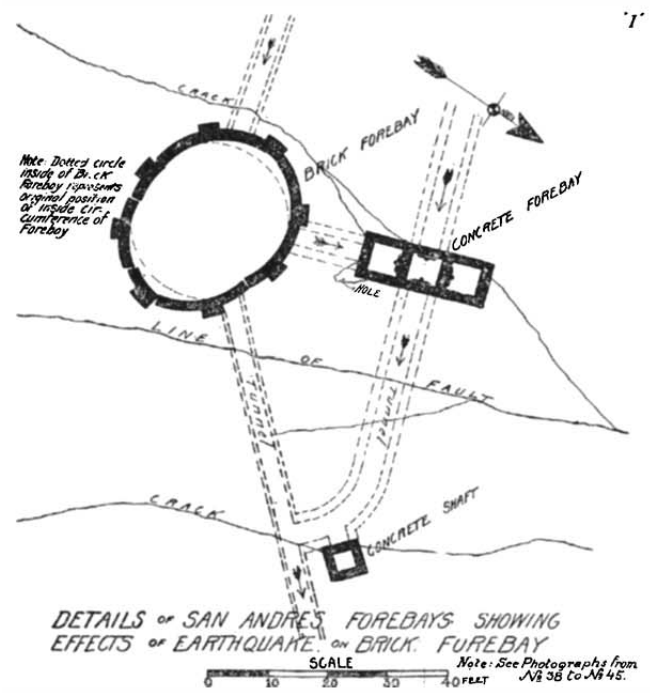

(a)

(b)

Figure 2-4. Fault rupture damages structures during the 1906 San Francisco Earthquake: (a) Plan view of the brick and concrete structures; and (b) the deformed brick forebay (Bray and Kelson 2006).

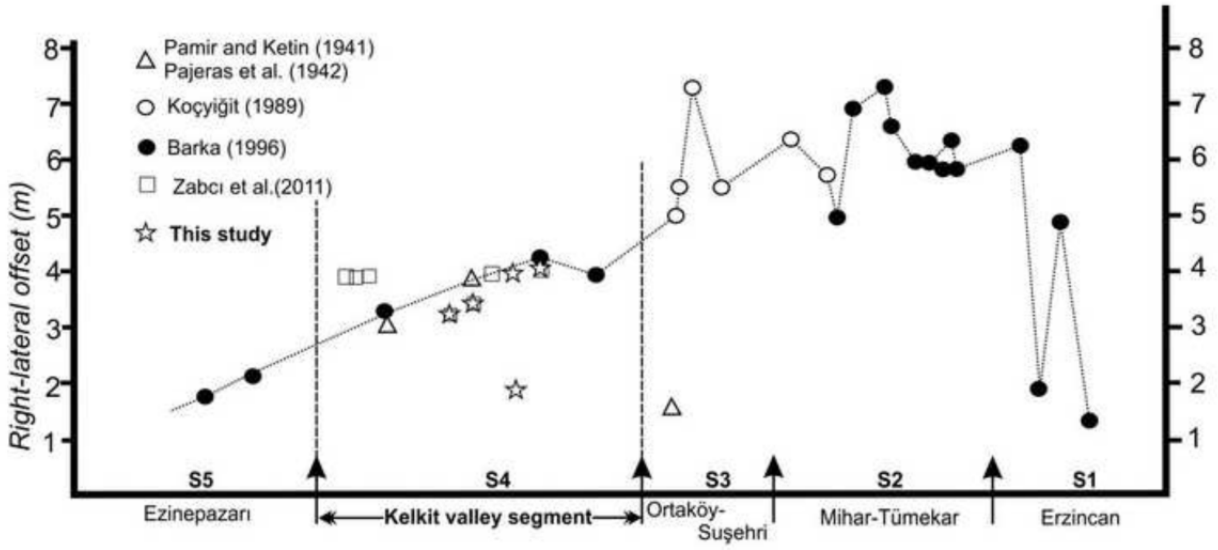

Figure 2-5. Surface fault displacement measured for the 1939 Erzincan event (Gursoy et al. 2012).

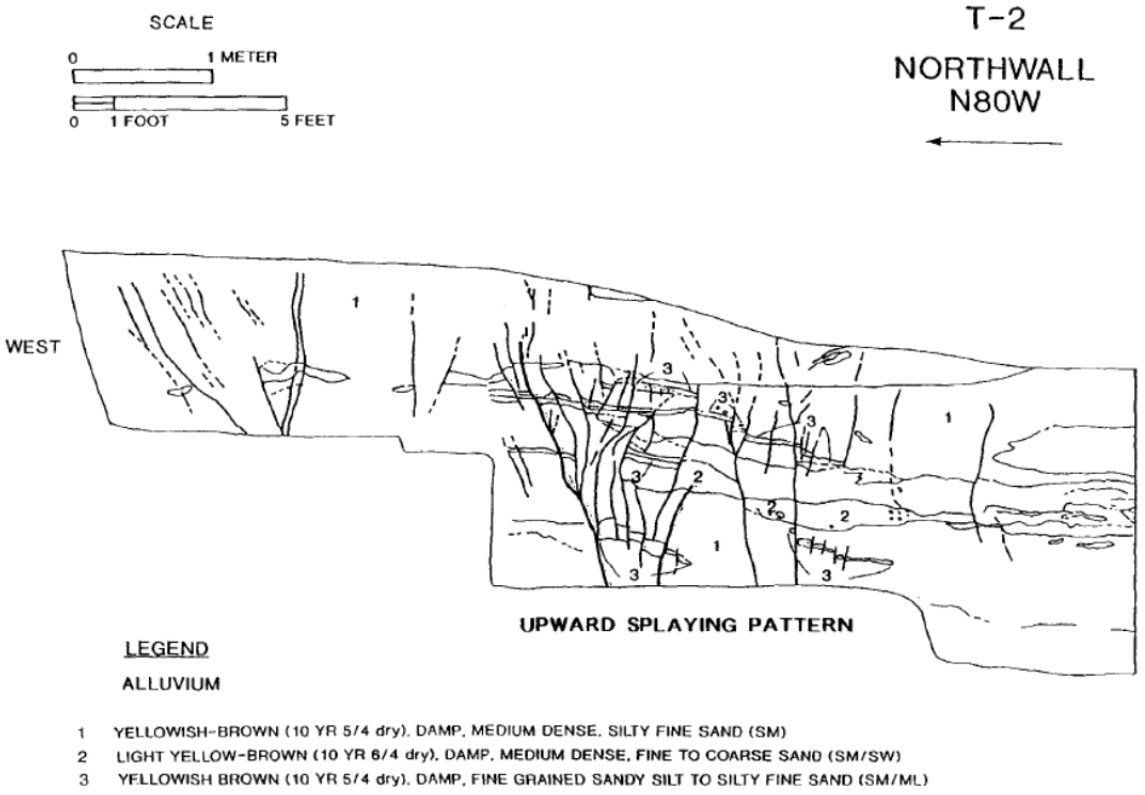

Figure 2-6. Propagation of strike-slip fault rupture in silty-sand alluvium at the Lannom Residence (Murbach et al. 1999).

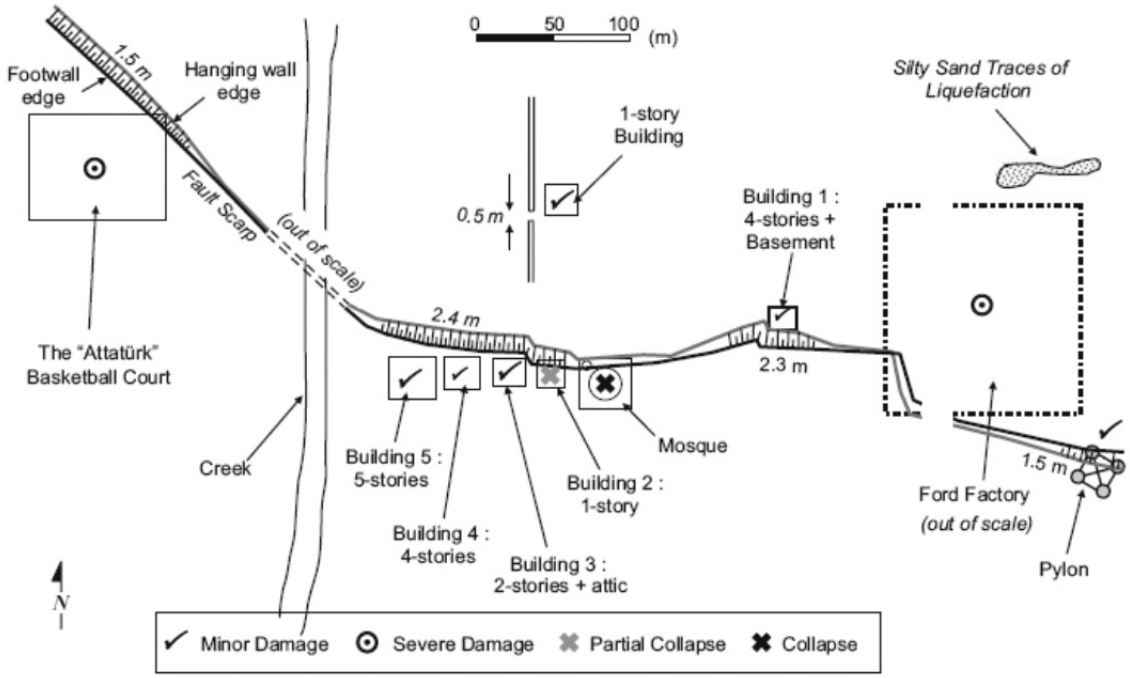

Figure 2-7. Observations of soil–structure interaction in the 1999 Kocaeli Earthquake (Anastasopoulos and Gazetas 2007a).

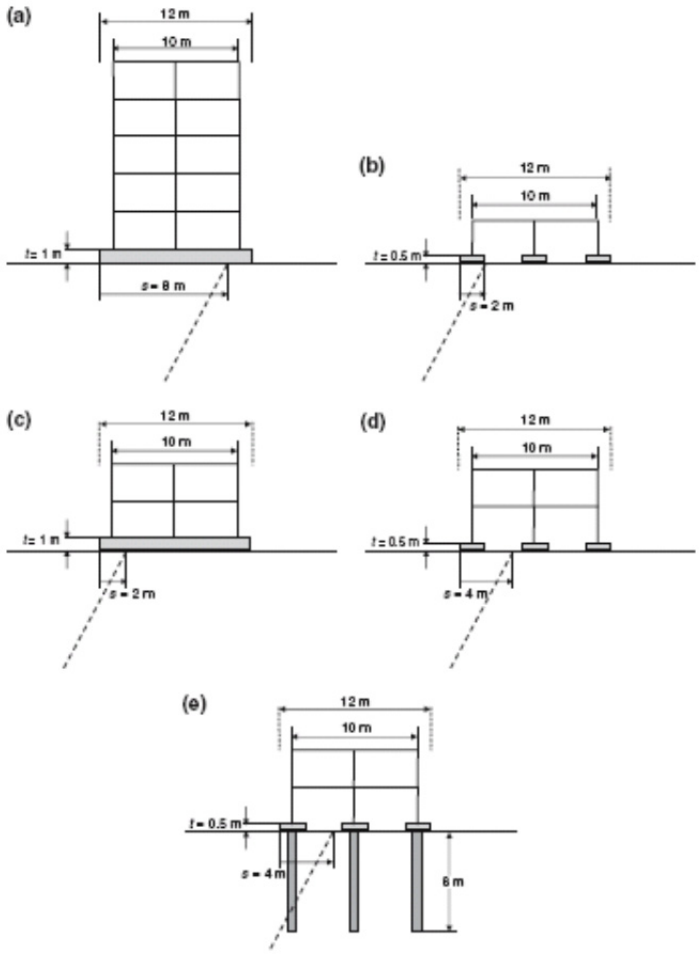

Figure 2-8. Numerical models used for five of the case histories from the 1999 Kocaeli Earthquake presented in Anastasopoulos and Gazetas (2007b); (a) four-story building with basement; (b) one-story building; (c) two-story building; (d) mosque equivalent to a two-story building; and (e) basketball court equivalent to a two-story building.

Figure 2-9. A building heavily damaged as a result of surface fault rupture during the 1999 Chi-Chi event (GEER 1999).

Figure 2-10. A building significantly rotated as a result of surface fault rupture during the 1999 Chi-Chi event (GEER 1999).

Figure 2-11. A building that partially collapsed likely as a result of surface fault rupture during the 1999 Chi-Chi event (GEER 1999).

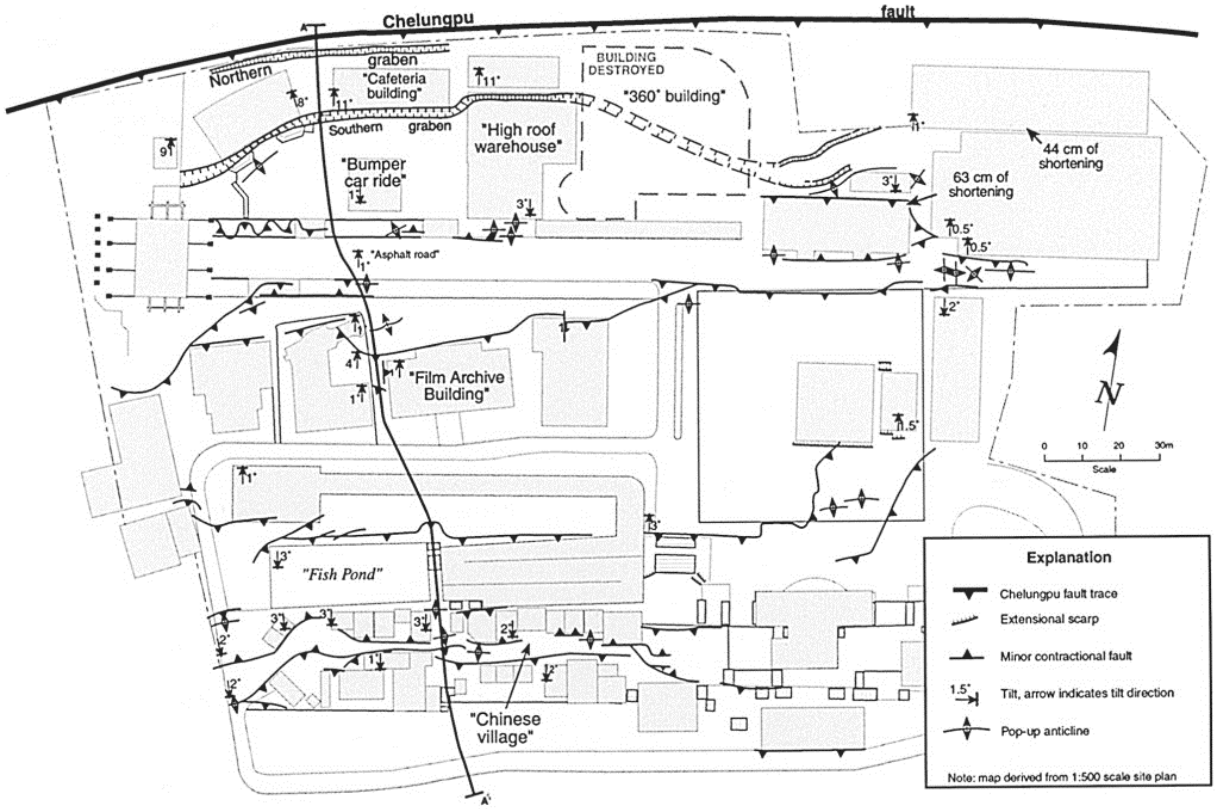

(a)

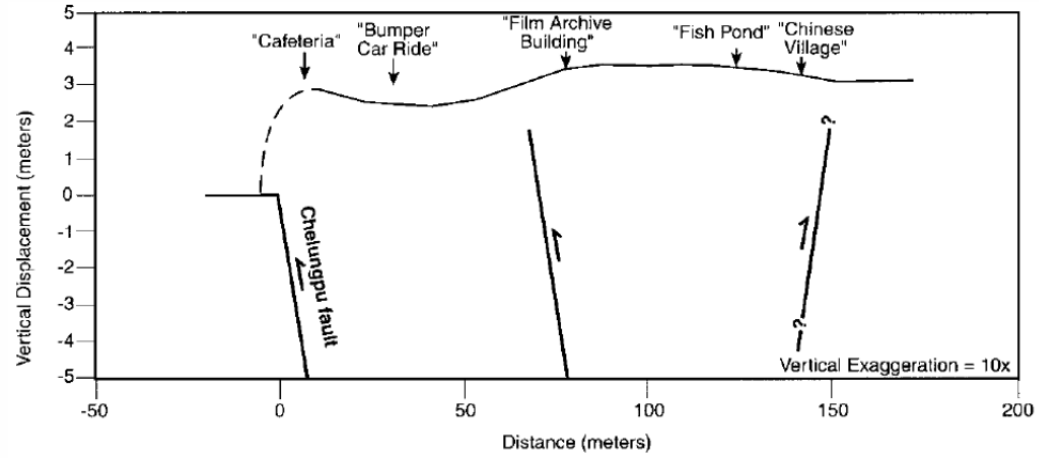

(b)

Figure 2-12. Broad distributed secondary hanging-wall deformation from surface fault rupture at Taiwan Studio City during the 1999 Chi-Chi event (Kelson et al., 2001b). (a) Plan view map of the area with the Chelungpu Fault and Studio City buildings shown, note that faulting was observed to be localized around the front and back of structures; (b) cross section A-A' showing the broad deformation through Studio City.

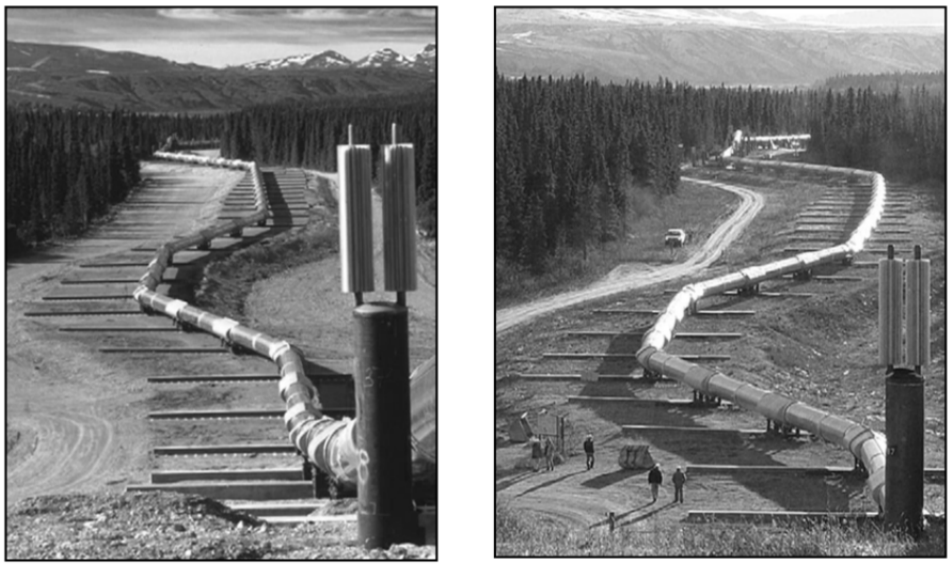

(a) before (b) after

Figure 2-13. The Trans-Alaska Pipeline crossing of the Denali Fault Zone: (a) before earthquake; (b) after earthquake (Sorensen and Meyer 2003).

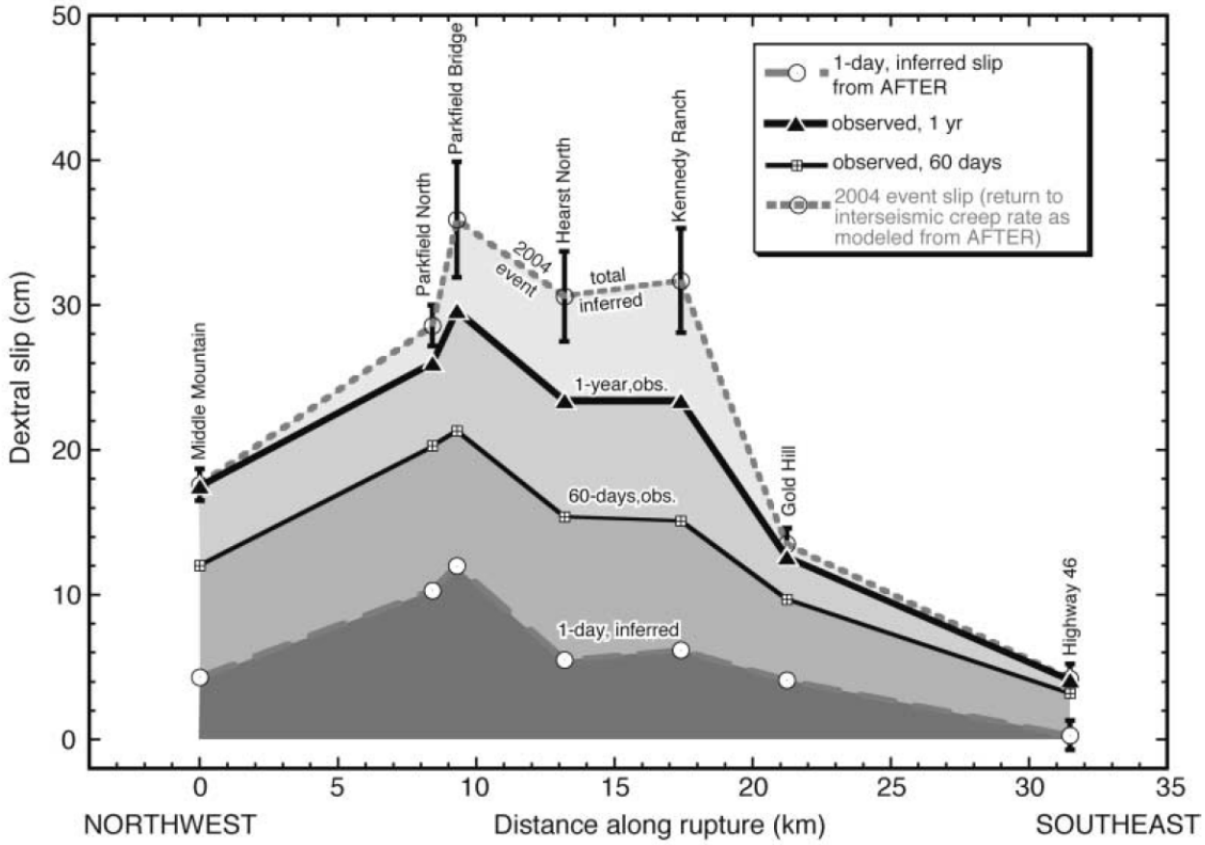

Figure 2-14. Surface rupture primarily as a result of increased creep following the 2004 Parkfield Earthquake (Lienkaemper et al. 2006).

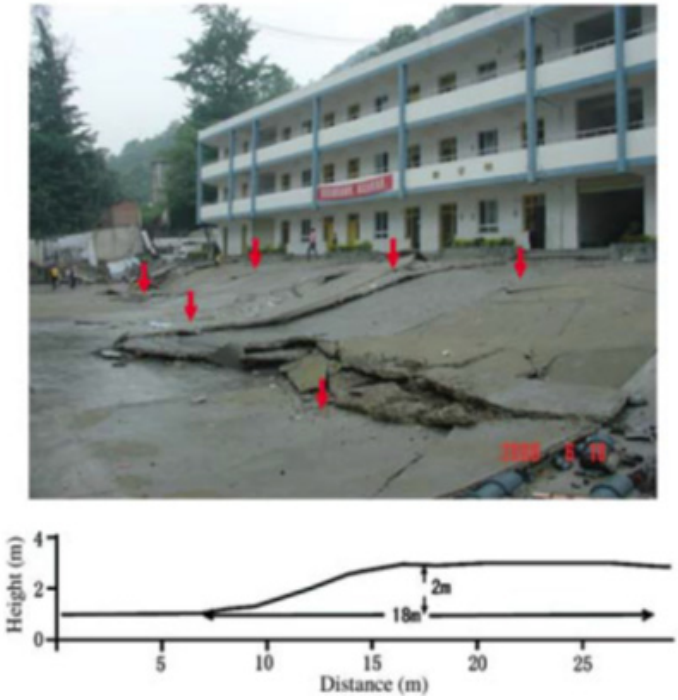

Figure 2-15. Surface rupture near a three-story building after the 2008 Wenchuan Earthquake (Zhou et al. 2010).

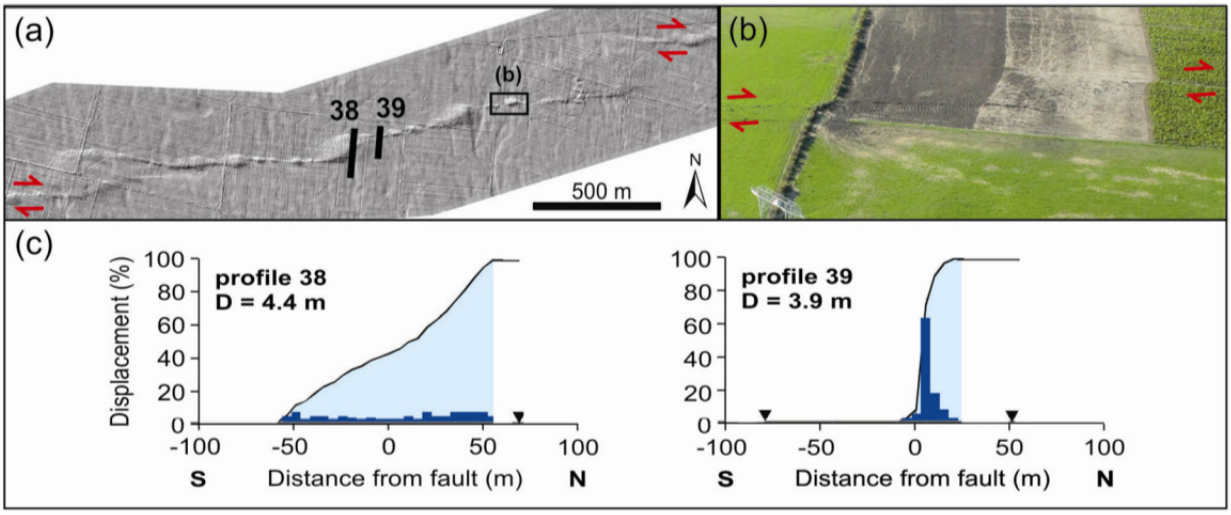

Figure 2-16. Distributed deformation during the Darfield, New Zealand Earthquake. (a) LiDAR data at a step-over in the fault; (b) LiDAR data away from the step-over; (c) change in ground displacement perpendicular to the fault at the step-over; and (d) change in ground displacement perpendicular to the fault away from the step over (Van Dissen et al. 2013).

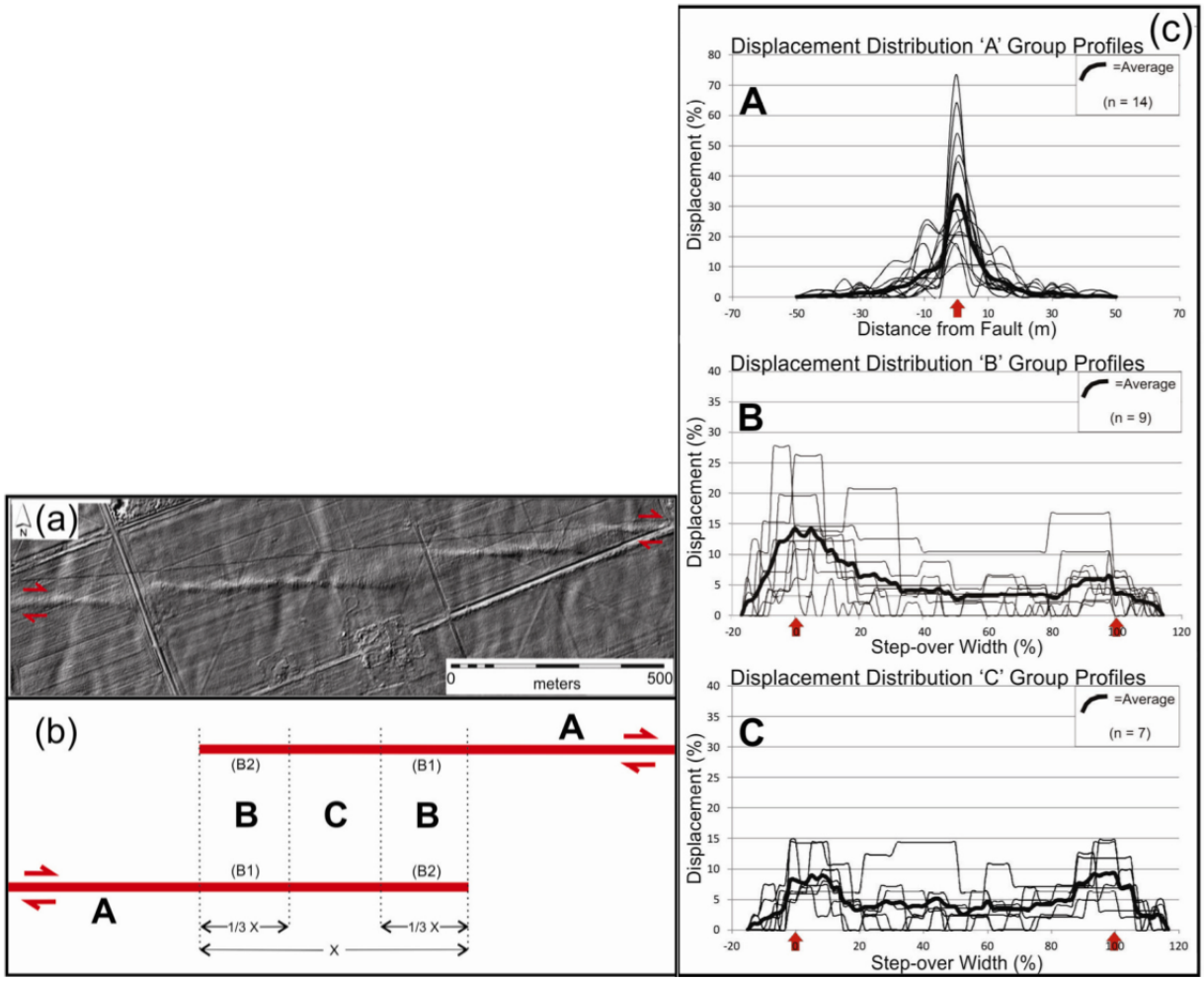

Figure 2-17. Distributed deformation during the Darfield, New Zealand Earthquake. (a) LiDAR data; (b) definition of A profile, B profile, and C profile types; (c) typical distribution of surface deformation away from the a step-over, at the edge of a step-over, and in the middle of a step-over. (Van Dissen et al. 2013).

Figure 2-18. Building damage as a result of surface fault rupture from the 2010 Darfield, New Zealand Earthquake (Van Dissen et al. 2011).

Figure 2-19. Free-field rupture from the 11 April 2011 Aftershock of the Great Tohoku Earthquake (GEER 2011).

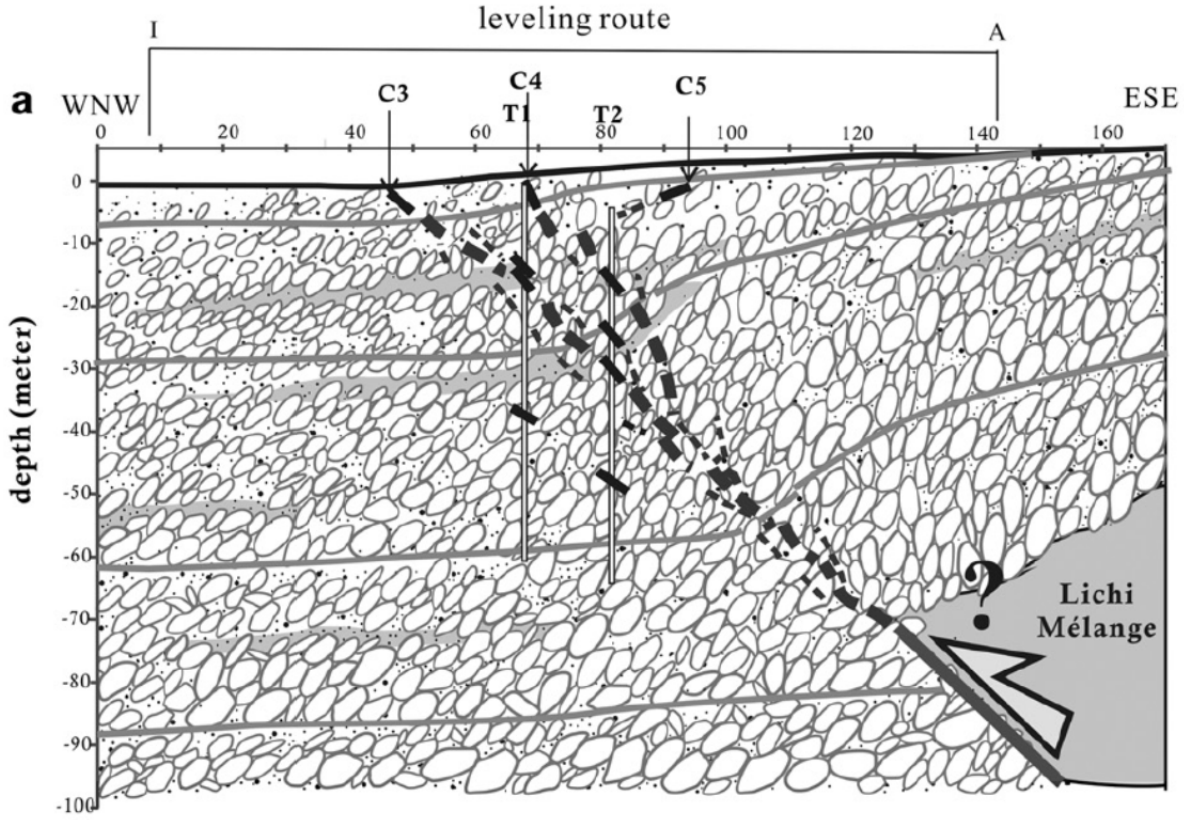

Figure 2-20. Interpreted cross section of a fault cutting through alluvium in Taiwan (Mu et al. 2011).

CHAPTER 3: NUMERICAL PROCEDURES AND VALIDATION

3.1 Numerical Procedures

Numerical Simulation Software

The two-dimensional (2D), plane strain, explicit finite-difference program FLAC (Itasca 2008) is employed to assess soil–structure interaction phenomena in fault zones for the case of dip-slip faulting. FLAC allows for incorporation of a nonlinear soil model with post-peak strain softening, large-strain calculations, and remeshing, among other features useful for analyzing the fault rupture process.

UBCSAND Soil Constitutive Model and Modifications

The UBCSAND model (Byrne et al. 2004) was selected as the soil constitutive model for capturing the nonlinear response of dry, uncemented sand. This is an elasto-plastic constitutive model with non-linear stress–strain response, contractive and dilative volumetric response, non-associated flow rule, and parameter dependence on effective confining pressure. The version of UBCSAND used herein was based on code dated 26 July 2009 provided by Prof. Peter Byrne (personal communication). The elastic response of this model is given by Equations 3.1 and 3.2:

$$B^e = K_B P_A \left(\frac{p\prime}{P_A}\right)^{n_e} \tag{3.1}$$

$$\mathrm{G^e = K_G^E P_A \left(\frac{p\prime}{P_A}\right)^{m_e}} \tag{3.2}$$

where B^e is the elastic bulk modulus, K_B is the elastic bulk modulus multiplier, P_A is the atmospheric pressure, p' is the mean effective stress in the plane of loading, n_e is the elastic bulk exponent, G^e is the elastic shear modulus, $K_G{}^E$ is the elastic shear modulus multiplier, and m_e is the elastic shear exponent.

Plastic response is predicted to be initially stiff and decrease in stiffness as the stress ratio is increased. This hardening behavior is modeled with a hyperbolic law. The plastic behavior is based on the elastic shear modulus, is stress dependent, and has variable nonlinearity. The plastic response is described in Equations 3.3 through 3.7:

$$\Delta\gamma^p = \left(\frac{1}{G^*}\right)\Delta\eta_d \tag{3.3}$$

$$\eta_d = \frac{q}{p\prime} = \sin\phi_d \tag{3.4}$$

$$\Delta\eta_d = \left[\frac{\Delta q}{p\prime} - \left(\frac{q}{(p\prime)^2}\right)\Delta p'\right] \tag{3.5}$$

$$\Delta\gamma^p = \frac{1}{G^*}\left[\frac{\Delta q}{p\prime} - \left(\frac{\eta_d}{p\prime}\right)\Delta p'\right] \tag{3.6}$$

$$G^* = K_G^P(\text{hfac1})\left(\frac{p\prime}{P_A}\right)^{n_p-1}\left[1-\left(\frac{\eta_d}{\eta_f}\right)R_f\right]^2 \quad (3.7)$$

where $\Delta\gamma_p$ is the plastic shear strain increment, G^* is the plastic shear modulus, $\Delta\eta_d$ is the stress ratio increment, η_d is the developed stress ratio, q is the shear stress on the plane of maximum shear stress, ϕ_d is the developed friction angle, $K_G{}^P$ is the plastic shear modulus, *hfac1* is the plastic modulus multiplier, n_p is the plastic modulus exponent, η_f is the stress ratio at failure, and R_f is the failure ratio.

The UBCSAND model was modified to enhance its capabilities for simulating the surface fault rupture process. Importantly, post-peak strain softening, which was identified previously by several researchers as being essential (e.g., Anastasopoulos et al. 2007), was added. This modification decreased the soil yield surface after a peak stress condition was reached over a given strain interval to the critical-state stress ratio. Additionally, the UBCSAND model was modified to have a stress-dependent peak friction angle using a $\Delta\phi$ Duncan et al. (1980)-type approach and simplified by disabling parameters only required for capturing cyclic loading. The equations adopted for strain softening are provided in Equations 3.8 and 3.9. The stress dependent friction angle equation adopted herein is presented in Equation 3.10:

$$\eta_f = \sin\left[\phi_f - \frac{\gamma_{soften}}{\gamma_{pp}}(\phi_f - \phi_{cs})\right] \quad (3.8)$$

$$\gamma_{soften} = \min\left[\gamma_{pp},\ \sum^{post-peak}\Delta\gamma^p\right] \quad (3.9)$$

$$\phi_f = \max\left[\phi_{cs}, \left(\phi_{peak} - \Delta\phi\log\frac{\sigma_3'}{P_A}\right)\right] \quad (3.10)$$

where ϕ_f is the failure friction angle, γ_{soften} is the developed post-peak shear strain, γ_{pp} is the shear strain from peak stress to critical state, ϕ_{cs} is the critical state friction angle, ϕ_{peak} is the failure friction angle at atmospheric pressure, $\Delta\phi$ is the confining pressure dependence of the friction angle, and σ_3' is the minor principal stress.

A non-associated flow rule is used within UBCSAND. Contractive behavior is modeled at stress ratios below the critical state stress ratio. Dilative behavior is modeled above the critical state stress ratio. A smooth transition between the two regimes is used. As a result of the modifications to UBCSAND described above, where strain-softening was added to the constitutive model, the modified UBCSAND model predicts constant volume behavior when the soil is fully softened (i.e., dilation cutoff). The original UBCSAND model predicted continuous dilation under shear (i.e., no dilation cutoff). The UBCSAND flow rule is defined by Equations 3.11 through 3.15, given below.

$$\Delta\varepsilon_V^p = (\sin\psi)\Delta\gamma^p \quad (3.11)$$

$$\sin\psi = (\sin\phi_{cs} - \sin\phi_d) \quad (3.12)$$

$$f = \sigma_1' - \sigma_3'(1+\eta_d)/(1-\eta_d) \quad (3.13)$$

$$g = \sigma_1' - \sigma_3'(1 + \sin\psi)/(1 - \sin\psi) \quad (3.14)$$

$$\Delta\varepsilon_{ij}^{p} = \lambda\left(\frac{\partial g}{\partial \sigma_{ij}'}\right) \quad (3.15)$$

where $\Delta\varepsilon_V^p$ is the increment of plastic volumetric strain, ψ is the dilation angle, f is the yield function, σ_1' is the major principal stress, g is the plastic potential function, $\Delta\varepsilon_{ij}^p$ are the plastic strain increments, and λ is a constant proportionality between plastic strain increments and the partial derivative of *g* with respect to the effective stress.

As a result of including strain softening in the soil constitutive model, the numerical simulations became mesh dependent (Simo et al. 1993). There are methods that can model strain-softening shear bands without mesh dependence (e.g., Simo et al. 1993); however, specialized methods like these are not available in FLAC. Anastasopoulos et al. (2007) used a regularization method to account approximately for mesh dependency effects, which was adopted herein. This regularization method allows the strain required to soften fully the shear band to be scaled approximately to the mesh size. Based on work reported in Bransby et al. (2008a), the shear band in sand was assumed to be approximately 16 d_{50} wide with a displacement of approximately 100 d_{50} is required to soften fully the shear band (where d_{50} is the median grain size of the sand). When modeling sand deposits at prototype scale, a post-peak shear strain of 6% was required to reach critical state, which is appropriate for a fine sand with a mesh size of 0.2 m. The anticipated width of the shear band was smaller than the typical mesh width, as it was unreasonable to employ a mesh size of only 0.002 m (i.e., 16 d_{50}). When modeling centrifuge tests performed at 115 g, the particle grain size increases by a factor of 115 at prototype scale, so the shear strain required to soften fully the shear band was increased by a factor of 115 after adjusting for a mesh size that equaled the width of the shear band (0.4 m at prototype scale; Bransby et al. 2008a). In this way, the width of the shear band and the displacement required to soften fully the shear band were captured well in the back-analyses of the centrifuge tests. The regularization equations used herein are provided in Equations 3.16 and 3.17.

$$\gamma_{pp} = \frac{100(d_{50})}{d_{fe}} \quad (3.16)$$

$$\gamma_{pp-cent.} = \gamma_{pp}(N) \quad (3.17)$$

where d_{50} is the median sand grain size, d_{fe} is the width of a mesh element, $\gamma_{pp\text{-}cent.}$ is γ_{pp} for a centrifuge test, and N is the scale multiplier in the centrifuge test.

Model Parameters

All UBCSAND model parameters were assigned conventional values (Dr. Michael Beaty, unpublished presentation, October 2007), except instead of varying the parameter Rf slightly, it was set to 0.95 to obtain a relatively high level of nonlinearity in the soil's stress–strain response. Recommended parameter values for the UBCSAND model are based on the relative density of the soil being modeled. Baseline model parameter selection is based on critical state concepts and typically observed behavior for quartz sands. The plastic shear modulus was calibrated to match the apparent failure strain of the soil in the centrifuge tests.

This was done by adjusting the UBCSAND parameter *hfac1* to capture realistic failure strain values for soil, as discussed in detail later. A complete list of the baseline modified UBCSAND parameters used in this study is provided in Table 3-1. The resulting plane-strain compression response for the modified UBCSAND model with these baseline parameters is presented in Figure 3-1.

Modeling Methods

The underlying fault movement was modeled as a single, distinct offset of rigid bedrock. The FLAC model's boundary conditions were implemented similar to other researchers (e.g., Bray et al. 1994b; Anastasopoulos et al. 2007). The footwall lateral boundary was fixed in the horizontal direction; the footwall base boundary was fixed in both the horizontal and vertical directions. On the hanging wall, at both the base and lateral boundary, velocity was applied in the direction of fault movement. A representative progression of shear strain contours with displacement was applied pseudostatically (i.e., transient ground motions were ignored) using the increasing fault movement is shown in Figure 3-2. As conventionally done, the bedrock fault displacement was applied pseudostatically (i.e., transient ground motions were ignored) in most cases using the combined-damping formulation in FLAC (Itasca 2008). Convergence of the model element size and time increment were checked to ensure accurate numerical results. FLAC indicators of convergence were also tracked (Itasca 2008).

Foundations, when employed in the centrifuge tests, were modeled as beam elements with appropriate structural properties. Foundation elements were surrounded by interface elements with frictional properties similar to that of the underlying soil. The simulations with structural beam elements were analyzed in large-strain mode until just before the mesh was distorted beyond its ability to continue with large strain calculations; fault movement was then continued with small-strain calculations, because FLAC does not currently support remeshing when models contain structural elements.

Two steel moment-frame structures were analyzed to evaluate soil–foundation–structure interaction aspects further. A three-story structure (Lee et al. 2004) and a six-story structure (Kalkan and Kunnath 2006) were modeled with beam elements in FLAC. The three- and six-story structures are shown in Figure 3-3 and Figure 3-4, respectively. Building loads were assumed to be 10 kPa per floor, including the roof, for the three-story structure and 7 kPa for six-story structure. This mass was included in the beams. Full moment capacity was assumed for both the beam and columns, and strength-limited compression and tension capacities were used. Properties for the structural elements were taken from American Institute of Steel Construction (2005) and are presented in Table 3-2. Shear failure cannot be modeled directly in FLAC, so shear failure in the structural elements was checked manually. Analysis of these structures was limited to the elastic range with perfectly plastic response thereafter.

The steel frames of these two structural models were attached to reinforced-concrete (RC) mat foundations with full moment connections. Properties of the mat were based on its thickness with typical detailing. The second moment of area was taken as half of that calculated for a rectangular cross section to approximate the cracked second moment. Other properties of the mat foundations are provided in Table 3-2.

Incremental Calibration

The constitutive model parameters were calibrated to centrifuge tests conducted by Bransby et al. (2008a,b). A new method of interpreting the surface response of the centrifuge tests was developed to more accurately calibrate the numerical model. This process involves examining the incremental response of the surface for consecutive displacement intervals, e.g., comparing the surface response for displacements between 0 and 0.3 m, 0.3 and 0.6 m, and 0.6 and 0.9 m. This procedure assists in identifying the transition between the pre-failure and post-failure regimes of the centrifuge tests, and therefore, helps to identify the effective failure strain of the soil, which has been previously identified (Bray et al. 1994a,b) as a key parameter for soil response to underlying fault rupture.

To calibrate the constitutive model using the incremental method, free-field test results from Bransby et al. (2008a,b) were used to eliminate complexities associated with soil–structure interaction which are not necessary to evaluate when calibrating for the soil failure strain. Calibration was separated for normal and reverse faults to identify potential differences between these two modes of shear. Results for centrifuge test 28 (reverse fault) and centrifuge test 12 (normal fault) are presented in Figure 3-5 and Figure 3-6, respectively.

The results for test 28 indicate that an *hfac1* value (a parameter that multiplies with the soil stiffness, and therefore linearly adjusts the soil failure strain) of approximately 0.025 best captures the transition between the pre-failure and post-failure regimes of the reverse fault centrifuge test results. Higher failure strains (softer response) inhibit the transition between a wide (pre-failure) surface deformation response and a narrower (post-failure) surface response at the correct level of fault displacement, as shown in Figure 3-5. Lower failure strains (stiffer response) cause a pre-mature transition to a highly localized surface expression of fault deformation. The calibrated soil stiffness corresponds to failure strains for various stress paths shown in Table 3-3.

For centrifuge test 12 (normal fault), the transition between pre-failure and post-failure response was difficult to detect in the numerical model, as shown in Figure 3-6a. To better contrast these regimes, a more abrupt transition between peak strength and critical state strength was implemented to better calibrate the appropriate failure strain for the numerical model. This response is shown in Figure 3-6b. With this change to the shear banding behavior implemented, a calibrated value for *hfac1* was determined. The appropriate soil stiffness to match the centrifuge test results transition between pre- and post-failure regimes was best matched with an *hfac1* of approximately 0.025 (the same value as for reverse faults).

The results of the incremental calibration procedure indicate that the selected constitutive model may appropriately model the transition between pre- and post-peak regimes for both normal and reverse faults with the same plastic stiffness model parameters.

3.2 Simulation Validation

Free-Field Tests

The capabilities of the numerical simulations were validated using the centrifuge tests presented in Bransby et al. (2008a,b). Figure 3-7 provides illustrative results of centrifuge test 28 (free-field, reverse fault) and our corresponding numerical simulation with the constitutive model

and parameters discussed above for comparison. The shear band developed during this test can be seen for both the centrifuge test and the numerical simulation. The general location, curvature, and outcropping location of the fault produced through the numerical simulations are consistent with those observed in the geotechnical centrifuge experiments. Figure 3-8 presents more detailed results of the same test in terms of ground deformation near the surface (note that ground surface is defined as within 1 m of the ground surface herein to match the position of the available centrifuge data) and angular displacement near the surface.

Results of ground deformation near the surface are shown for three levels of base displacement. The results show that the horizontal location of the point halfway between the footwall and hanging wall shifts to the left as the base displacement increases for both the numerical and centrifuge results. The increasing slope of the ground surface as the base displacement is increased in the numerical simulation is consistent with that of the geotechnical centrifuge results. The angular distortion away from the fault on the footwall is approximately matched, but the distortion away from the fault on the hanging wall side is somewhat under estimated. While the general location of the fault outcrop was well estimated, the exact location was shifted by approximately 2 m to the footwall side of the fault in the numerical simulation relative to the centrifuge test results. This observation is further reinforced by the angular distortion compared in Figure 3-8.

Results are presented in Figure 3-9 and Figure 3-10 for centrifuge test 12 (free-field, normal fault). Many general characteristics of the surface response were well estimated by the numerical model. Results at lower base offsets were typically better matched between the geotechnical centrifuge and numerical simulations, especially with regard to the maximum slope of the deformed ground surface. However, the numerical model calculated the formation of a graben at low base offsets whereas the centrifuge only developed a graben at larger deformations. In addition to the mismatch of graben formation, the numerical model calculated the location of the outcrop (or peak angular distortion) would be slightly more to the footwall side of the fault than the centrifuge tests indicated. This shift in the numerical results relative to the centrifuge test results for the normal fault is consistent with the shift observed for the reverse fault simulations.

Modification of the Flow Rule and Localization Behavior

To address the small, but consistent, shift between numerical results and centrifuge test data observed in both normal and reverse fault analyses, the flow rule was modified from the original UBCSAND implementation to allow for an adjustment of the stress ratio at which contractive volumetric behavior transitions to dilative behavior (i.e., the characteristic line). This was implemented because soil dilatancy has previously been identified as an important parameter for analyzing surface fault rupture propagation through soil (Lade and Cole 1984). A new parameter, *hfac5*, was introduced to the modified version of UBCSAND to implement this shift in the characteristic line. These modifications are described in Equations 3.18 and 3.19.

$$\sin\psi = (\sin\phi_a - \sin\phi_d) \tag{3.1}$$

$$\sin\psi = (\sin\phi_{cs} - hfac5 - \sin\phi_d) \tag{3.2}$$

where ϕ_a is the angle of the characteristic line and *hfac5* is the difference between the characteristic line and the critical state line.

In the standard UBCSAND model, contractive behavior occurs during plastic shearing for stress ratios below the critical state stress ratio while dilation behavior occurs beyond it. In this modified model, if *hfac5* is a small, positive number, dilation will occur at a slightly lower stress ratio than critical state. If *hfac5* is a small, negative number, dilation will occur at a slightly higher stress ratio than critical state.

This change in the flow rule is consistent with the response of sand observed in other tests and used in other constitutive models where a separate characteristic line is established near the critical state stress ratio (e.g., Boulanger 2010). Lade and Ibsen (1997) and Lade and Abelev (2003) noted that the characteristic line is significantly dependent on the confining stress, lode angle, and b-value, indicating that the appropriate characteristic line may be different for reverse and normal faults since each of these fault types is associated with a unique stress path response in the soil overlying the fault (Oettle and Bray 2013a).

When the flow rule is modified by adding the parameter *hfac5*, the comparisons between the results of the numerical simulations and the results of the geotechnical centrifuge experiments are improved. An *hfac5* value of 0.07 was found to fit best for normal faults, and an *hfac5* value of -0.1 was found to fit best for reverse faults. The different best-fit parameterization between normal and reverse fault types is likely attributable to the compression unloading stress path in normal faults and the extension loading stress path in reverse faults. This modification to the dilatancy of the soil also improved the fit between the numerical and experimental results for the normal fault case vis-a-vis the graben formation which was calculated to be more significant in the numerical model than was observed in the experimental results.

Another discrepancy between the experimental data and numerical simulations was the highly localized incremental response observed for normal faults (but not reverse faults) as noted earlier and shown in Figure 3-6a. These results show that the numerical model does not capture accurately the highly localized incremental response observed in normal fault centrifuge tests but rather calculated a broader surface response, as visible in Figure 3-9. This broad response of the numerical model caused the angular distortion on the footwall side of the fault to be over-estimated and produced a large mismatch in the calculated and observed ground surface slope at the fault outcrop location for high base dislocations, as shown in Figure 3-10.

To produce a more localized surface deformation response, as observed in the centrifuge model results, the displacement required to fully soften the shear band was significantly reduced from $100d_{50}$ to an almost immediate transition from peak shear strength to critical state shear strength. This adjustment to the constitutive model produced a more localized surface deformation response in the post-failure regime. These results matched more closely with the centrifuge experimental results in terms of the degree of post-failure localization and the location of that localization. Element shear test results presented in Abelev and Lade (2003), which found very abrupt transitions between peak strength and critical state strength for certain lode angles, may point to a potential cause. The compression unloading stress path calculated to occur in soil above a normal fault (Oettle and Bray 2013a) may also cause such a localized response. Reverse faults were not found to require this change to the model parameters; this is likely a result of the extension loading stress path expected for reverse faults. Alternatively, the origin of this mismatch between experimental and numerical results for normal faults could arise from the

numerical techniques used to model strain softening and shear banding (i.e., mesh dependency and related issues with modeling strong discontinuities in a continuum). It may be appropriate to investigate whether these conclusions are affected by the regularization techniques used to model strain softening. Performance of element tests for normal fault stress paths and analysis of their fundamental shear banding behavior would also be valuable.

The adjusted and improved numerical model results, with the added *hfac5* parameterization and increased post-peak localization for normal faults, are presented in Figure 3-11 for the reverse fault and Figure 3-12 for the normal fault.

Soil–Structure Interaction Tests

The centrifuge tests conducted by Bransby et al. (2008a,b) were replicated using the developed numerical model to analyze the capability of the model to capture the soil–structure–fault interaction observed in centrifuge testing. A representative illustration of the general capability of the numerical model to account for soil–structure interaction effects is presented in Figure 3-13. In this figure, several shear bands are visible in the centrifuge test, showing complex interaction between the soil, fault, and structure which were not observed for free-field centrifuge tests. The corresponding numerical model was able to generally capture the observed complex system behavior.

To analyze in detail the capability of the numerical model to replicate observed trends in the soil–structure interaction behavior for changes to the test configurations, a series of detailed comparisons of the surface deformation for a number of centrifuge tests is presented. In each centrifuge test, one aspect of the test configuration was changed, as documented in Bransby et al. (2008a,b). Each centrifuge test is compared to the reference case and plotted against the numerical model results. In each case, the change in ground surface deformation from the reference case to the test case is mirrored by the numerical model.

In Figure 3-14, the free-field results for a reverse fault are compared to the same test configuration with the addition of a relatively rigid, 10 m wide foundation applying a 91 kPa load. In both the numerical simulations and geotechnical centrifuge results, the foundation suppressed the ground deformation underneath the foundation, i.e., the fault was partially diverted. The same comparison is made for the case of a normal fault in Figure 3-15. In this case, the foundation also suppresses movement beneath the foundation, partially diverting the fault, for both the numerical model and centrifuge test. In both the reverse and normal fault tests, the numerical model roughly matches the slope of the ground and tilt of the foundation.

In Figure 3-16 to Figure 3-20, the mechanical properties of the foundation element are adjusted to reflect each centrifuge test. The results of each test case are compared to the centrifuge test of the baseline structural condition presented in Figure 3-14 and Figure 3-15 for reverse and normal faults, respectively. In the comparison shown in Figure 3-16, the foundation weight is reduced to 37 kPa, from 91 kPa, for the reverse fault case. This change decreases the soil–structure–fault interaction and the surface deformation becomes more similar to that of the free-field condition. This causes the foundation tilt to increase and the fault diversion to be minimized. The same comparison is made for a normal fault in Figure 3-17 and similar results are obtained which show a decrease in fault diversion and an increase in building tilt. For both the normal and reverse faults, the numerical model roughly matches the estimated slope of the ground deformation and the corresponding building tilt.

In Figure 3-18, results are presented for centrifuge test 18 (a normal fault) where the foundation was moved 5 m to the left of the baseline location. The change in fault–structure geometry resulted in (a) the building remaining more on the footwall side of the fault than the hanging wall side; and (b) the ground response underneath the structure to be more curved compared to the reference structural case. The numerical model captured both of these trends. In Figure 3-19, results are shown for a larger 25 m-wide foundation, also for a normal fault, compared to the 10 m-wide foundation of the reference case. The wider foundation caused, in both the numerical simulation and the centrifuge test, the foundation to span the entire length between the footwall side and hanging wall side of the fault, essentially eliminating diversion of the fault away from the building but spreading the fault deformation evenly underneath the foundation. The final comparison, presented in Figure 3-20, compares the relatively rigid foundation of the reference case with a flexible foundation of the same geometry and weight. The flexible foundation caused the ground surface deformation to be curved markedly underneath the foundation compared to the relatively constant slope beneath the rigid foundation. This trend was matched in the numerical simulation with the foundation tilting at a higher angle on the footwall side of the foundation than on the hanging wall side.

The numerical model results of the above comparative analysis for the same numerical model but without the modifications to the flow rule through the *hfac5* parameter or the abrupt localization specific to normal faults is presented in Appendix A, Figure A-1 through Figure A-7. This comparison is made because the numerical model used in Chapters 4 through 6 does not implement the aforementioned changes. The results presented in Appendix A, however, still match the general trends observed in the centrifuge data despite not capturing some of the minor details which prompted the above modifications. The parameter *hfac5* was developed later in this program of research to investigate what might be required to better capture some details of the earthquake fault rupture phenomenon. Its use is not required to capture the key aspects of the problem, and the value of the *hfac5* parameter requires calibration. However, in those cases where sufficient data are available to calibrate this extra parameter, improved modeling of some of the details of the surface fault rupture hazard can be achieved.

3.3 Conclusions

An improved numerical model based on the UBCSAND soil constitutive model was developed to analyze soil–structure–fault interaction problems. Th results of these numerical simulations were compared against the observations from an extensive set of geotechnical centrifuge experiments that included the effects of structures. Both the numerical model results and centrifuge test results show that structures can have a significant effect on the propagation of dip-slip fault rupture through engineered fill.

The UBCSAND constitutive model was modified to add strain softening, a non-linear failure envelope, and a variable volumetric response rule. Constitutive model parameters were calibrated primarily by adjusting for the known relative density of the centrifuge test soil. In addition, incremental plots of the surface response in the centrifuge tests were used to estimate the failure strain of the soil. The UBCSAND parameter *hfac1* was used to calibrate the numerical model to the apparent soil failure strain observed in the centrifuge tests.

The proposed numerical model was able to capture well key trends in the experimental data. These key trends include increasing fault diversion with increasing structural weight,

increased fault diversion for stiff structures, fault propagation dependence on the location of the structure, and significant dependence on the width of the building. In general, free-field test results were also matched well with experimental data in terms of the calculated ground deformation. However, two minor adjustments to the originally proposed model and model parameters were found to be necessary to match differences in response between normal and reverse fault tests. These minor differences were attributed to two factors in the employed constitutive model, which are explained subsequently.

First, highly localized post-peak behavior was observed in normal faults and not in reverse faults. This localization was incorporated into the numerical model by modifying the post-peak strength response of the soil to transition abruptly from the peak strength to the critical state shear strength. This response is likely attributable to the differences in loading and stress path that a normal fault undergoes relative to a reverse fault (i.e., extension loading for reverse faults and compression unloading for normal faults).

Second, a small but consistent horizontal offset between the numerical results and centrifuge data was observed. The location of the fault outcrop at the ground surface calculated through the numerical simulation was approximately 2 m further to the footwall side of the fault relative to that observed in the centrifuge test results. This systematic mismatch was controlled by the selected flow rule. Consequently, the stress ratio at which contractive response transitions to dilative behavior (the characteristic line) was adjusted to modify the flow rule. It was found that shifting the characteristic line to just above the critical state stress ratio eliminated the horizontal offset in the numerical simulations for the reverse fault cases. For normal faults, a characteristic line just below the critical state stress ratio was found to best match experimental data. The need for different characteristic lines for normal and reverse faults may be attributable to the stress paths of soil overlying normal and reverse faults because the location of the characteristic line can vary with confining stress and b-value. Modifications to the flow rule also helped minimize differences in graben formation between numerical and experimental results during normal fault rupture scenarios.

These numerical simulations were able to capture the observed trends in the experimental data well. Therefore, the FLAC finite difference analyses using the modified UBCSAND constitutive model were judged provide reasonable insights. These findings are similar to those of previous researchers (e.g., Bray et al. 1994b, and Anastasopoulos et al. 2007), who demonstrated that nonlinear soil models with a well-defined failure strain and post-peak drop in shear strength can capture the key features of fault rupture propagation through previously unruptured soil. However, the enhancements to the UBCSAND model discussed in this chapter offer an improved modeling capability of the earthquake surface fault rupture phenomenon. The numerical model developed herein can be applied to analyze dip-slip fault propagation through engineered fill and account for the effects of soil–structure–fault interaction to estimate permanent ground deformation resulting from underlying fault movement.

Table 3-1. Representative UBCSAND model parameters used in study.

Parameter	Function	Value
D_r	Relative density	Varies
ρ	Dry mass density	1.6 Mg/m^3
$N_{1,60}$	Normalized, corrected SPT blow count	D_r^2 x 60
K_G^E	Elastic shear modulus multiplier	21.7 x 20 x $(N_{1,60})^{0.333}$
m_e	Elastic shear exponent	0.5
K_B	Elastic bulk modulus multiplier	0.7 x K_G^E
n_e	Elastic bulk exponent	0.5
K_G^P	Plastic bulk modulus multiplier	K_G^E x $(N_{1,60})^2$ x 0.003 +100
n_p	Plastic bulk exponent	0.4
ϕ_{cs}	Critical state friction angle	33^o
ϕ_{peak}	Peak friction angle	ϕ_{cs} + $N_{1,60}$ / 10 + max[0,($N_{1,60}$-15)/5]
R_f	Failure ratio	0.95
hfac1	Model parameter	0.025
hfac2	Model parameter	1.0
hfac3	Model parameter	n/a
hfac4	Model parameter	n/a
anisofac	Model parameter	1.0
γ_{pp}	Shear strain from peak stress to critical state	0.06
$\Delta\phi$	Stress-dependent friction angle	4^o

Table 3-2. Properties of the three-story and six-story structural models (from American Institute of Steel Construction 2005).

Specification	Type	I (m^4)	A (m^2)	M_n (kN*m)	V_n (kN)	Axial (kN)
Three-story structure						
W14x211	Column	0.001108	0.0400	2205	2060	13807
W14x370	Column	0.002267	0.0704	4169	3969	24274
W30x90	Beam	0.001504	0.0170	1601	1672	5879
W30x108	Beam	0.001862	0.0205	1964	2176	7059
W30x116	Beam	0.002054	0.0221	2145	2270	7616
Six-story structure						
W14x90	Column	0.000416	0.0171	866	825	5901
W14x132	Column	0.000637	0.0250	1326	1266	8641
W14x176	Column	0.000892	0.0334	1775	1690	11536
W24x68	Beam	0.000762	0.0130	1003	1315	4476
W24x84	Beam	0.000987	0.0159	1269	1516	5501
W27x102	Beam	0.001508	0.0194	1722	1868	6681
W30x116	Beam	0.002054	0.0221	2145	2270	7616

Notes: I = second moment of area; A = cross-sectional area; M_n = nominal moment capacity; Vn = nominal shear capacity; Axial = axial capacity; the modulus of elasticity of steel structural members was assumed to be 200 GPa and for the reinforced concrete mat foundation 30 GPa; the nominal moment capacities of the mat foundations were assumed to be 120 kN*m, 760 kN*m, 1,000 kN*m, 3,600 kN*m, 8,900 kN*m, 20,000 kN*m, 57,000 kN*m, and 130,000 kN*m for mat thicknesses of 0.2 m, 0.4 m, 0.45 m, 0.8 m, 1.2 m, 1.8 m, 3.0 m, and 4.5 m, respectively.

Table 3-3. Soil failure strain in UBCSAND for various loading conditions and model parameters with baseline parameters defined as per Table 3-1.

	PSC (loading)		PSC (unloading)	PSE (loading)
Parameter	γ_{max}	ε_a	γ_{max}	γ_{max}
hfac1 = 0.01	24.7%	12.4%	31.1%	61.0%
hfac1 = 0.025	10.0%	5.0%	12.5%	24.5%
hfac1 = 0.05	5.0%	2.5%	6.2%	12.4%
hfac1 = 0.1	2.5%	1.3%	3.1%	6.3%
R_f = 0.98	25.7%	12.9%	31.6%	61.0%
R_f = 0.95	10.0%	5.0%	12.5%	24.5%
R_f = 0.90	4.6%	2.3%	5.9%	12.1%
R_f = 0.70	1.2%	0.6%	1.5%	3.9%
$N_{1,60}$ = 15	20.4%	10.2%	26.7%	51.4%
$N_{1,60}$ = 22	10.0%	5.0%	12.5%	24.5%
$N_{1,60}$ = 34	4.4%	2.2%	5.1%	10.7%

Notes: PSC = Plane Strain Compression; PSE = Plane Strain Extension

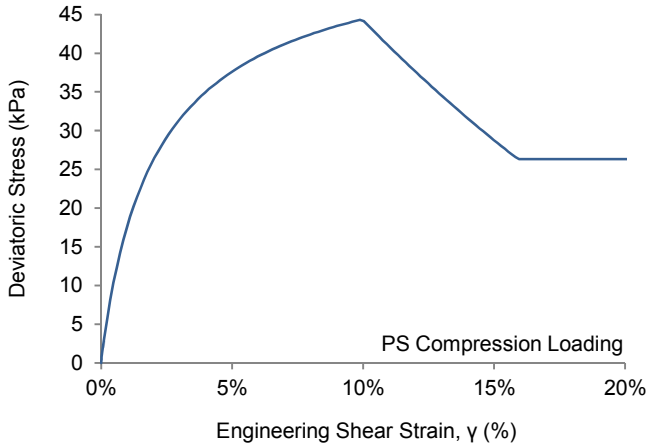

(a)

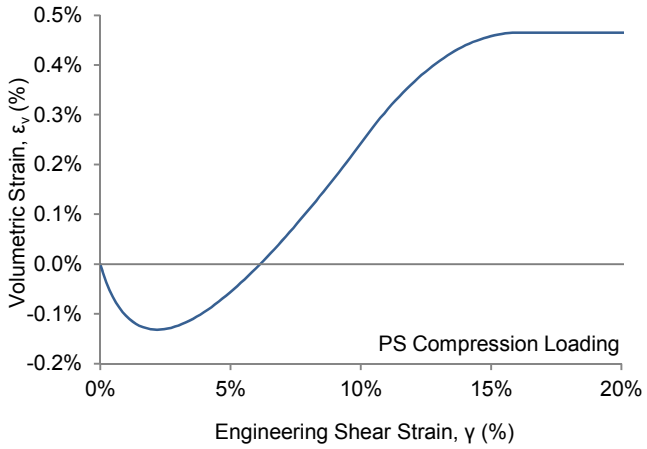

(b)

Figure 3-1. Element response of the modified version of UBCSAND used herein in plane-strain compression loading ($N_{1,60}$=22, K_0=0.45, σ'_3=45 kPa).

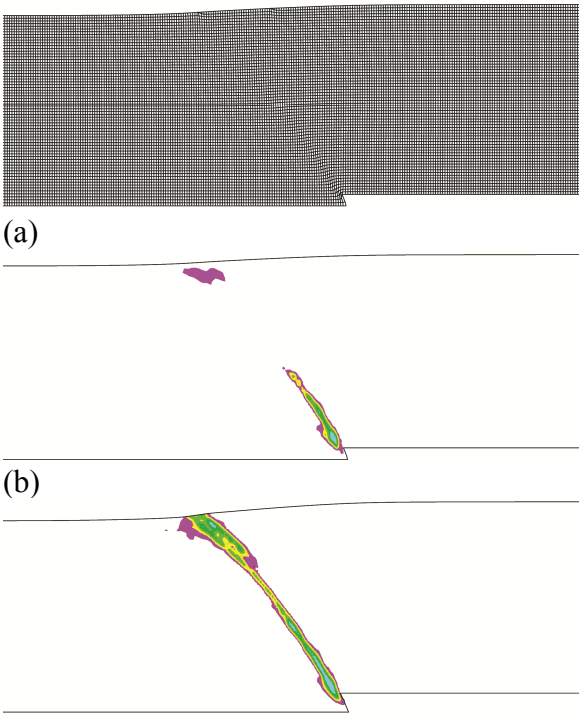

Figure 3-2. Modeling of the progression of fault rupture through previously unfaulted soil (reverse fault, 60° dip, 15 m-deep soil, $N_{1,60}$=22, K_0=0.45): (a) representative deformed mesh; (b) contours of post-peak shear strain after 0.9 m of vertical fault movement; and (c) after 1.5 m of vertical fault movement. Note: the lateral extent of the domain has been cropped.

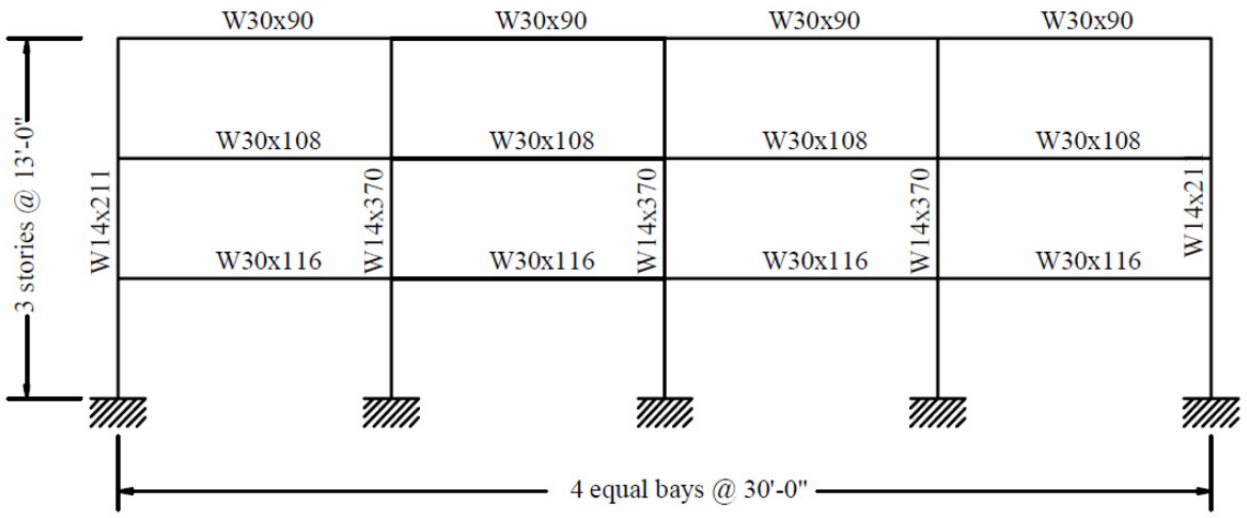

Figure 3-3. The three-story model structure used herein (Lee et al. 2004). The fourth bay, however, was omitted for use in this thesis. Each bay was assumed to be 10 m wide for a total structural model width of 30 m. The height of each story was assumed to be 4 m. The frame spacing was assumed to be the same as the bay width.

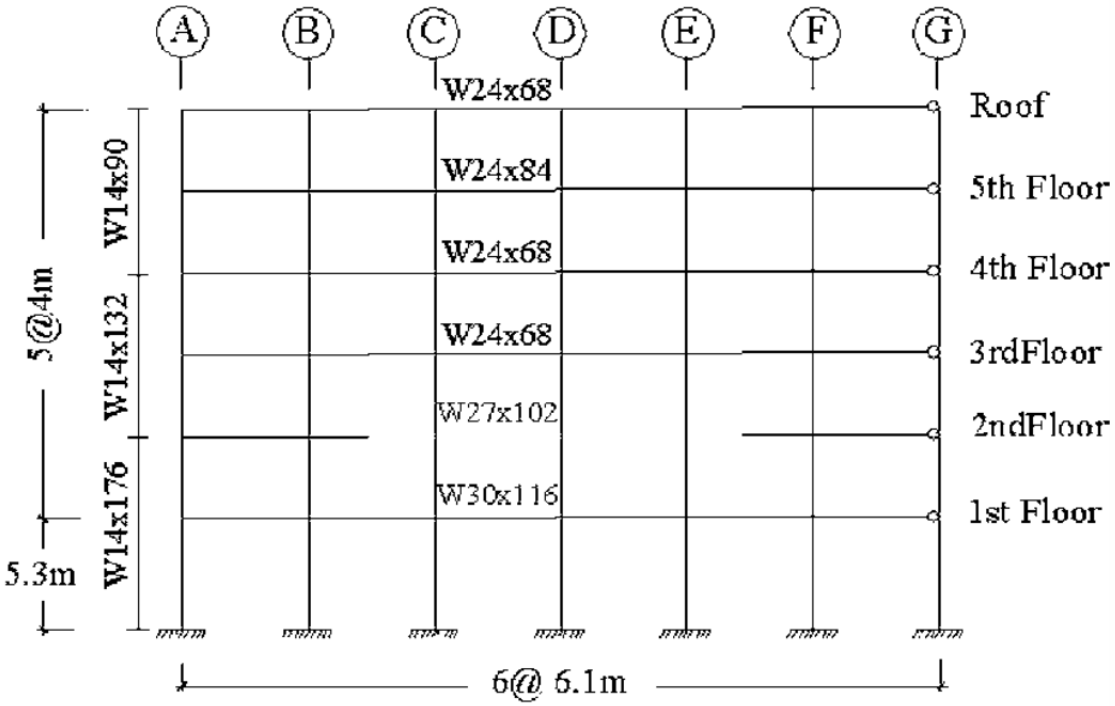

Figure 3-4. The six-story model structure used herein (Kalkan and Kunnath 2006). The frame spacing was assumed to be the same as the bay width.

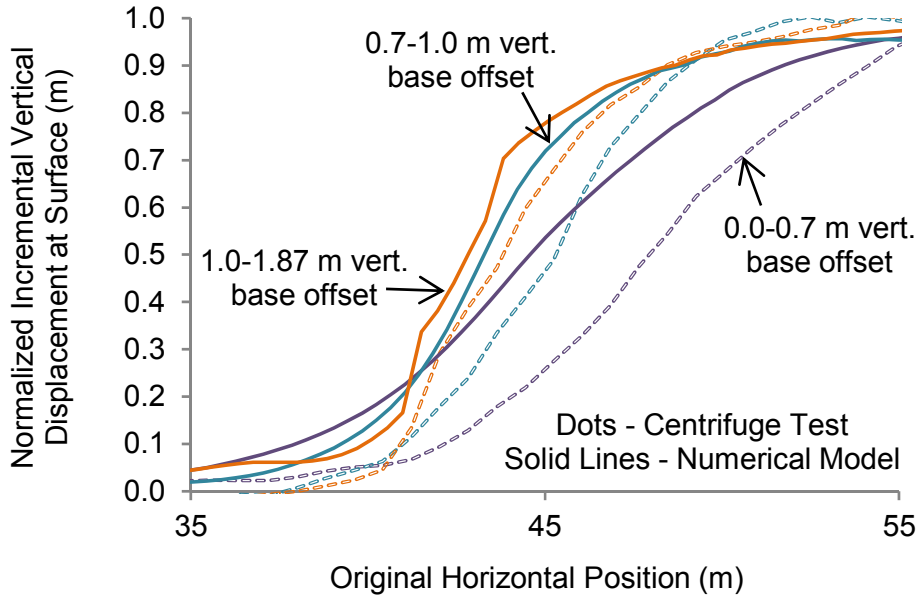

(a)

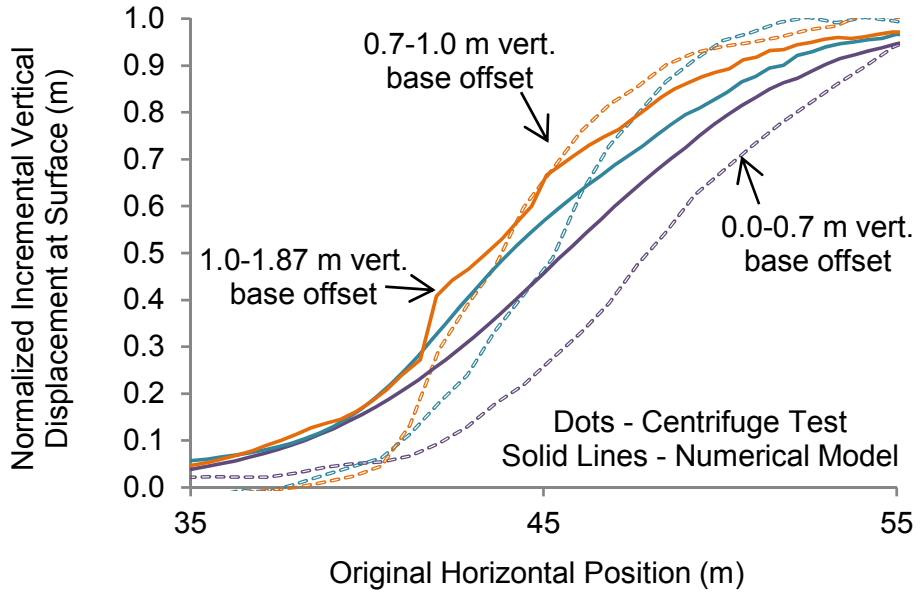

(b)

Figure 3-5. Incremental calibration of the numerical model (reverse fault, 60° dip, 15 m-thick soil deposit, $N_{1,60}$=22, K_0=0.45). with centrifuge test 28 from Bransby et al. (2008b): (a) reasonable match of the displacement at which a transition in the slope of the response changes (*hfac1*=0.025); and (b) a response too soft as evidenced by the surface deformation remaining at almost the same slope in each increment rather than increasing in slope (*hfac1*=0.015).

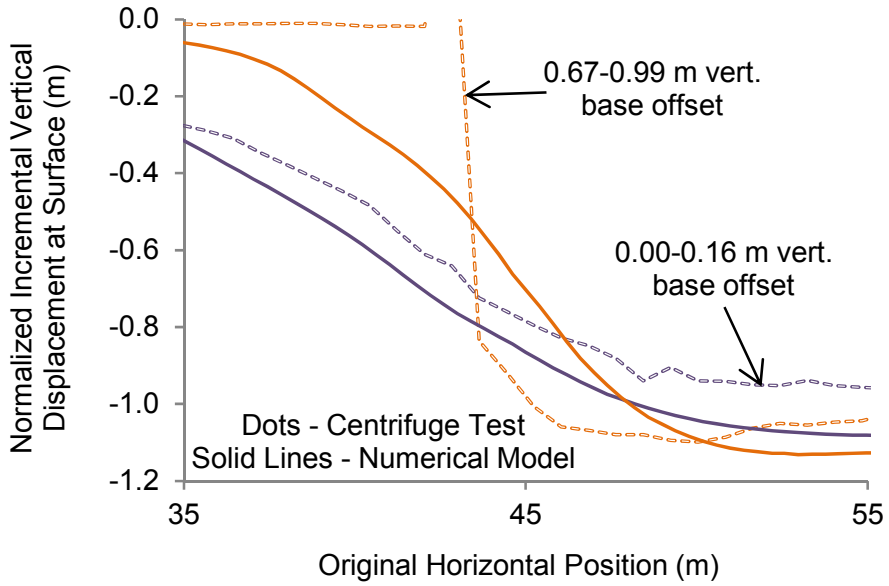

(a)

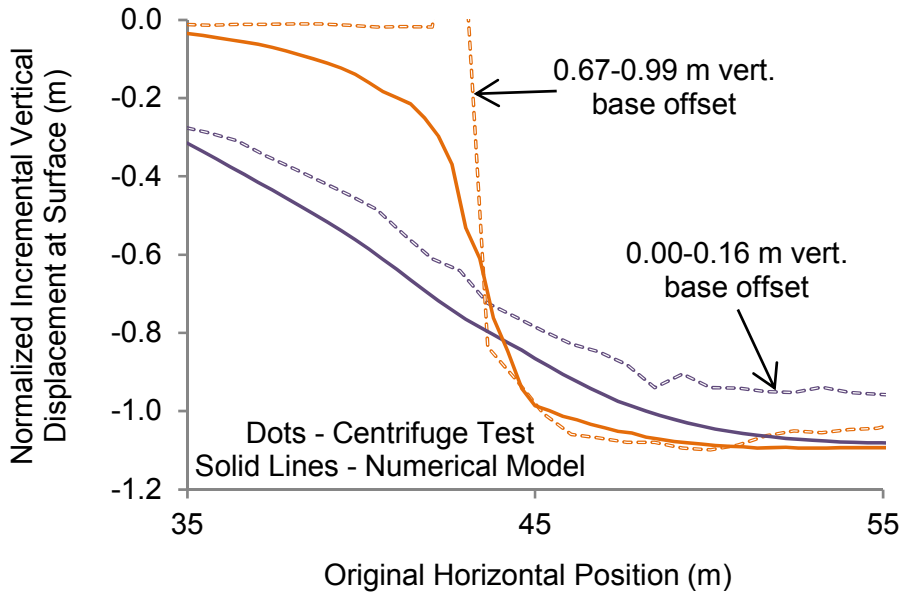

(b)

Figure 3-6. Incremental calibration of the numerical model (normal fault, 60° dip, 24.5 m-thick soil deposit, $N_{1,60}$=22, K_o=0.45). with centrifuge test 12 from Bransby et al. (2008a): (a) a mismatch in the slope of the post-peak surface response (*hfac1*=0.025; $100d_{50}$ to fully soften); and (b) a better match of the post-peak surface response steepness (*hfac1*=0.025; immediate fully softened response after peak stress).

(a)

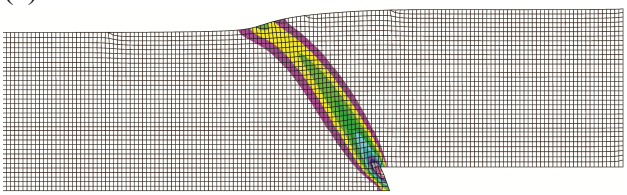

(b)

Figure 3-7. Validation of numerical model with centrifuge test 28 from Bransby et al. (2008b): (a) photograph of the centrifuge experiment; and (b) deformed mesh and shear strain contours for the numerical model (reverse fault, 60° dip, 2.2 m of vertical fault movement, 15 m soil, $N_{1,60}$=22, K_0=0.45). Note: the lateral extent of the domain on the left side has been cropped.

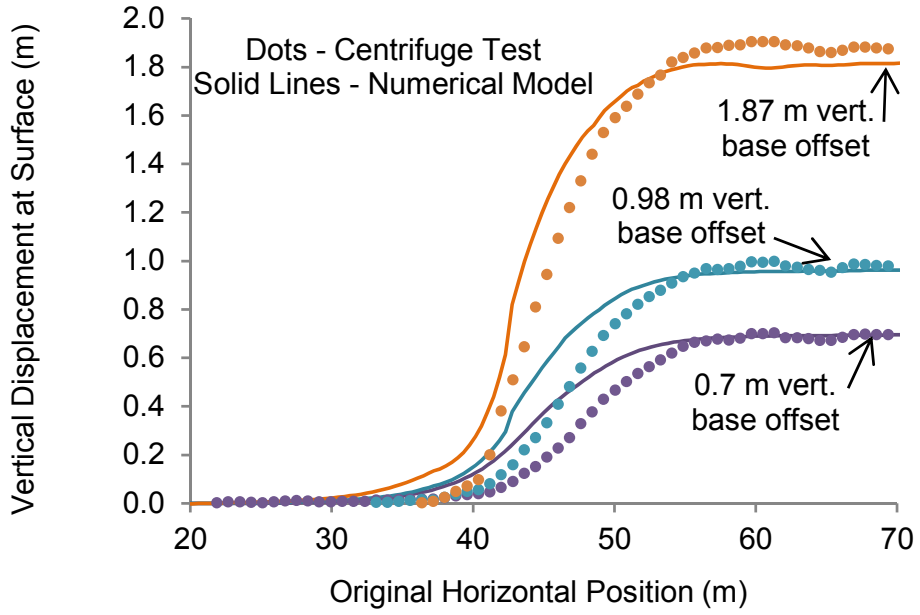

(a)

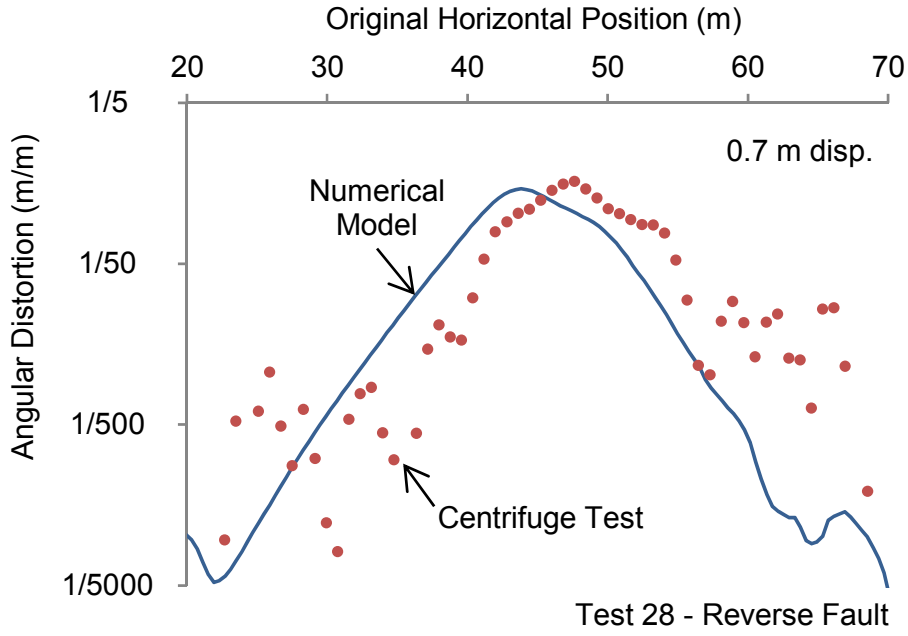

(b)

Figure 3-8. Comparison between centrifuge test (Bransby et al., 2008b) and numerical results for centrifuge test 28 (reverse fault, 60° dip, 15-m soil, $N_{1,60}$=22, K_0=0.45): (a) surface deformation; and (b) angular distortion.

(a)

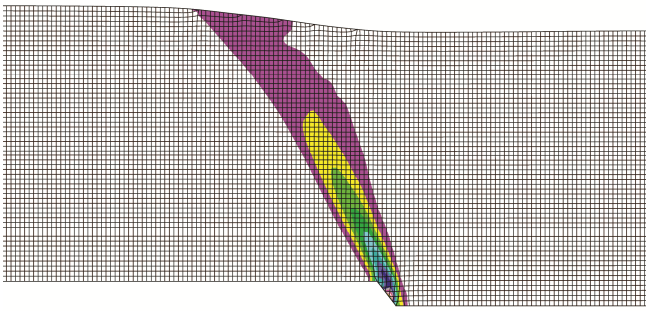

(b)

Figure 3-9. Validation of numerical model with centrifuge test 12 from Bransby et al. (2008a): (a) photograph of the centrifuge experiment; and (b) deformed mesh and shear strain contours for the numerical model (normal fault, 60° dip, 2.16 m of vertical fault movement, 24.5 m soil, $N_{1,60}$=22, K_0=0.45). Note: the lateral extent of the domain on the left side has been cropped.

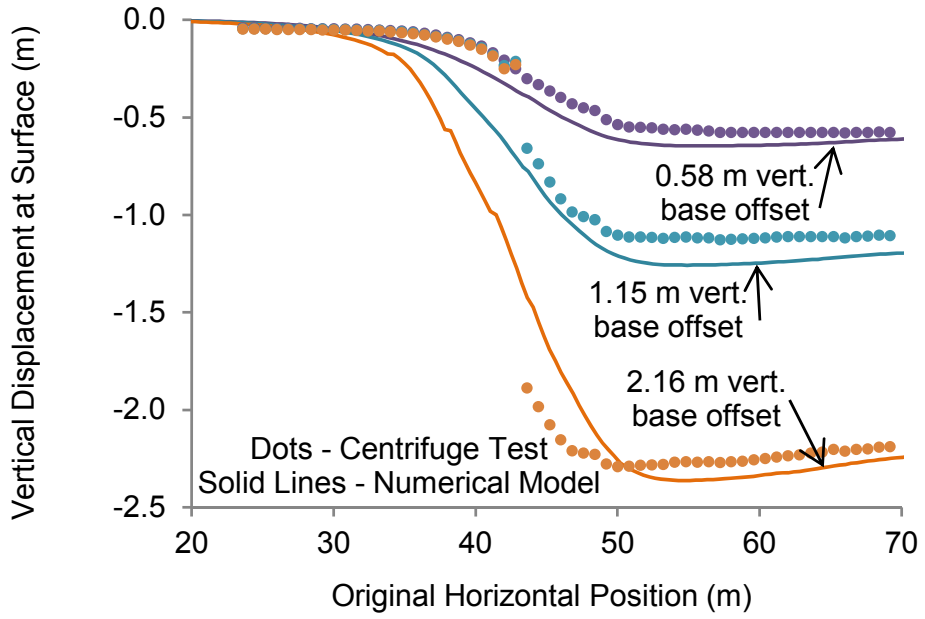

(a)

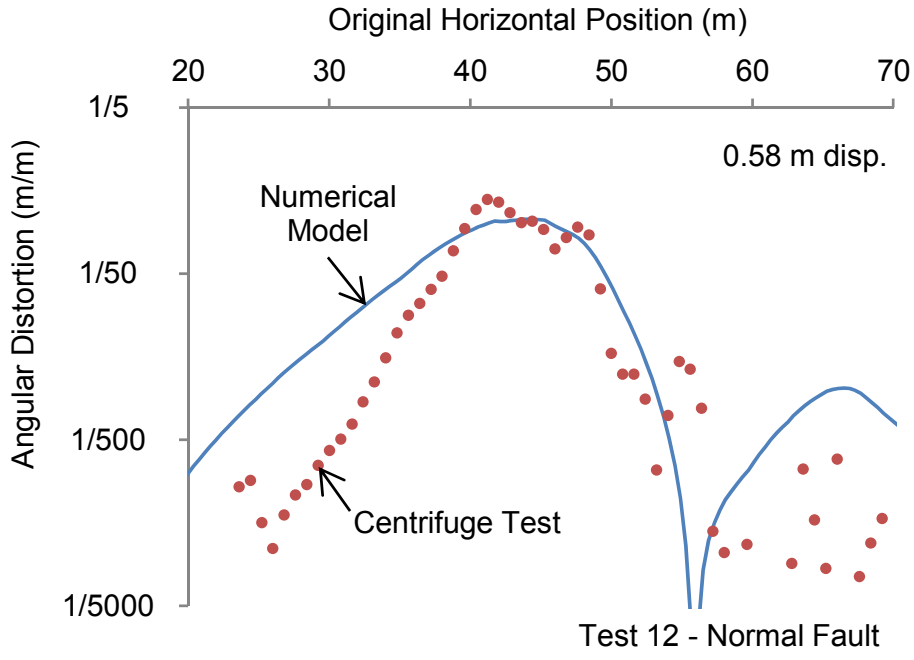

(b)

Figure 3-10. Comparison between centrifuge test (Bransby et al., 2008a) and numerical results for centrifuge test 12 (normal fault, 60° dip, 24.5-m soil, $N_{1,60}$=22, K_0=0.45): (a) surface deformation; and (b) angular distortion.

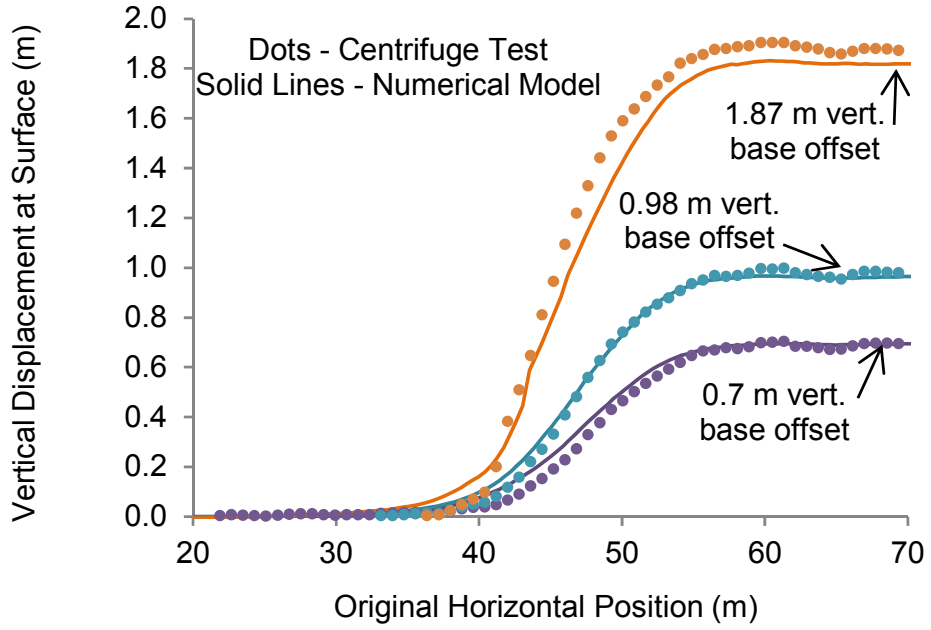

(a)

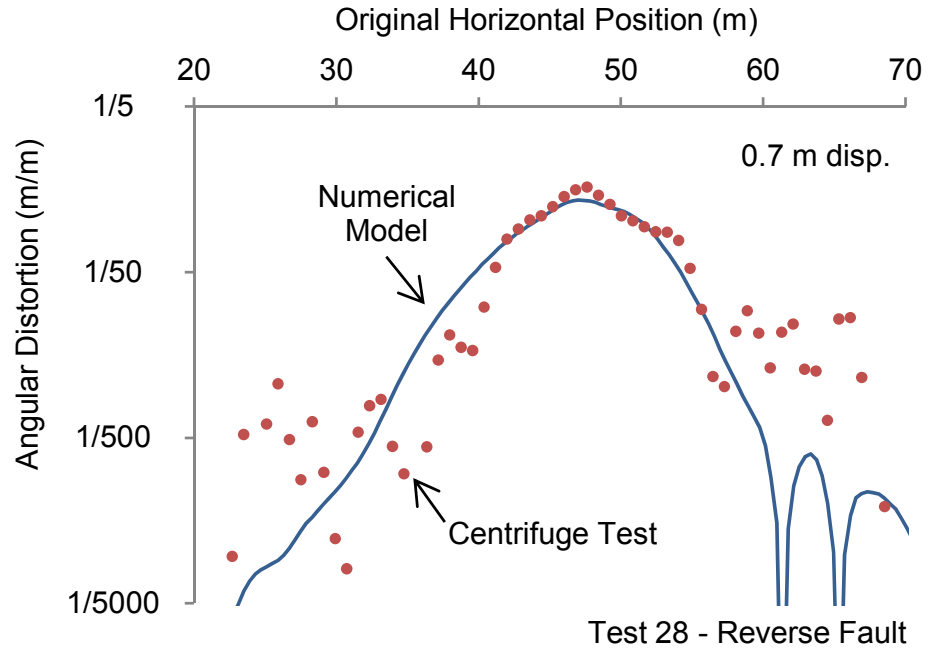

(b)

Figure 3-11. Improved fit between the numerical model and experimental data (centrifuge test 28, free-field reverse fault) when the characteristic line is adjusted with the parameter *hfac5*: (a) surface deformation; and (b) angular distortion.

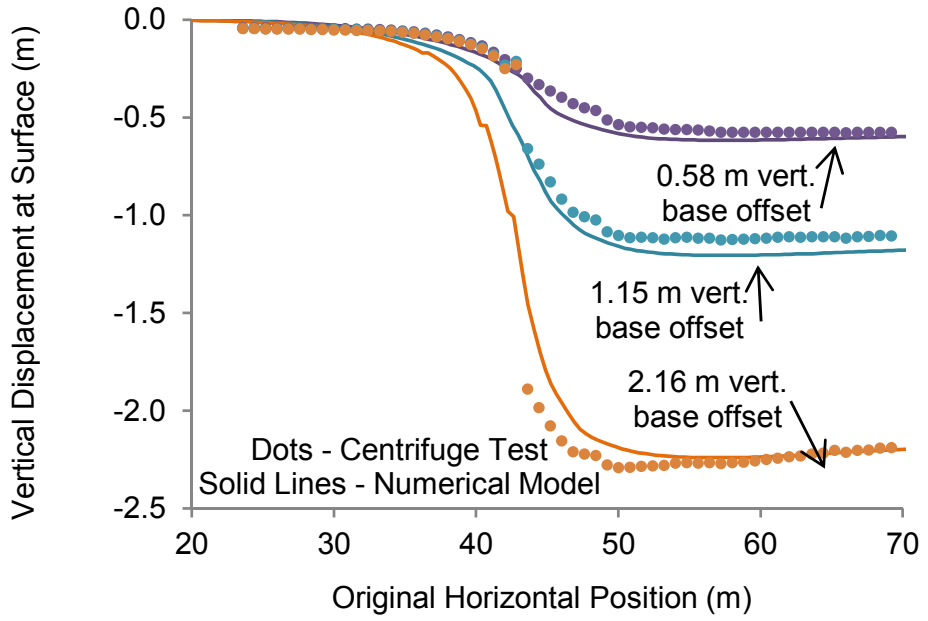

(a)

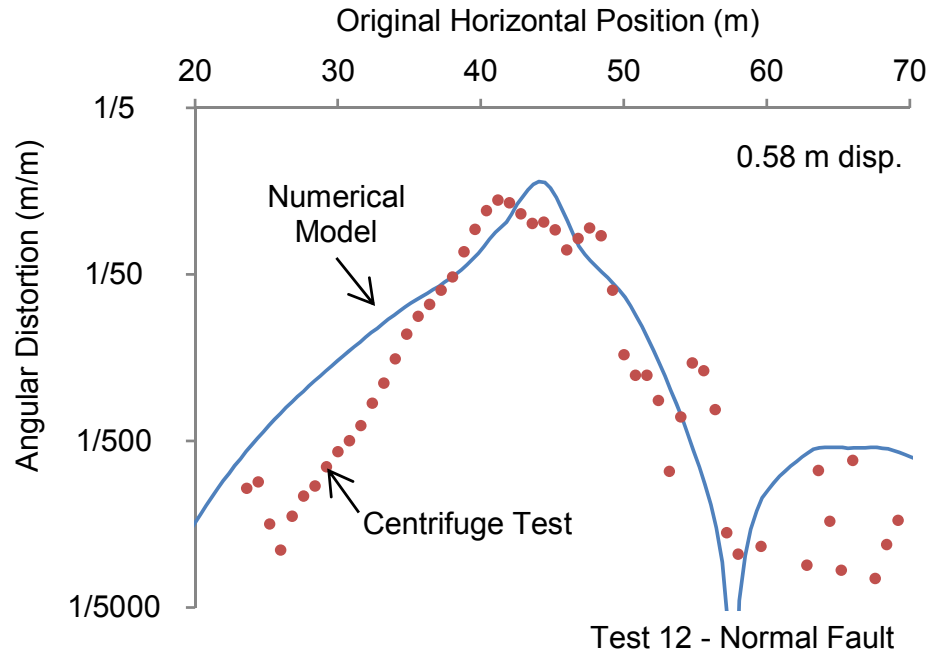

(b)

Figure 3-12. Improved fit between the numerical model and experimental data (centrifuge test 12, free-field normal fault) when the characteristic line is adjusted with the parameter *hfac5* and the post-peak localization is increased: (a) surface deformation; and (b) angular distortion.

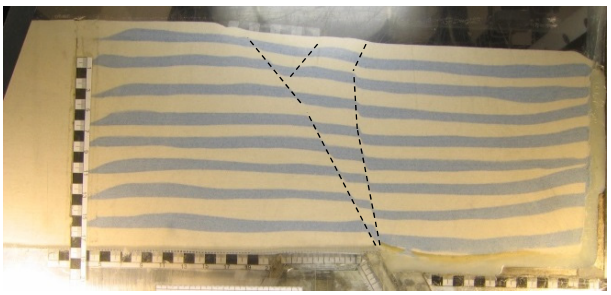

(a)

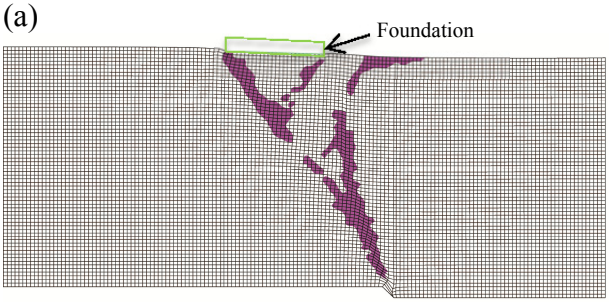

(b)

Figure 3-13. Validation of numerical model with centrifuge test 18 from Bransby et al. (2008b): (a) photograph of the centrifuge experiment; and (b) deformed mesh and strain softening contours for the numerical model (normal fault, 60° dip, 2.0 m of vertical fault movement, 24.5 m-thick soil deposit, $N_{1,60}$=24, K_0=0.45). Note: the lateral extent of the FE mesh on the left side has been cropped.

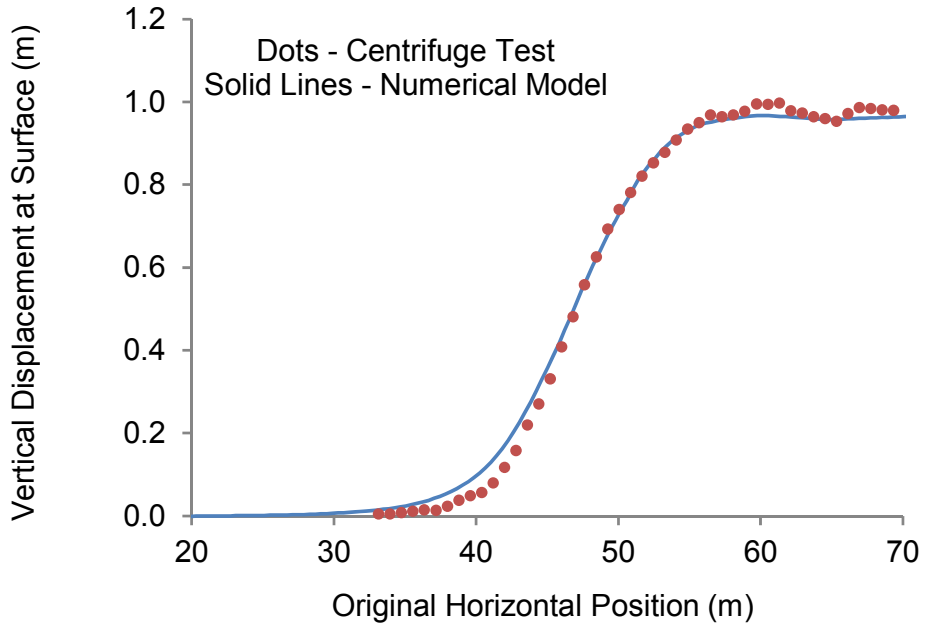

(a)

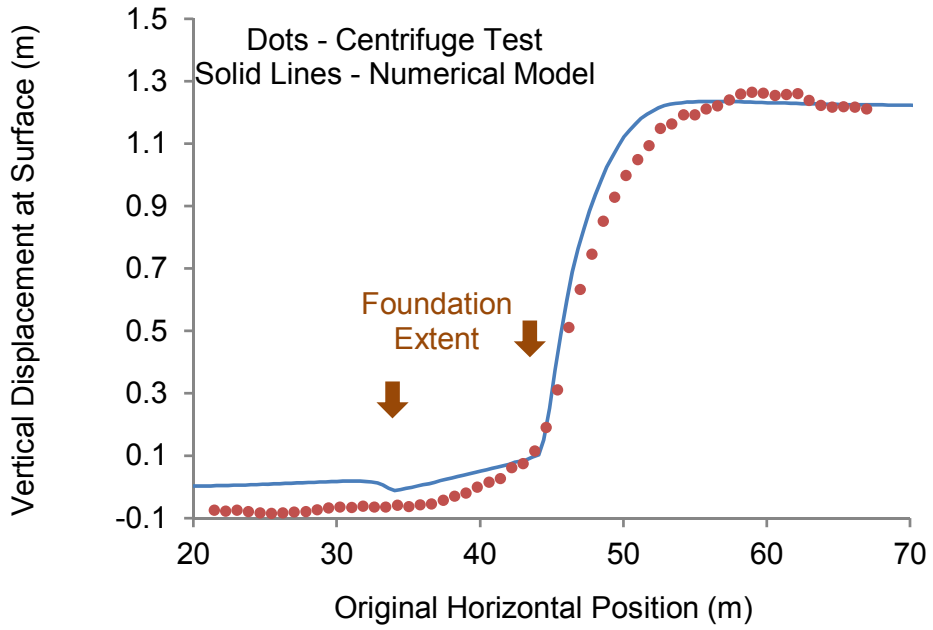

(b)

Figure 3-14. Comparison of free-field response and response with a structure for a reverse fault (a) Test 28 (free field); and (b) Test 29 (with structure).

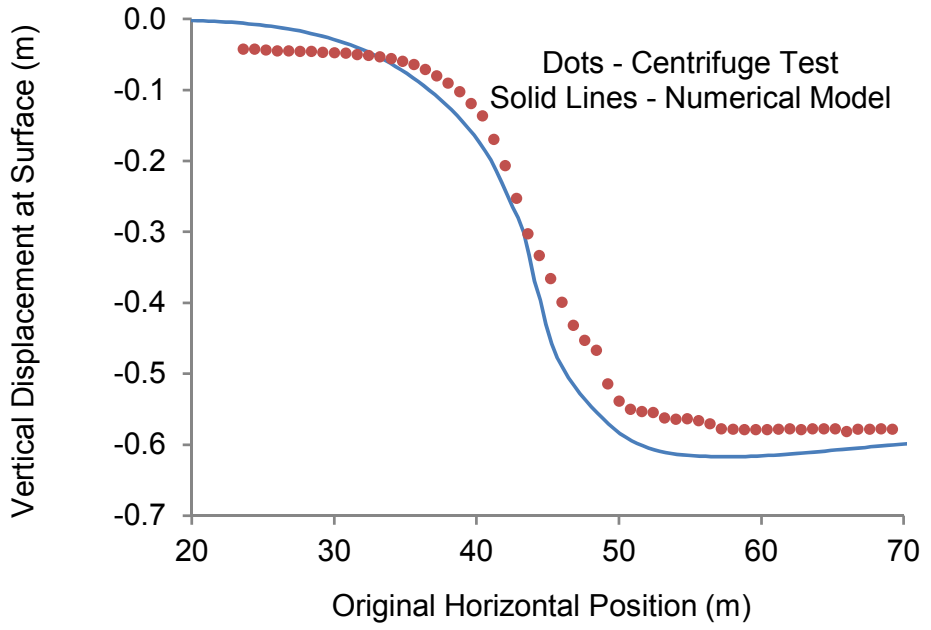

(a)

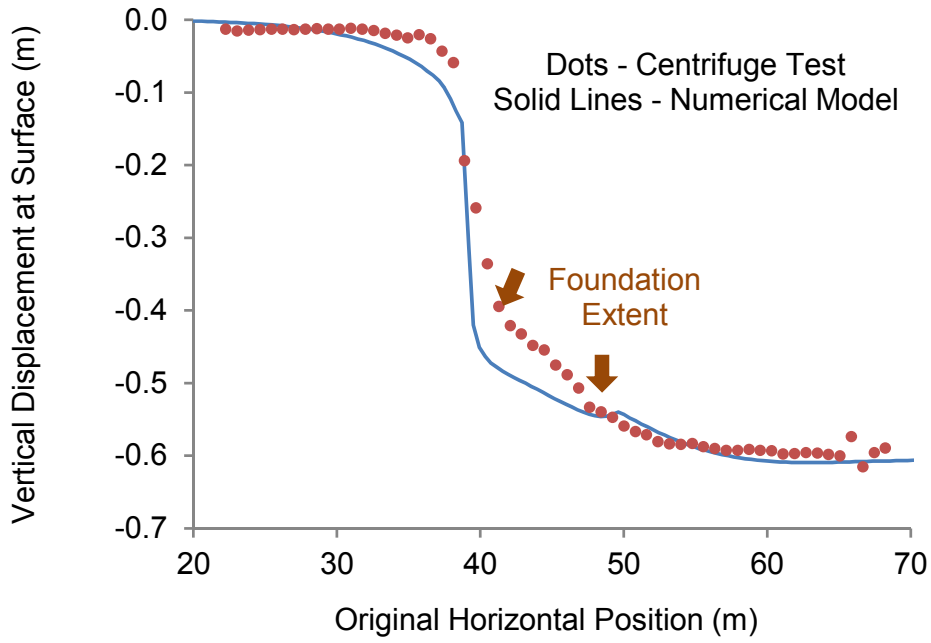

(b)

Figure 3-15. Comparison of free-field response and response with a structure for a normal fault (a) Test 12 (free field); and (b) Test 14 (with structure).

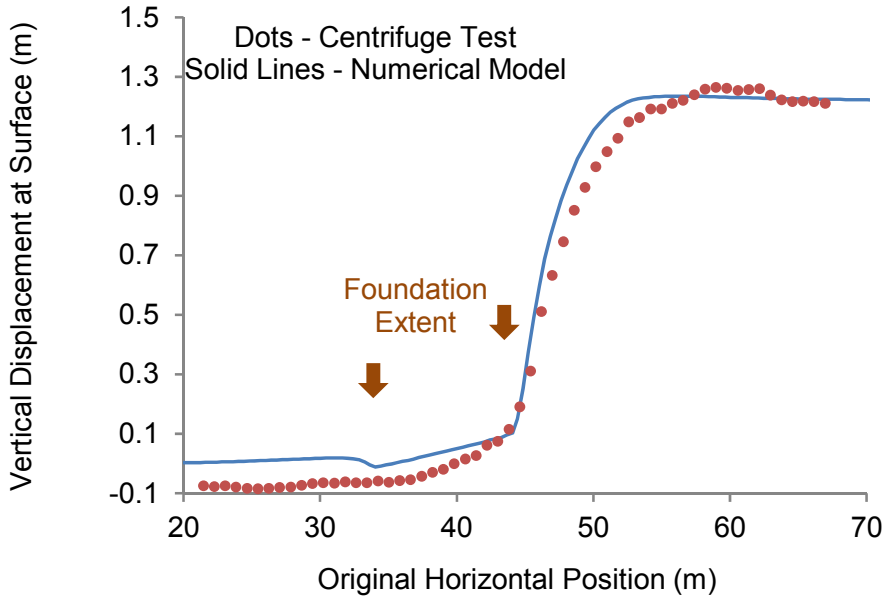

(a)

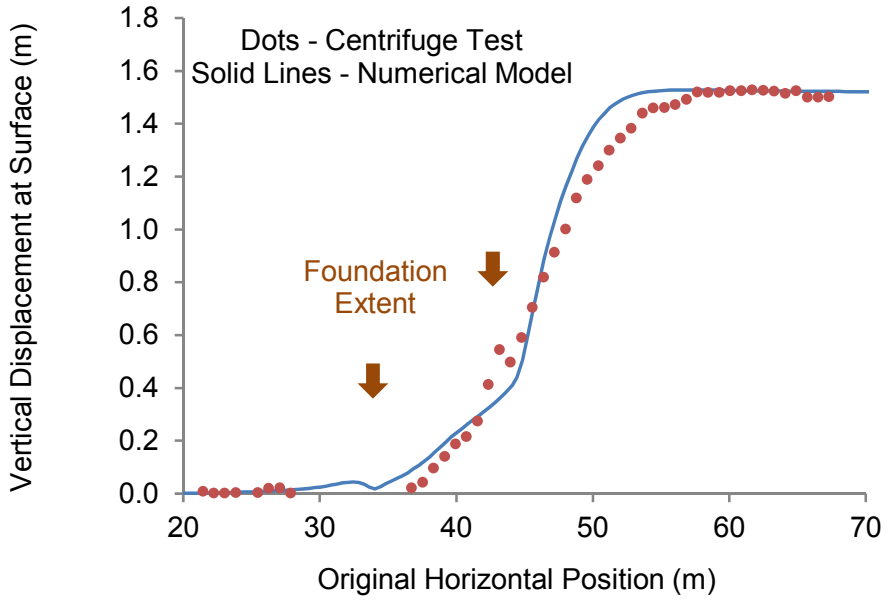

(b)

Figure 3-16. Comparison of response with a reference structure and a lighter structure for a reverse fault (a) Test 29 (reference structural configuration: 91 kPa); and (b) Test 30 (light structure: 37 kPa).

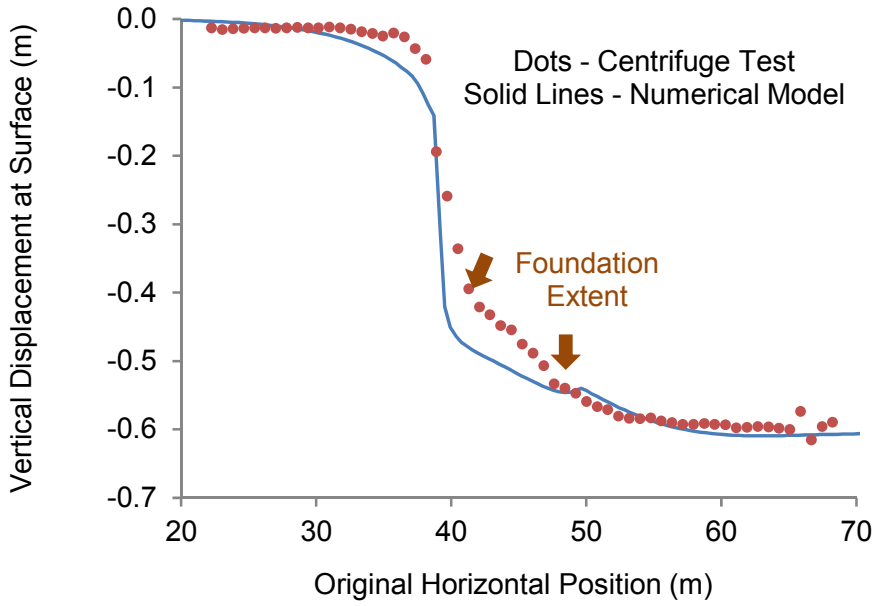

(a)

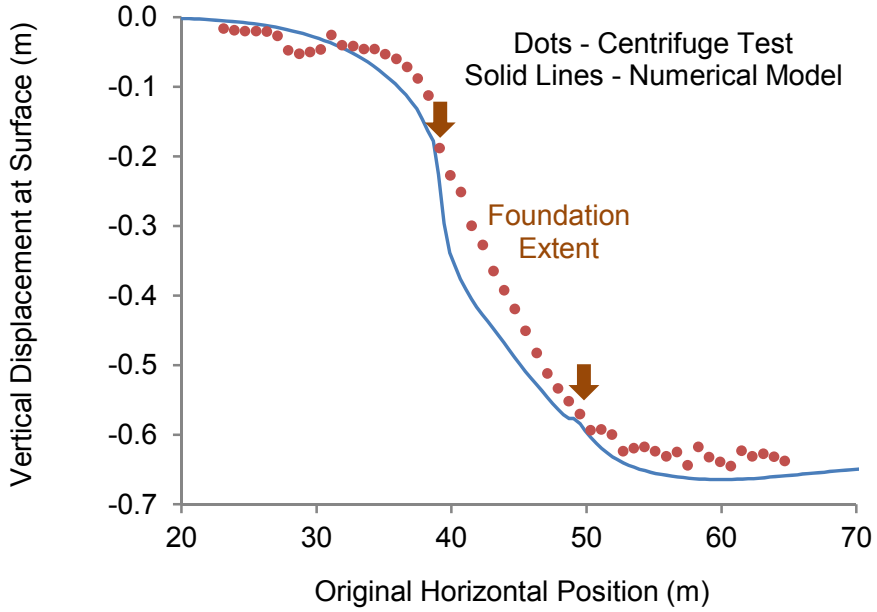

(b)

Figure 3-17. Comparison of response with a reference structure and a lighter structure for a normal fault (a) Test 14 (reference structural configuration: 91 kPa); and (b) Test 15 (light structure: 37 kPa).

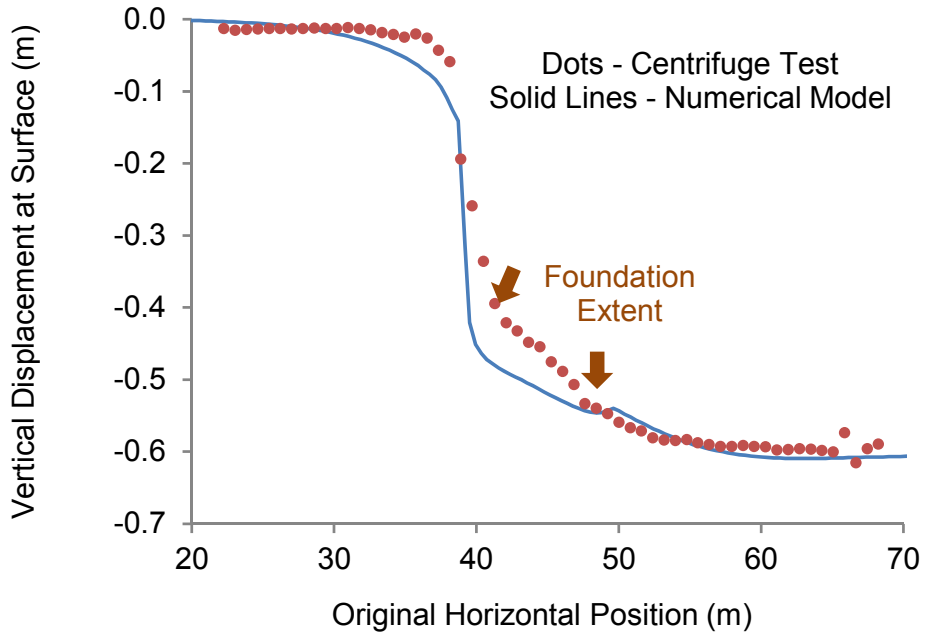

(a)

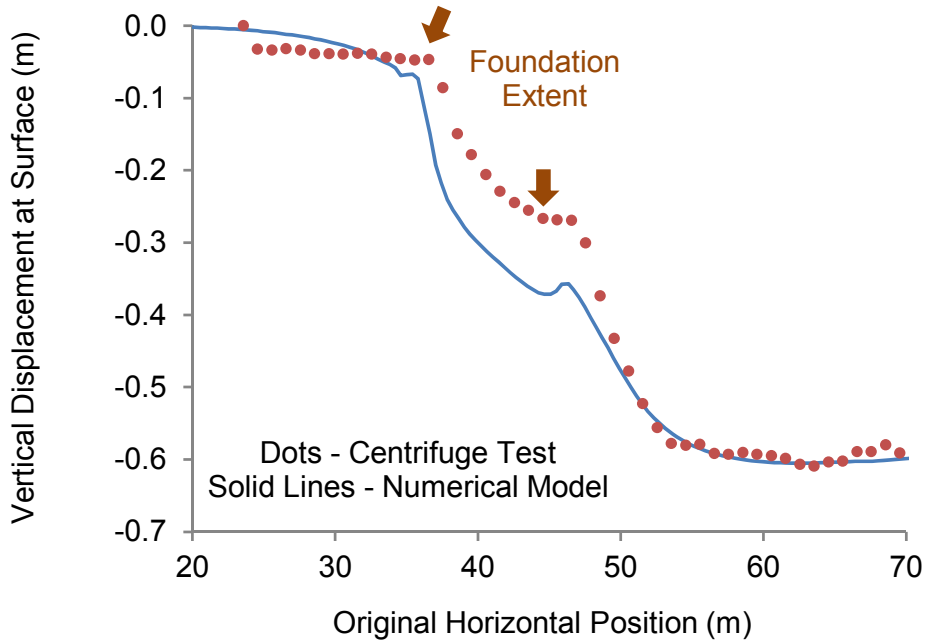

(b)

Figure 3-18. Comparison of response with a reference structure and a structure moved 5 m to the left for a normal fault (a) Test 14 (reference structural configuration); and (b) Test 18 (structure moved 5 m to the left).

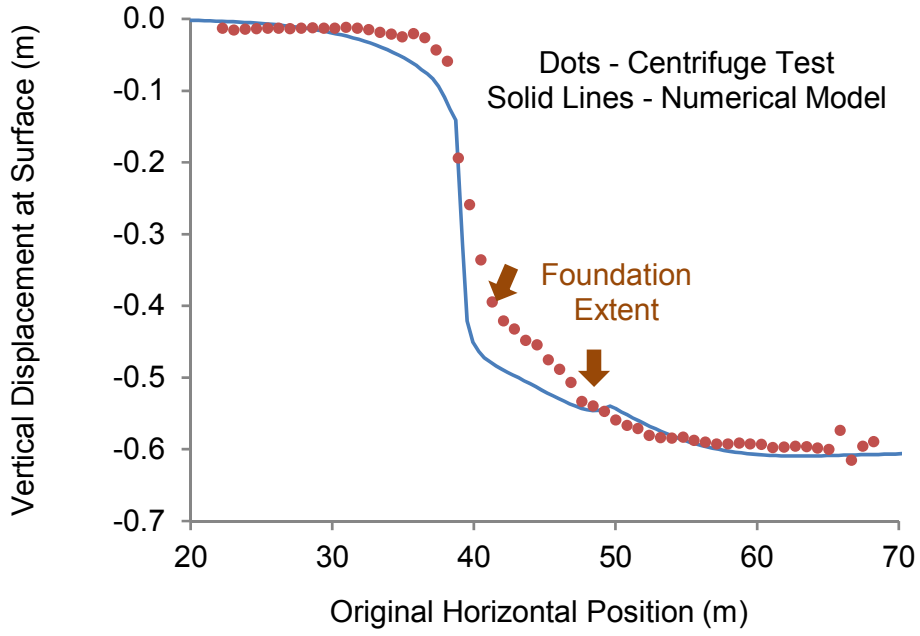

(a)

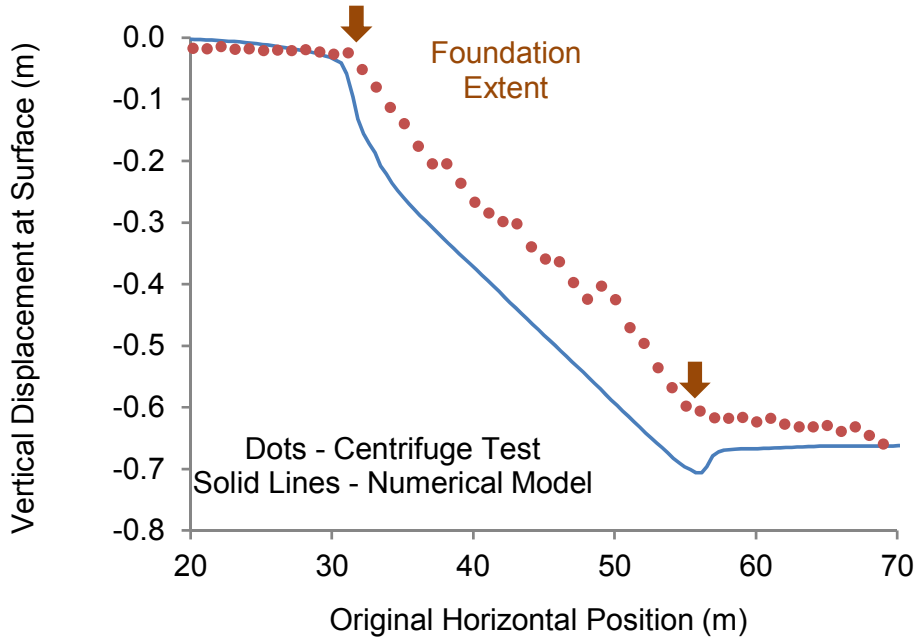

(b)

Figure 3-19. Comparison of response with a reference structure and a structure with a wider foundation for a normal fault (a) Test 14 (reference structural configuration: 10 m wide foundation); and (b) Test 20 (25 m wide foundation).

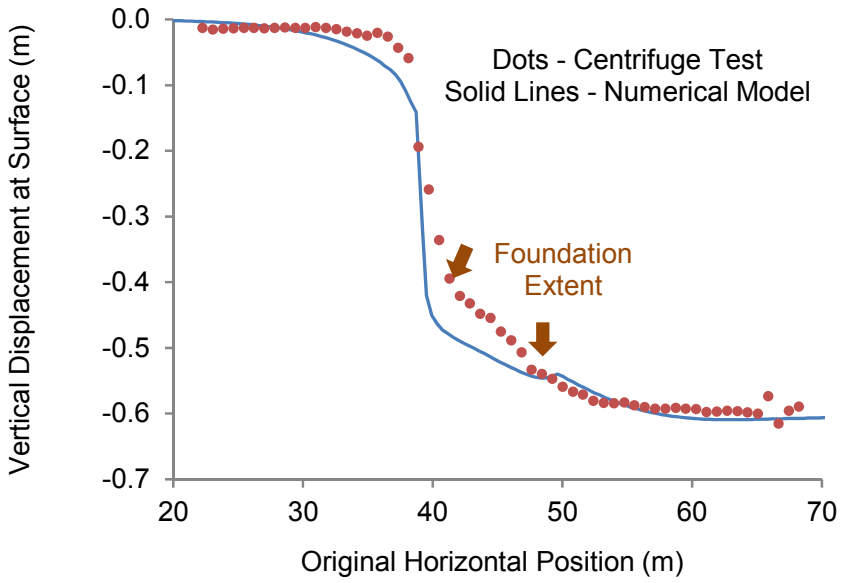

(a)

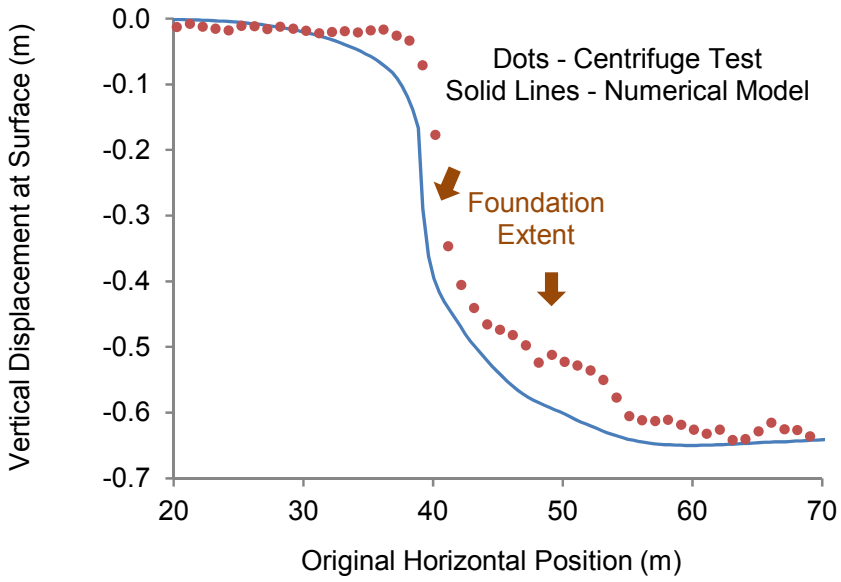

(b)

Figure 3-20. Comparison of response with a reference structure and a structure with a more flexible foundation for a normal fault (a) Test 14 (reference structural configuration that has a mostly rigid foundation); and (b) Test 22 (structure with a mostly flexible foundation).

CHAPTER 4: PRIOR RUPTURES

The majority of this chapter is directly taken from a manuscript accepted for publication in the Journal of Geotechnical and Geoenvironmental Engineering titled "Fault Rupture Propagation through Previously Ruptured Soil". Jonathan Bray is the only co-author of this manuscript.

4.1 Introduction

Surface fault rupture is an important design consideration in projects built across or adjacent to active fault traces. At times it is not possible to avoid active fault traces, and there is no need to avoid minor faults if proper mitigation measures are incorporated (e.g., Bray 2001, Cluff et al. 2003, Gazetas et al. 2008, and Bray 2009). A key to developing a rational design and mitigation framework for this hazard is to understand fully the mechanics involved in the surface fault rupture process. Researchers who have performed numerical modeling of earthquake surface fault rupture have generally found it is essential that the simulations incorporate soil stress¬-strain nonlinearity, a well-defined failure strain, and post-peak strain softening (e.g., Bray et al. 1994a,b; Bray 2001; Anastasopoulos et al. 2007,2008a; Loukidis et al. 2009).

In previous studies, the soil that overlies the bedrock fault has not been ruptured previously. When conducting physical testing, soil has been prepared by dry pluviation, moist tamping, or consolidation without pre-rupturing the soil before conducting the test of interest (e.g., Lade and Cole 1984, Bray et al. 1993, Johansson and Konagai 2006, Ha et al. 2008, and Bransby et al. 2008a,b). Numerical simulations performed previously assumed that the soil deposit had at-rest stress conditions without a weak shear band at critical state or with slicken-sided properties (e.g., Anastasopoulos et al. 2007, Gazetas et al. 2008, and Loukidis et al. 2009). This assumption is true for engineered fill placed over a fault, such as in the case of earth dams (Bray et al. 1992) or for the case of young unfaulted soils (as possibly occurred in the 2010 Darfield Earthquake). However, most faults are located by excavating trenches and identifying evidence of prior ruptures. At such sites, it is not appropriate to assume that no prior faulting has occurred when conducting physical or numerical analysis of surface fault rupture. The concept that fault-induced ruptures typically follow previous shear rupture zones is a well-known concept (Sibson 1977), and most faults have ruptured multiple times. Faults in bedrock often form features indicative of this continued damage such as fault gouge. The analogous effect in unconsolidated sediment, however, has not been explored fully. This study expands upon previous studies with a focus on investigating the fundamental response of soil during shearing as a result of dip-slip fault displacement with consideration of the ruptured soil deposit's stress and strain history.

Previous numerical modelers of surface fault rupture have used several soil constitutive models in their analyses. Bray et al. (1994b) employed the Duncan et al. (1980) hyperbolic model that incorporates stress–strain nonlinearity, stress-dependency, and importantly, a well-defined failure strain. However, it does not include dilation or strain softening. Anastasopoulos et al. (2007, 2009) and Loukidis et al. (2009) used Mohr–Coulomb models modified to include strain softening. Each of these modelers assumed that the soil was initially in an at-rest stress state and did not consider the presence of existing shear fault ruptures in the soil deposit.

Failure strain (i.e., soil brittleness or ductility) is an important soil parameter in this problem (Bray et al. 1994b). Dip-slip faults rupturing through ductile soil were found to delay the formation of a discrete offset at the ground surface. Ductile soils could "absorb" the underlying bedrock fault rupture and spread the fault offset across a broad zone of deformation at the ground surface. Brittle soils, however, form distinct shear bands from the bedrock fault to the ground surface after relatively little bedrock movement. While both ductile and brittle soils transmit fault movement to the surface, the key difference is the width over which that movement occurs and whether a distinct rupture plane has been formed.

Centrifuge modeling of surface fault rupture was conducted by Bransby et al. (2008a,b). At least 16 centrifuge tests were conducted on dry sand typically compacted to a relative density of 60%. The height of sand above the model base was between 15 m and 25 m in prototype scale. Both reverse and normal faults were modeled with and without foundations. The foundations were typically modeled as very stiff steel strip plates in addition to two flexible foundations. These foundations varied in width and applied load. These centrifuge tests, as documented in Bransby et al. (2008a,b) and with additional details provided by Gazetas and Anastasopoulos (personal communication, 2010), were used herein as a basis for calibrating and validating the numerical simulations presented in this paper.

4.2 Effects of Reverse and Normal Faulting on Soil State and Stress

Reverse Faults

The evolution of the state of stress in the soil deposit overlying a displaced bedrock fault was explored through the validated numerical simulations. Such results have not been reported thoroughly in the literature.

The developed shear band was found to project away from the bedrock fault at approximately the same angle as the fault dip. The dip of the shear band dip decreased slightly as it approached the ground surface. Stress ratio was calculated to be relatively high over a broad zone around the shear band. Principal stress orientations were calculated for reverse ruptures for the boundary conditions and model parameters specified previously (e.g., see UBCSAND parameters in Table 3-1). A representative stress pattern is presented in Figure 6. For normally consolidated, at-rest soil deposits with $K_0 = 0.45$, the principal stresses are rotated over a wide area, forming an "arch of stress" over the bedrock fault. In situ K_0 stress conditions are maintained away from the bedrock dislocation. A shear band is formed eventually in the center of the zone of high shear stress. The ground surface deformation response was highest at the outcropping location of this shear band and decreased away from the shear band on the hanging wall side of the fault. There was considerable less secondary ground deformation on the foot-wall side.

For an element in the center of the soil deposit in the location of the developing shear zone, the minor principal stress is increased until a near isotropic stress state is reached. Continued shearing causes the horizontal stress to exceed the vertical stress in the center of this region. As this occurs, the minor principal stress decreases and the major principal stress increases until a failure state is reached. This stress path is presented in Figure 7. The stress path of the soil in the location of the developing shear band (i.e., near the middle of the "arch of stress" zone) is most similar to the stress path of a plane-strain extension (loading) laboratory test

(as defined in Wood, 1990). However, the stress path also contains a component of minor principal stress reduction, unlike a typical plane-strain extension (loading) test. The stress path shown in Figure 7 for the case of a reverse fault is also somewhat analogous to Rankine passive earth pressure conditions. It should take relatively more bedrock fault displacement to mobilize fully the Rankine passive condition than the Rankine active condition. While the details of this stress path are likely affected by the soil constitutive model employed in the simulations, the general trends of the calculated extension and loading responses were found to be consistent with those observed in FLAC simulations using several simpler constitutive models (e.g., Mohr–Coulomb).

Normal Faults

In normal faults, principal stresses rotate in a relatively small zone near the rupture. The major principal stress in the rupture zone "bends over" slightly to accommodate shear along the rupture plane. Unlike for reverse faults (and high-angle dipping normal faults), low-angle dipping normal faults generate a second zone of high stress ratio antithetic to the primary rupture. A graben may or may not form in a high-angle dipping normal fault. In the case with a low-angle dipping normal fault, a graben is necessarily formed to accommodate kinematically curvature in the primary normal fault shear zone between the two zones of high stress ratio. Away from the fault, K_0 stress conditions are maintained. A representative stress pattern for the case of a normal fault rupture is presented in Figure 8.

The stress path in the shear zone during normal faulting can be represented by the plane-strain compression (unloading) shearing mode. The major principal stress remained almost constant while the minor principal stress decreased until failure. The major principal stress rotated slightly, but remained in a predominantly vertical direction. This stress path is also presented in Figure 7. The stress path shown in this figure for the case of a normal fault is also somewhat analogous to Rankine active earth pressure conditions, which can be contrasted to the case of the reverse fault movement discussed previously, which is somewhat analogous to the Rankine passive condition.

For the case of a vertical dip-slip fault movement, the stress paths were found to be in between those of the reverse and normal fault stress paths discussed previously. These stress paths were approximately vertical in the upward direction until dilation started to occur, and the major principal stresses were oriented in between the horizontal and vertical directions. This stress path is therefore more analogous to simple shear tests conducted in the vertical direction than to compression or extension tests. Since for a vertical fault the boundary conditions neither produce a net amount of extension or compression, the approximately vertical stress path was expected.

Care is required when modeling surface fault rupture, because the stress paths that form in a soil deposit overlying normal and reverse faults are quite different. This is especially so because the soil's failure strain should be smaller for the normal fault stress path than for the reverse fault stress path. The soil's failure strain varies for different stress paths using the same material parameters in the modified UBCSAND model used in this study. However, it may be necessary to use different material parameters to capture the dependence of failure strain and other key material responses as a function of stress path in some other cases.

Soil–Foundation–Structure Interaction

Anastasopoulos et al. (2009) described "hogging" and "sagging" soil–foundation-structure interaction modes for buildings with strip foundations in the fault rupture zone. In these analyses, there were similar tendencies for buildings to respond in one of those two ways (if conditions caused soil–foundation separation). When buildings are present, the schematic stress distributions shown previously in Figure 6 and 8 are largely maintained. Stress paths in the main shear band during surface fault rupture were found to be qualitatively similar to those of the free-field case. However, at both ends of the mat in the "sagging" case and in the center of the mat for the "hogging" case, large stress concentrations are added. This is shown schematically in Figure 9. In addition, secondary shear bands often develop with reverse fault movements as a result of soil–foundation-structure interaction. These two shear bands were found to propagate to the edges of foundation contact, as shown in Figure 9.

4.3 Effects of Previously Ruptured Soil Deposits

Methodology

To investigate the effects of previously ruptured soil deposits, a conventional bedrock fault rupture displacement analysis was performed as described previously until a distinct shear band had formed and produced a distinct surface offset. The FLAC model nodal displacements were then reset to zero while maintaining the fault rupture-induced stress state in the soil deposit, and the ensuing analysis of interest was performed. For the case of a 15 m-deep soil deposit with the soil parameters described in Table 3-1, approximately 2 m of bedrock fault offset was required to develop fully the shear band in the soil and to ensure that a distinct shear offset was produced at the ground surface. Thus, for all of the cases discussed herein, 2 m of bedrock fault offset was imposed before resetting nodal displacements to zero before the start of the analyses of fault rupture propagation through previously ruptured soil. Importantly, at the start of these later analyses, the stress state in the overlying soil deposit was not in the at-rest state. Instead, the soil's stress state was either as shown in Figure 6 for the case of reverse fault rupturing or in Figure 8 for the case of normal fault rupturing.

The initial stage of imposing the 2 m bedrock fault offset was performed in small-strain mode in FLAC, rather than in large-strain mode, because this allowed the establishment of a perfectly flat ground surface condition after pre-rupturing so that buildings could be easily placed on the ground surface. Some comparisons of the results using the small-strain mode and the large-strain mode for otherwise identical simulations of earthquake fault rupture propagation in FLAC are shown in Figure 10a. For the cases explored in this study, it is reasonable and practical to perform the initial stage of analysis in the small-strain mode and then perform the later analysis of the previously ruptured soil deposit in the large-strain mode. The two primary reasons why a numerical model calculates different results for the previously unruptured (virgin) case and for the pre-ruptured case is because of differing initial stress states within the soil deposit and the prior existence of shear banding for the latter case. Therefore, when resetting nodal displacements, the stress state was maintained and the strain-softened shear band was kept intact.

A series of analyses were performed in which the stress field was reset to K0 conditions and strain softening was disabled in the constitutive model to evaluate the relative importance of the initial stress state and the pre-existence of shear bands. The results of these analyses indicated that the dominant contributor to pre-rupture effects is the modified initial stress state, although the presence of the shear band is also important, and complicated interactions between these effects are possible. The key trends in the results of these analyses are shown in part in Figure 10b.

While a shear band would most likely remain intact from earthquake to earthquake, the stress state caused by faulting would likely evolve after an earthquake as a result of stress relaxation (Lade et al. 2010). Prior fault movements could also cause particle breakage in the shear band. The actual field case for surface fault rupture would likely be between that analyzed with this methodology and that analyzed from unruptured conditions. Alternatively, it may be reasonable to model prior ruptures and then partially, or fully, reset the soil stress state. However, then some judgment is required in resetting the soil stress state of the previously ruptured soil deposit. Additionally, intervening erosion, deposition, strong ground shaking, and other phenomena complicate the estimate of initial stress conditions at a site.

Effects of Prior Fault Ruptures on Soil Response

Using this methodology, a series of analyses were performed to assess the potential effects that prior ruptures might have on the characteristics of surface fault rupture. The same conditions described previously for the centrifuge test 28 of Bransby et al. (2008b) were analyzed to evaluate the differences between the cases of previously unruptured and ruptured soil. Representative results of the analyses of this test, compared to the numerical results for unruptured soil, are presented in Figure 11. The resulting ground surface deformation was far more localized for the case of previously ruptured soil than for the previously unruptured soil condition. Consequently, the maximum angular distortion was increased for the previously ruptured soil, but angular distortion away from the fault was reduced. These results indicate that, at least when soil–foundation–structure interaction is neglected, rational building setback distances based on a maximum permissible angular distortion threshold should be greater for previously unruptured soil deposits and smaller for previously ruptured soil deposits.

For very loose soils, distinct shear band formation is not expected because the soil is contractive. For such soils, broad zones of deformation are expected. Thus, the effects of prior ruptures might be minor for such cases. The results of the fault rupture propagation through soil analyses performed for the pre-ruptured and unruptured cases, as shown in Figure 12, confirm this hypothesis for the case of a loose sand deposit. As expected, 2 m of pre-rupture did not develop a distinct shear band nor did the soil undergo strain softening. Therefore, the resulting surface deformation profile was not markedly different than the deformation profile at the same site without previous ruptures. In contrast, dense soil deposits that are far more brittle than loose sand deposits (i.e., possess a lower failure strain), and they develop quickly failure stress conditions and a distinct shear band within the soil deposit. For the analysis presented in Figure 12, a notable difference between unruptured and previously ruptured soil was calculated for the case involving dense soil.

Effects of Prior Fault Ruptures on Structural Response

The effects of pre-rupturing were also assessed while considering soil–foundation–structure interaction effects. When the same conditions as centrifuge test 30 in the Bransby et al. (2008b) were modeled without pre-rupturing, the main shear band formed at the edge of the foundation, away from the free-field location, as shown in Figure 13a. Thus, the formation of the shear band in the soil deposit was diverted by the presence of the building. However, when prior shear rupturing was modeled before imposing additional bedrock fault displacement, the primary shear band was not diverted significantly by the building in the case analyzed, as shown in Figure 13b. Instead, the fault continued to develop along its original free-field path. The tilt of the building foundation was therefore increased, and an unsupported length developed, causing increased bending moment in the foundation. The change in structural response between previously unruptured and previously ruptured conditions continued to persist at greater amounts of fault displacement.

The relative effects of prior ruptures on a building located directly above the fault or slightly adjacent to the fault were assessed by modeling the case of the three-story building reported in Lee et al. (2004), which was described previously, under several different scenarios, two of which are discussed in this paper. In the first case, the moment frame steel structure was placed on top of the surface projection of a reverse fault and analyzed for both previously unruptured and previously ruptured conditions with a medium-dense sand deposit. In the second scenario, the building was placed on the footwall side of a normal fault with dense sand and analyzed for both previously unruptured and previously ruptured conditions. The results of these analyses for the reverse fault and normal fault cases are shown in Figure 14.

The structure placed directly on top of the surface projection of the reverse fault suffered approximately the same level of damage when the soil had already been ruptured compared to the previously unruptured condition when evaluated with the criteria in Son and Cording (2005) and when comparing the moments calculated in the superstructure. However, the structure sited adjacent to the normal fault suffered greater damage in the previously unruptured soil deposit condition as a result of more distributed fault rupture-induced ground deformation. The angular distortion of the ground (β, as defined in Son and Cording, 2005) was approximately 0.003 for the previously unruptured case and 0.001 for the previously ruptured case after approximately 2.1 m of vertical fault movement. Likewise, the additional moment demand in the second floor beam (defined as the beam above the ground floor) was approximately 630 kN-m for the previously unruptured case and approximately 280 kN-m for the previously ruptured soil deposit case. The differing responses of the structures for these cases emphasizes the importance of performing site-specific evaluations that consider critical factors such as fault type and geometry, amount of fault displacement, soil deposit characteristics, structural characteristics, location of the structure relative to the surface projection of the fault, and whether previous rupture events have modified the stress state and formed a localized shear rupture within the soil deposit.

4.4 Conclusions

Although previous researchers have studied how surface fault rupture might interact with structures, the potential effects of prior fault ruptures through the underlying soil deposit have not been investigated. Given that faults typically rupture multiple times in a semi-periodic

manner and given that soil response is affected by stress history and by the formation of shear bands, the potential effects of prior earthquake fault ruptures on fault rupture interaction with structures warrants investigation. This issue was explored in this paper employing numerical simulations validated by existing centrifuge data. The program FLAC with enhancements of the UBCSAND model that incorporated a well-defined failure strain and post-peak strain softening was shown to capture well the responses observed in a series of centrifuge tests performed by Bransby et al. (2008a,b).

In addition, a thorough examination of the primary modes of soil shearing during fault rupture and its effects on the soil deposit's stress state was studied. The numerical results demonstrate that the stress paths in the rupture zone are analogous to plane-strain extension (loading) and plane-strain compression (unloading) element tests for reverse and normal faults, respectively. The stress paths in vertical faults were found to be similar to a simple shear mode. In all cases, the state of stress in the fault rupture zone and the surrounding region were found to have evolved after the occurrence of bedrock fault ruptures, and distinct shear bands were also formed during fault rupture if the soil was dilatant.

The soil response to underlying bedrock fault rupture occurs in two distinct stages. First, broad deformation occurs before strain localization, which is followed by more localized deformation after shear band formation. Given that faults typically rupture multiple times in a semi-periodic manner and given that soil response is affected by stress history and by the formation of shear bands, for many dip-slip faults, the first stage of broad deformation may no longer occur, or may occur to a lesser extent, during subsequent events. The extent to which the initial stage of broad deformation could still occur despite prior surface fault ruptures is likely a function of how stress relaxation could impact the initial stress state in a fault zone.

Modeling of prior rupture events through soil was simulated by imposing a bedrock fault offset sufficiently large to develop fully the shear band and resulting stress state in the soil deposit. Ground deformation response at sites with prior ruptures was found to be more localized (i.e., angular distortion was greater at the fault outcrop but lower away from the fault trace). As a result, structural damage would be more severe if the structure was located directly above the surface projection of the bedrock fault, but damage would be less severe if it were located adjacent to the fault (when soil–structure interaction is ignored). In this set of analyses of dry sand deposits, there was no attempt to estimate the effects of stress relaxation between rupture events which could partially reset the developed stress state and cause increased distributed deformation. The amount of stress relaxation in a soil deposit depends on many factors, including soil type, time, and creep. In practice, it would be difficult to estimate the amount of stress relaxation reliably, so both cases of no and full stress relaxation would likely need to be considered.

Several cases of soil–structure¬–interaction were analyzed. In one case, a structure built directly on top of a pre-existing fault did not divert the fault rupture around the building, because the soil deposit was previously ruptured. However, in another scenario where the structure was placed directly on top of the projection of the fault, the previous rupturing of the soil was found to have a minimal effect on the damage induced in the structure. When the structure was placed adjacent to the fault, significantly lower building damage was calculated when previous rupturing occurred, as expected based upon lower angular distortion calculated for the free-field case for ground away from the fault.

Thus, previous rupture events can significantly affect soil and structural responses to earthquake fault rupture. The effects of prior fault rupture events can be potentially detrimental or beneficial from the standpoint of structural performance in the near-fault vicinity. Therefore, the potential effects of prior fault ruptures need to be considered in evaluations of the response of structures to surface fault rupture when previous events have likely ruptured through an existing soil deposit.

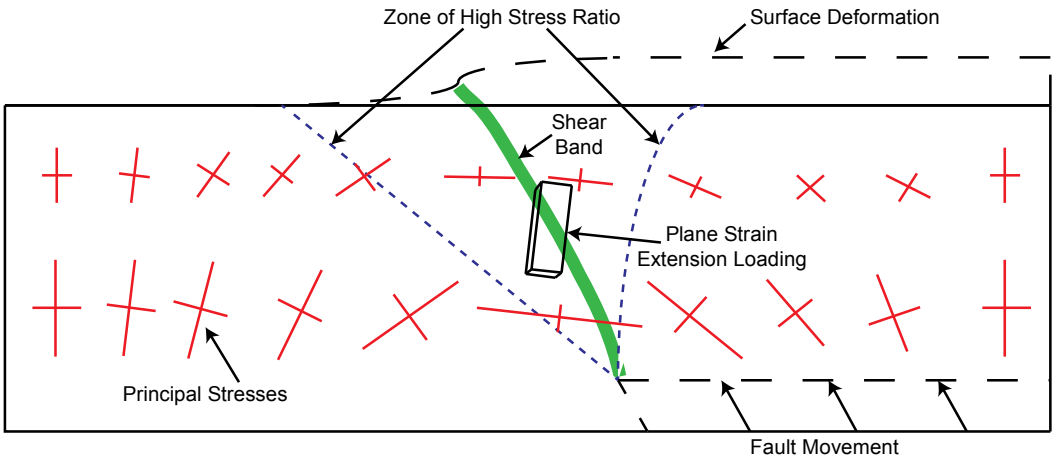

Figure 4-1. Schematic of soil response and shear band development as a result of a reverse fault rupture through dry sand (60° dip, 15 m soil, 0.7 m of vertical fault movement, $N_{1,60}$=34, K_0=0.45, previously unfaulted soil).

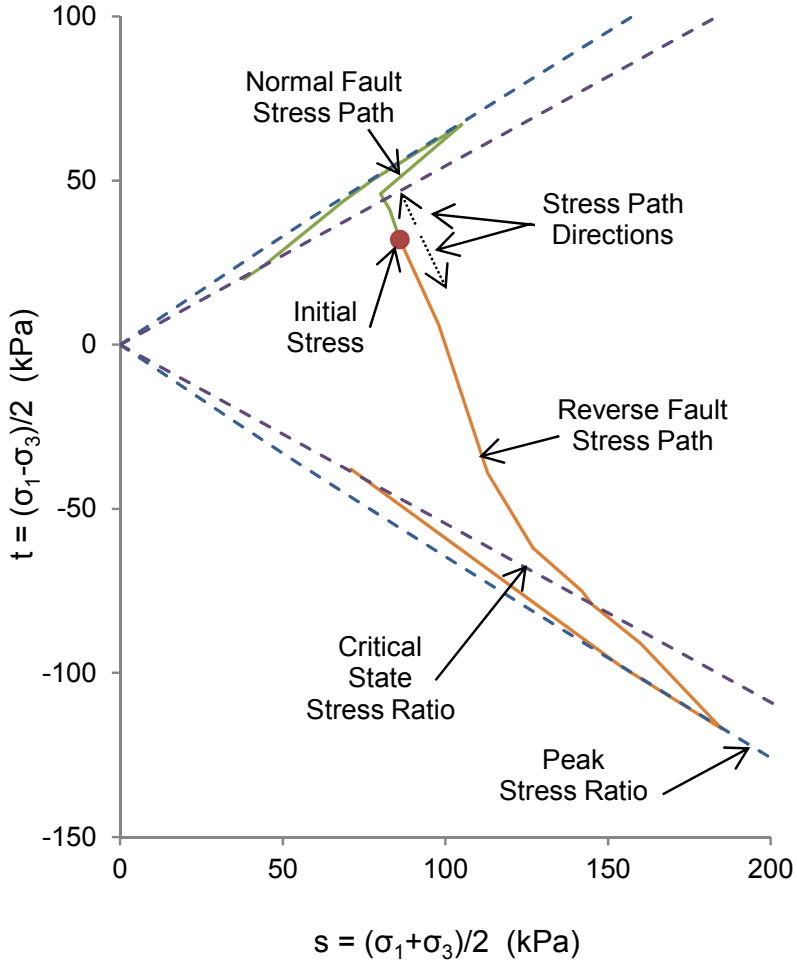

Figure 4-2. Stress paths for reverse and normal fault ruptures (located by the elements shown in Figures 6 and 8) where shear stress is taken as negative when the major principal stress is more horizontal than vertical.

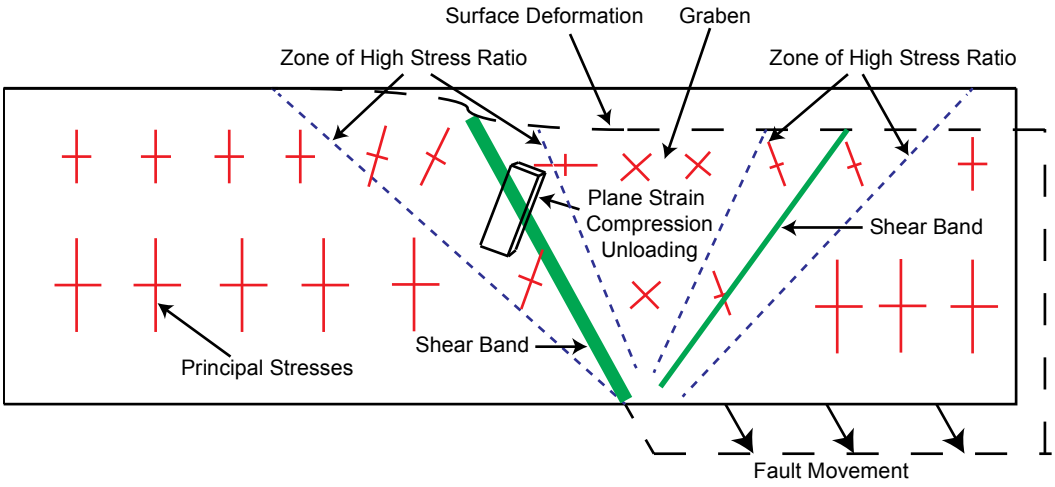

Figure 4-3. Schematic of soil response and shear band development as a result of a normal fault rupture through dry sand (60° dip, 15 m soil, 0.5 m of vertical fault movement, $N_{1,60}$=34, K_0=0.45, unfaulted soil).

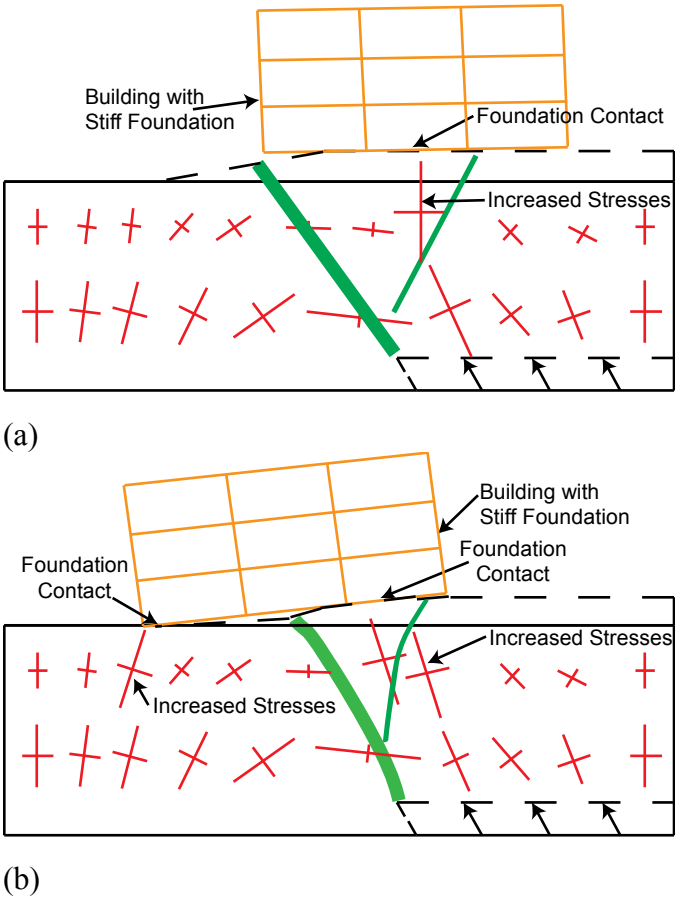

Figure 4-4. Schematic of soil–structure response over a ruptured fault after shear band development (reverse fault, 60° dip, 15 m soil, 2.0 m of vertical fault movement, $N_{1,60}$=50, K_0=0.45, unfaulted soil, three-story steel moment frame structure): (a) hogging-type soil–structure interaction; and (b) sagging-type soil–structure interaction.

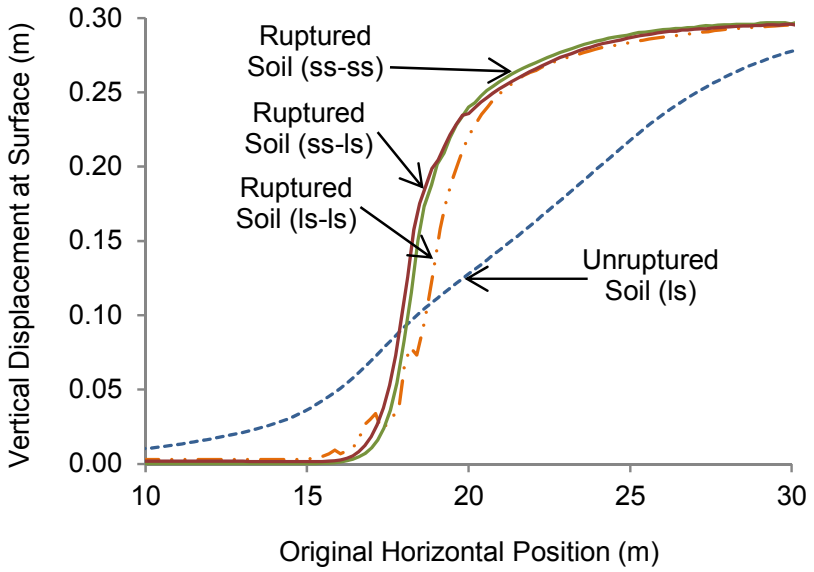

(a)

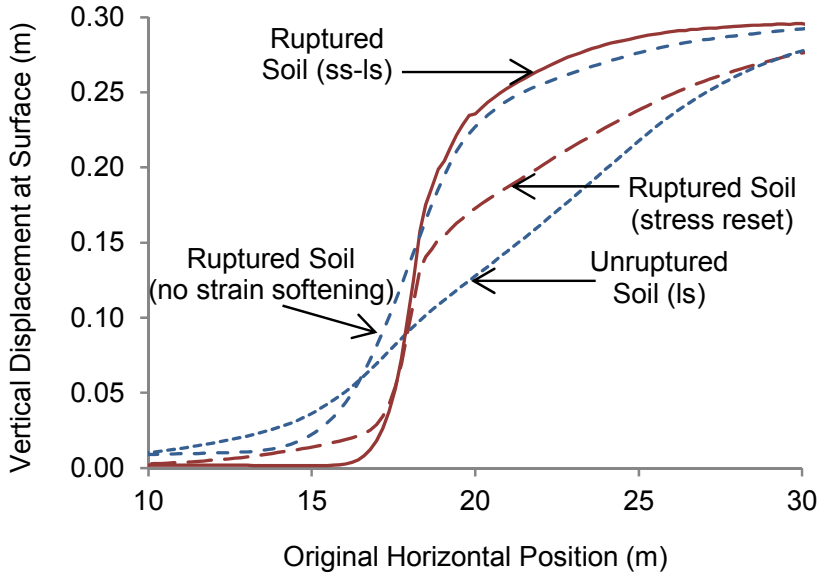

(b)

Figure 4-5. (a) Comparison of numerical techniques for capturing previous faulting effects (reverse fault, 60° dip, 15 m soil, 2 m of previous vertical fault movement, $N_{1,60}$=22, K_0=0.45): pre-rupture in large-strain mode and continue in large-strain mode (ls-ls), pre-rupture in small-strain mode and continue in large-strain mode (ss-ls), and pre-rupture in small-strain mode and continue in small-strain mode (ss-ss); and (b) effects of prior ruptures when strain softening is disabled in the constitutive model and when the stress state is reset to K_0 conditions after pre-rupturing.

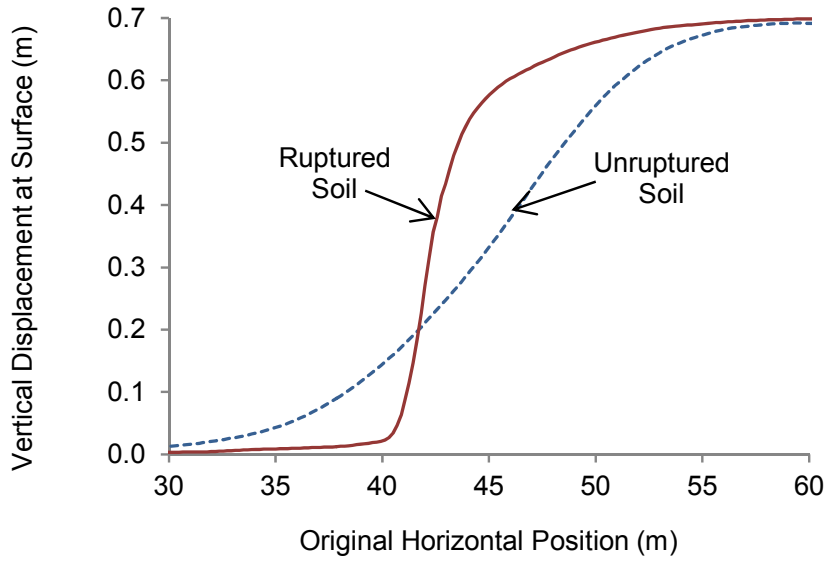

(a)

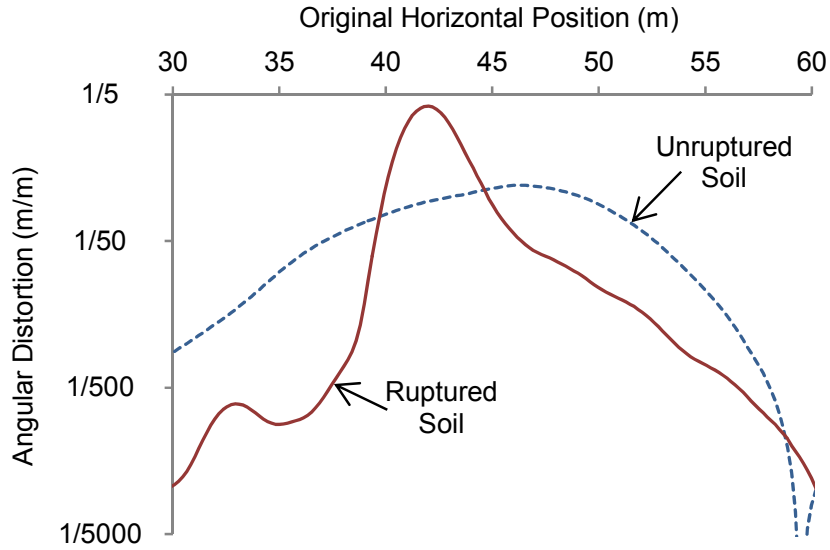

(b)

Figure 4-6. Comparisons between unruptured and previously ruptured soil for the same conditions as centrifuge test 28 (reverse fault, 60° dip, 15 m soil, 2.0 m of previous vertical fault movement, 0.7 m of vertical fault movement, $N_{1,60}$=22, K_0=0.45): (a) surface deformation; and (b) angular distortion.

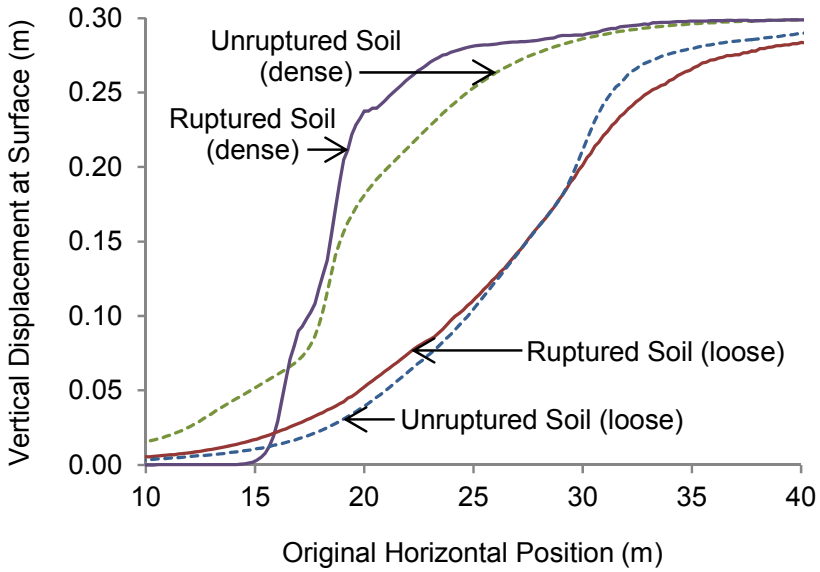

Figure 4-7. Comparison between unruptured and previously ruptured soil for loose and dense sand (reverse fault, 60° dip, 15-m soil, 2.0 m of previous vertical fault movement, $N_{1,60}$=8/50, K_0=0.45).

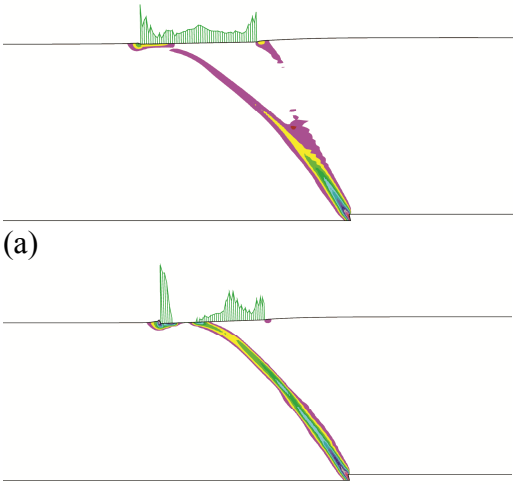

Figure 4-8. Comparison between unruptured and previously ruptured soil for the same conditions as centrifuge test 30 (reverse fault, 60° dip, 15 m soil, 2.0 m of previous vertical fault movement, 0.74 m of vertical fault movement, $N_{1,60}$=31, K_0=0.45, 10 m wide mat, 37 kPa mat load) showing contours of shear strain and magnitude of foundation contact stress: (a) unruptured soil; and (b) previously ruptured soil. Note: The lateral extents of the domain have been cropped.

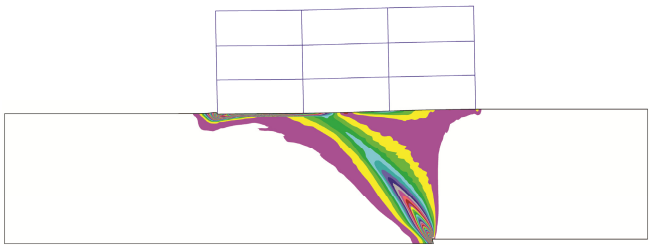

(a)

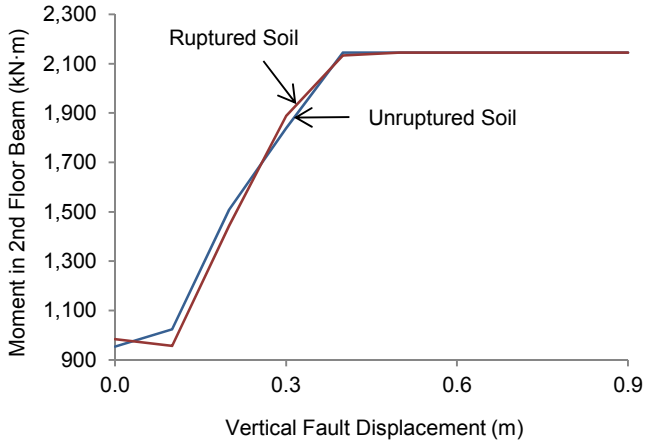
2,300
2,100
1,900
1,700
1,500
1,300
1,100
900
Moment in 2nd Floor Beam (kN·m)
Ruptured Soil
Unruptured Soil
0.0
0.3
0.6
0.9
Vertical Fault Displacement (m)

(b)

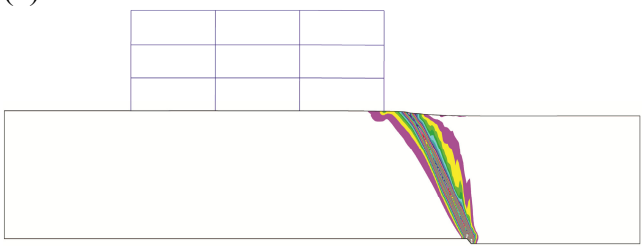

(c)

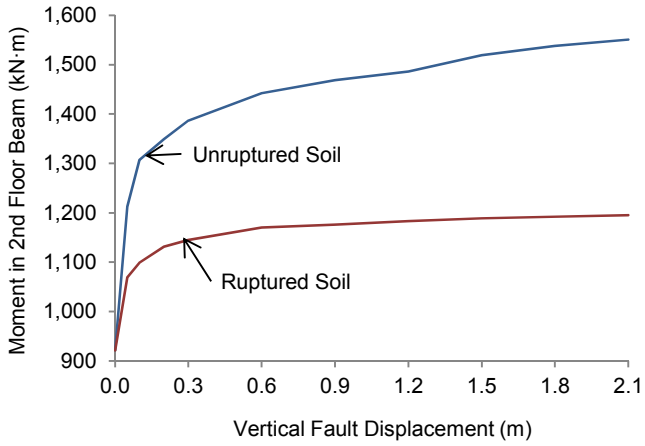

(d)

Figure 4-9. Responses of structures for previously unruptured and previously ruptured soil deposits: (a) contours of shear strain in the unruptured case (reverse fault, 60° dip, 15 m-deep soil deposit, 0.6 m of vertical fault movement, $N_{1,60}$=22, K_0=0.45, structure described in Lee et al. (2004) with a 0.45 m-thick mat foundation); (b) bending moment response in the structure for the reverse fault case; (c) contours of shear strain in the unruptured case (same as previous case except for a normal fault, with the building moved 15 m further from the fault trace, and $N_{1,60}$=35); and (d) bending moment response in the structure for the normal fault case.

CHAPTER 5: GEOTECHNICAL MITIGATION

The majority of this chapter is directly taken from a manuscript accepted for publication in the Journal of Geotechnical and Geoenvironmental Engineering titled "Geotechnical Mitigation Strategies for Earthquake Surface Fault Rupture". Jonathan Bray is the only co-author of this manuscript.

5.1 Introduction

Surface fault rupture is an important hazard that must be addressed when designing or evaluating structures built in areas with shallow active faults. Active fault traces at the ground surface exist in several urban areas including Los Angeles, the San Francisco Bay Area, Salt Lake City, Seattle, and San Diego. Because surface fault traces re-occur at the same location in nearly all instances, their location and characteristics can be discerned through a comprehensive geologic investigation. The movement at the ground surface is not always expressed along a single fault trace. Instead, the underlying fault movement is often expressed over a wide fault zone with secondary faults and distributed ground deformation. The resultant movement at the ground surface can damage infrastructure by breaking utilities, displacing bridge components, and inducing structural damage in buildings.

Surface faulting has interacted with several buildings during recent earthquakes (e.g., Bray 2001). The performance of buildings depends on site and project-specific factors including the fault characteristics (e.g., type, amount of offset, and its definition), the nature of the overlying soil (e.g., the soil thickness and ductility), and the foundation and structure systems (Bray 2009). For example, the Attaturk basketball court in Turkey was significantly damaged and judged to be unrepairable in the part of the building overlying a displaced fault trace, because its pile foundation locked the structure into each side of the fault (Anastasopoulos and Gazetas 2007a). In 1972 in Nicaragua, the 15-story Banco Central building was not damaged significantly because its thick basement walls, robust foundation, and weight caused the fault rupture to divert around the building (Niccum et al. 1976). A residential structure in the 1992 Landers earthquake fault zone suffered relatively less damage, because its mat foundation was isolated partially from the fault-induced ground strain through slippage along a plastic sheet that had been placed under the mat during construction (Murbach et al. 1999).

The prevailing strategy for mitigating the surface fault rupture hazard is to avoid building on or near active fault traces (Bryant 2010). However, in certain cases, this may be difficult to achieve, and sometimes when the amount of fault displacement is relatively minor, it may be unnecessary. Structures can be built safely on or near active faults when the hazard is well defined and manageable and the structure is designed appropriately (e.g., Cluff et al. 2003; Johansson and Konagai 2006; Gazetas et al. 2008; Bray 2009). In fact, several recent projects have been completed in active fault zones. A residential development in Southern California was designed utilizing numerical simulations to establish rational setback locations and mechanically stabilized soil in combination with post-tensioned mats to mitigate damage from anticipated bedrock fault rupture offsets of 3 cm (Bray 2001). California Memorial Stadium, which is situated on top of the Hayward Fault, was recently retrofitted using "fault-sliding blocks" to accommodate a design strike-slip fault movement on the order of 2 m (Vignos et al. 2009).

There are several more cases where geologists and engineers have worked together to identify and characterize surface faulting and to apply sound engineering principles in developing robust designs that mitigate the hazards associated with surface faulting. Surface fault rupture is a ground deformation hazard that can be mitigated geotechnically and structurally by employing design strategies that are routinely applied to address other ground deformation hazards, such as mining subsidence, landsliding, lateral spreading, and expansive soils. The objective of this paper is to investigate some of the most promising geotechnical mitigation strategies to develop insights that aid in the evaluation of the surface fault rupture hazard.

The characteristics of fault rupture through bedrock are controlled largely by the existing geologic structure, but the nature of the surficial earth materials and the built environment determine the surface expression of the bedrock fault at a particular location (e.g., Bray 2001, 2009). Bransby et al. (2008a,b) investigated the response of fault rupture propagation through soil using a series of geotechnical centrifuge experiments. In these studies, both normal and reverse fault rupture through sand of varying relative density and thickness were investigated. Importantly, the effects of mat foundations were also investigated by including steel plates and flexible loads in some of the experiments.

The surface fault rupture phenomenon has been modeled successfully through numerical simulations using several soil constitutive models. Bray et al. (1994b) employed the Duncan et al. (1980) hyperbolic model that incorporates stress–strain nonlinearity, stress dependency, and importantly, a well-defined failure strain. However, it does not include dilation or strain-softening. Anastasopoulos et al. (2007) and Loukidis et al. (2009) used Mohr–Coulomb models modified to include strain softening. Capturing the nonlinear stress-dependent response of soil is critical. It is also important to capture the soil's ductility through its failure strain (Bray et al. 1994b). Additionally, capturing localization requires the use of a soil constitutive model with strain-softening. A finite strain formulation provides improved performance for large fault offsets.

Recent studies have modeled directly the response of structures to fault rupture propagation through soil deposits. For example, using the same soil constitutive models that were employed in the free-field analyses, Anastasopoulos et al. (2008a) included structures by adding flat structural elements with a specified stiffness and surcharge pressure at the ground surface. Their simulations replicated reasonably well the results of the centrifuge tests conducted by Bransby et al. (2008a,b). These studies and previous studies have led to several recommendations regarding the design of structures near or on active faults. They include the use of non-arbitrary setbacks (Bray 2001), mechanically stabilized earth fills beneath structures (Bray et al. 1993), decoupling slip layers beneath foundation elements (Bray 2001), strong basement walls (Duncan and Lefebvre 1973), strong mat-type foundations (Bray 2001; Gazetas et al. 2008), building weight to divert or diffuse fault movement (Berrill 1983; Gazetas et al. 2008), and simply supported bridge spans (Gazetas et al. 2008). However, comprehensive investigations of the response of structures to surface fault rupture are limited, and additional work in this relatively novel field of study are required. Specifically, the effectiveness of geotechnical mitigation strategies has not yet been assessed comprehensively for realistic structures. This is the primary aim of this study.

5.2 Response of Structures to Surface Fault Rupture

The typical responses of structures to surface fault rupture when mitigation was not employed are analyzed using the three-story steel moment-frame building with a conventional 0.45 m-thick RC mat foundation. Representative results are presented in Figure 3. Yielding in the structure initiated typically through excessive bending in the second floor beams at the beam-column joints. Yielding then progressed upward through the structural frame to the roof. Axial yielding of the beams and columns, either in tension or compression, did not occur typically. Shear failure in the beams and columns did not occur. Yielding in bending in the conventional mat foundation developed; whereas shear or axial failure did not occur. Similar results were obtained for the six-story building with a conventional mat foundation.

The empirically based building damage evaluation procedure presented by Boscardin and Cording (1989) was employed to evaluate the consequences of the fault-induced ground movements. This procedure uses angular distortion minus building tilt (which they simply call "angular distortion" or "β") and lateral strain to estimate the level of damage to a structure. Fault-induced building damage was found to be caused largely by angular distortion rather than by lateral strain, because even a thin mat foundation tied the structure's columns together laterally. When isolated spread footings were used, the structure was found to be damaged significantly due to the combination of lateral strain and angular distortion after minor vertical fault movement (<0.1 m). In the case of the model supported by isolated spread footings, column yielding in bending occurred in addition to the development of yielding in the rest of the structure as occurred for the case a conventional RC mat foundation.

Three mitigation strategies were investigated to assess their effectiveness in limiting structural damage from dip-slip fault rupture: (1) diffusing the underlying fault rupture over a large area to limit angular distortion at the ground surface; (2) accommodate fault rupture through rigid-body movement of the structure; and (3) diverting the fault away from the structure. Specific design strategies that fall into each of these categories are discussed subsequently.

5.3 Diffusion of Fault Rupture

Ductile Engineered Fill

Ductile engineered fill placed on top of a bedrock fault is known to spread discrete fault slip over a broad zone as schematically shown in Figure 4a (e.g., Bray 2001). This fill response can be used to improve building performance relative to the unmitigated scenario by replacing stiff, previously sheared soil with ductile compacted earth fill. The earth fill must be sufficiently deep and ductile to spread out the underlying fault deformation sufficiently. The width of fault offset spreading is roughly proportional to the fill thickness. Therefore, a greater fill depth will produce improved structural performance. Ductile fill (i.e., fill with a large failure strain) is also required to prevent a distinct shear failure offset from reaching the ground surface and to spread the underlying bedrock fault offset across a wider zone at the ground surface. The use of a thick, ductile compacted earth fill does not prevent fault movement from being expressed at the ground surface; rather, it causes the ground to warp in distributed shear in response to the underlying fault movement as opposed to rupturing along a distinct shear surface.

As an example of the effectiveness of this mitigation strategy, the case with a relatively stiff, brittle 10 m-thick native soil deposit that has been ruptured previously during several past earthquakes was analyzed. In this case, yielding developed in the beams of the three-story steel frame structure with a 0.45 m-thick mat foundation, which was described previously, after only about 0.2 m of vertical bedrock fault movement. However, if the previously sheared soil were replaced by 10 m-thick ductile engineered fill with 6% axial failure strain, the fault-induced ground deformation was spread out sufficiently so that yielding of the structural beams did not occur until 0.6 m of vertical fault movement (Figure 4b). For the case where the 10 m-thick engineered earth fill was even more ductile (i.e., 10% failure strain), yielding did not occur until over 1.5 m of vertical fault movement (Figure 4b).

Bray et al. (1994a,b) demonstrated the dependence of the height of the propagation of the fault rupture into a soil deposit on the soil's failure strain (i.e., its ductility). In developing their relationship, they had examined primarily reverse faulting and had used the failure strain of the soil in triaxial compression as the index of soil ductility. An update to this relationship is developed herein. Figure 5a was derived using the UBCSAND constitutive model by varying the soil's failure strain through varying several model parameters to provide a range of results. The relationships developed for reverse and normal faults differ because their stress paths differ, and hence, the failure strain of the soil differs for these two cases (Oettle and Bray 2012). Thus, the results presented in Figure 5a rely on the UBCSAND estimation for the soil's failure strain in a particular mode of shear. Figure 5b was developed wherein the more generalized stress path-dependent failure strain is plotted on the horizontal axis. Thus, normal and reverse fault results converge which indicates that the soil's response to the base fault displacement is a function of the actual failure strain of the material for the resulting fault-induced stress path.

The angular distortion induced at the ground surface can also be reduced by increasing the thickness of the fill until the spreading sufficiently accommodates structural requirements. As a rule of thumb, fault movement at the surface can be spread over a horizontal zone approximately equal to 1 to 2 times the fill thickness. Thus, the required fill thickness is a function of the amount and type of fault movement and the ductility of the fill. The proposed numerical simulations can be utilized to evaluate an appropriate combination of these parameters to ensure satisfactory seismic performance of the structure.

5.4 Rigid-Body Movement

Thick Mat Foundation

A thick mat foundation can resist effectively the damaging effects of many types of ground movement (e.g., those due to expansive clay and liquefiable sand movements). Mat foundations improve structural performance by tying adjacent columns together, bridging gaps in soil support, and redistributing stresses beneath the mat.

Illustrative numerical analyses were performed to evaluate the effectiveness of thick mat foundations at mitigating the surface fault rupture hazard. In these analyses, the structure was placed at the center of the free-field outcrop of the fault. Mat thickness was varied between 0.2 m and 4.5 m. A complex fault zone was also analyzed with the fault displacement split between two faults separated by 10 m, because many fault zones are not comprised of a single idealized bedrock fault.

The results shown in Figure 6 indicate that for the structural system analyzed, thick mat foundations can reduce significantly damage to the superstructure. For very thick mats, the fault movement-induced structural demands are well below the beam's yield capacity, even for relatively large fault displacements of several meters. Failure in bending in the mat foundation only occurred for relatively thin mats (<0.8 m thick). Interpretation of the results using the Boscardin and Cording (1989) methodology is presented in Table 5-1. The results indicate that structures with thicker mat foundations primarily responded by tilting. Thick mat foundations were effective for both reverse and normal faults and for varying fault outcropping locations. They worked well for both hogging and sagging type deformation modes and in complex fault zones, as shown in Figure 7.

Thick mat foundations are a versatile design strategy for preventing damage from surface fault rupture. The performance of robust mat foundations can range from protecting life safety with relatively thin mats to preventing structural damage with very thick mats or with small fault movements. The structure may not be usable immediately after an earthquake due to excessive tilt. There are retrofit strategies to relevel tilted mat foundations, such as the use of grouting or controlled excavations, that have been used successfully for structures a few stories in height. The implementation of these retrofit strategies becomes more challenging for taller, heavier buildings.

Decoupling of Foundation and Soil

Foundations can be "decoupled" from the potentially damaging ground strain induced by fault movements by reducing the friction between the foundation and the underlying soil (Bray 2001). This could reduce structural damage from surface fault rupture by decreasing traction applied to the base of the foundation, as was observed for a strike-slip fault in Murbach et al. (1999). The decoupling layer beneath the building foundation acts as a "fuse" to limit the damaging effects of lateral ground strains. This mitigation strategy has been employed successfully to mitigate structural damage due to mining subsidence (e.g., Kratzsch 1983). Decoupling can be achieved by installing two low-friction geosynthetic layers, with bedding sand below and above it, beneath the foundation of the structure. For example, two HDPE geomembranes were installed within the middle of a compacted sand layer as part of the retrofit of the California Memorial Stadium (Vignos et al. 2009). This limits the maximum force and strain applied from the ground to the base of the foundation of the structure.

Several numerical analyses were conducted to analyze the response of the three-story building with and without a decoupling interface. The friction angle between the mat foundation and the underlying soil was assumed to be equal to the friction angle of the sand when no geosynthetics were used. The friction angle was assumed to be 11° (Koerner and Narejo 2005) when a geosynthetic decoupling interface was added. This analysis was performed for both reverse and normal faults and for several mat foundation thicknesses.

Representative results are presented in Figure 8. The geosynthetic interface decreased the fault movement-induced deformation in the superstructure; however, the effect was not significant enough to improve substantially building performance. Hence, it had only a minor effect on reducing the moments induced in the superstructure for the cases analyzed. These analyses indicate that a mat foundation does an adequate job of laterally tying a structure's columns together without the assistance of a decoupling interface. While placing geosynthetics

underneath a mat foundation in a fault zone may be prudent, especially if a component of strike-slip movement is expected, it does not seem to have a significant enough impact on the damage induced by pure dip-slip type fault deformation to serve as a substantial mitigation strategy for this particular case. If isolated spread footings were used, the decoupling layer would reduce the transmission of lateral ground strain to the structure.

5.5 Diversion of Fault Rupture

General

It is possible for an earthquake fault rupture to be diverted around a structure, as has been observed in several earthquakes (e.g., Niccum et al. 1976; Lettis et al. 2000b). Fault diversion strategies investigated herein include ground improvement beneath a structure, a diaphragm wall between a fault and structure, the addition of a basement, tying a building down with ground anchors, and installing a seismic gap between the fault and structure. The inherent weight of a structure is also known to divert fault rupture (Berrill 1983). This effect has been implicitly included in the scenarios analyzed herein.

A diversion strategy is useful when a structure is located on a single side of a bedrock fault or at the edge of a bedrock fault zone with sufficient soil or engineered fill overlying bedrock to divert the fault. It is necessary when relying on fault diversion to have a well-characterized fault zone to ensure that the fault can be adequately diverted from the structure. A more versatile design strategy is prudent in areas where the fault zone cannot be well characterized. A relatively small setback can often achieve similar performance to fault diversion, because fault diversion can only occur at the edge of a fault zone. However, in areas with constrained siting requirements, or for existing buildings, diversion strategies may be useful. The diversion strategy warrants caution, however, because the hanging wall of the bedrock fault often undergoes distributed shearing. As stated previously, often the underlying fault-induced movement does not just displace along a distinct fault but instead the primary fault offset is accompanied by significant warping of the hanging wall block. In these cases, diversion by deflecting the primary fault rupture, but not the associated ground warping of the hanging wall, may prove to be ineffective. Thus, the diversion strategy should be considered primarily for cases when the structure is situated on the footwall of a dip-slip fault (or with strike-slip faulting).

Gazetas et al. (2008) suggested that it may be appropriate to assume the worst case position of a structure relative to a fault. However, this may be unnecessarily conservative in cases where fault trenching clearly identifies the extent of a fault. A reasonable zone in which the fault can be expected to rupture can be established for these conditions. Combinations of mitigation strategies can be used with fault diversion strategies to provide higher levels of reliability.

Ground Improvement

Increasing the strength and stiffness of the soil beneath a structure could divert a fault rupture away from the building and limit damaging foundation deformation. With this approach, the structure and improved ground must be entirely on one side of the bedrock fault. If the

ground were improved directly on top of the fault, the fault would be forced to propagate through the improved ground, and no fault diversion would take place. Many ground improvement techniques can be used to increase the strength and stiffness of the soil including vibratory compaction, jet grouting, deep soil mixing, etc.

The effectiveness of ground improvement as a mitigation strategy is analyzed herein. An increase in the foundation soil relative density was modeled using UBCSAND by adjusting N1,60 which causes an appropriate scaling of strength and stiffness. Cement treating was modeled by replacing the foundation soil with a Mohr–Coulomb material with properties appropriate to cement treated sand (εaf = 0.2%, □□= 0.167, ϕ = 30°, c =490 kPa; e.g., from Namikawa and Mihira 2007). Ground improvement was applied over a 6 m-wide zone under the building on that side closest to the bedrock fault, as shown in Figure 9.

The results indicate that ground improvement can significantly improve building performance. Structural performance was improved from "moderate to severe damage" to "slight damage" (using the criteria of Boscardin and Cording 1989) when the soil's relative density was increased due to soil densification ground improvement technique applied over a 6 m-wide zone next to a reverse fault. Ground improvement through cement treatment in the 6 m-wide zone resulted in a "very slight damage" state being developed in the overlying structure.

Diaphragm Wall

Fault diversion can be achieved by installing a diaphragm wall between the bedrock fault and the structure. In the case of a normal fault, the diaphragm wall will act like an excavation support system where the fault can be thought of as "excavating" the adjacent soil. The diaphragm wall can be designed to support the structure and prevent the structure from being undermined by fault movement. In the case of a reverse fault, the diaphragm wall can "shield" the structure from the fault rupture propagation.

Several numerical analyses were performed for normal and reverse fault movements to evaluate the effectiveness of this mitigation strategy. A 1.2 m-thick RC diaphragm wall (Nikolinakou et al. 2011) was installed 2 m from the otherwise unmitigated three-story building with a 0.45 m-thick mat foundation. A tieback was installed at approximately 1.5 m below the ground surface for the normal fault case. Tiebacks were not used for the reverse fault because the wall was being loaded by the fault and the tiebacks would not be engaged. The analysis was performed for cases wherein the structure was located on the footwall and hanging wall side of the fault with the footwall scenario shown in Figure 10a. For reverse faults, the analysis was performed only for case where the structure was located on the footwall.

These analyses indicate that diaphragm walls can significantly reduce building damage. Results presented in Figure 10b show that the bending moments in the structure do not increase significantly when a diaphragm wall is installed. Without the diaphragm wall, the structure would have significantly yielded after only a moderate amount of vertical fault movement (<0.3 m). This strategy was effective for substantial normal fault movements. The robust diaphragm wall diverted the fault rupture from the structure and provided the required support. By varying the location and characteristics of the diaphragm wall, it was found that this mitigation strategy was generally more effective when the wall was closer to the structure and installed to greater depths.

Basement

As discussed previously, a strong basement can divert fault movement away from the structure. A basement can lower the foundation level below the expected fault propagation plane and cause the fault plane to intersect the basement perimeter walls rather than the bottom of the foundation. If the basement walls are sufficiently strong, the fault rupture can be diverted along the basement walls, reducing damage to the building. As suggested in Duncan and Lefebvre (1973), the passive soil pressure is the maximum pressure that soil can exert on a basement wall. A stiff basement can also increase the rigidity to the foundation similar to a thick mat foundation.

Several numerical analyses were performed to evaluate the performance of basements in active fault zones. The unmitigated three-story building with a 0.45 m-thick RC mat foundation shown in Figure 3 was modified by adding one level of RC basement walls. The interior columns of the building were assumed to extend to the foundation and the same beams used for the second floor were used for the ground floor. The structure was not modified otherwise. The results of these analyses indicate that a basement can be beneficial for mitigating the surface fault rupture hazard. The addition of a strong basement improved the structure's performance from the "moderate to severe damage" state to the "negligible damage" state as defined in Boscardin and Cording (1989).

Ground Anchors

Tying a structure down with stiff ground anchors can also cause the fault rupture to divert around a structure. This approach can be a viable option for structures located on the footwall of a reverse fault. As long as the bonded portion of the ground anchors are well below the expected fault rupture plane and sufficiently strong, the anchors will act to hold the building foundation at a constant elevation, causing the fault to be diverted around the structure.

Several analyses were performed to evaluate the effectiveness of using ground anchors as a mitigation strategy. In these examples, the ground anchors were extended to 1 m above the base of the model and had a bonded length of 4 m. The three-story unmitigated structure with a 0.45 m-thick RC mat foundation was used as the structural model. The ground anchors were placed at each column. The results shown in Figure 11 indicate that structural damage can be significantly reduced with ground anchors. This strategy was also effective for even at large fault movements. However, the installation of ground anchors can be deleterious to the performance of the structure if the location of the fault, or the edge of the fault zone, is mischaracterized. This is the case in the example shown in Figure 12. Poor performance will also occur if the ground anchors are shorter than necessary, as was observed in Anastasopoulos and Gazetas (2007a).

Robust, well-designed drilled shaft or pile foundations may also be designed in some cases to divert an underlying fault rupture around a building; however, because of the complexities of modeling pile foundations in a fault zone (e.g., three-dimensional effects), this case was not analyzed in this study. It is critical that the fault movement be properly characterized because if differential ground movement occurs within the drilled shaft or pile foundation, the shafts/piles will be essentially "locked" into the ground and the differential ground movement will be transferred into the superstructure with disastrous consequences. Bray and Kelson (2006) use the example of a tree that is ripped apart because it is rooted into the

ground on both sides of a strike-slip fault offset to illustrate the potentially adverse effects of locking a structure into the ground.

Seismic Gap

It may be difficult to use the fault diversion mitigation strategies described previously at rock sites. A strategy was therefore developed which should perform well at rock sites. By placing a "seismic gap" between a reverse fault and a structure, the anticipated reverse fault movement can be accommodated by allowing the fault-induced ground movement to displace into the seismic gap. The excavation support system employed during construction can be left in place with sufficient consideration of durability issues to provide a seismic gap between it and the embedded building. A compressible cover is required over the gap. The seismic gap could also be filled with very compressible material.

5.6 Conclusions

Surface fault rupture can be damaging to structures built on or near active faults. For the baseline structure examined in this study, which underwent dip-slip fault displacements without geotechnical mitigation, the fault-induced ground deformations typically produced yielding of the structure's beams, starting from the second floor toward the roof, in bending at the beam-column joints and failure in bending in relatively thin mat foundations (<0.8 m). For structures with RC mat foundations, this damage was predominately caused by angular distortion of the ground and not by lateral ground strain. For structures with spread footings, both angular distortion and lateral spreading significantly damaged the structures. Several geotechnical mitigation strategies were then examined in this study. These strategies are categorized as: (1) spreading fault displacement over a large area; (2) causing the structure to respond with rigid-body movement; and (3) diverting the fault rupture. The effectiveness of these strategies can vary from protecting life safety to preventing significant damage and can be effective for a range of dip-slip fault displacements.

Structural response was significantly improved when faulted soil was replaced by ductile compacted earth fill, because the fault movement was diffused over a wide zone in distributed shear. Earth fills must be sufficiently thick and ductile to prevent the underlying fault dislocation from developing at the ground surface again.

RC mat foundations mitigated effectively the surface fault rupture hazard. This strategy was effective for both reverse and normal faults for many site and structural conditions. Specifying a mat of at least minimal thickness may be prudent in areas where a fault zone is known to exist but is concealed or poorly defined and thus cannot be located with confidence. Thicker mat foundations provide superior performance and are recommended in areas where shallow active faults are known to exist. Mat foundations will also improve structural performance in combination with other mitigation strategies.

Several fault diversion strategies explored that proved effective at protecting structures from fault movement. These strategies are limited, however, to structures placed on one side of a bedrock fault, which should in most cases be the footwall side of a dip-slip fault. Thus these strategies are not as versatile as using a thick RC mat foundation or ductile compacted earth fills. The fault diversion mitigation strategies are also more tenuous than the other strategies because

mischaracterization of the fault zone could lead to poor system performance. It is therefore recommended that a mat foundation be used in conjunction with a fault diversion strategy, when possible, for additional resiliency.

Ground improvement beneath the structure proved to be an effective fault diversion strategy in some cases. This approach causes shear strains to concentrate in the adjacent unimproved ground. Diaphragm walls can be installed between faults and structures to shield ground deformation from the structure. Basements can be placed to deflect fault movement so it propagates along the side of strengthened basement walls. Similarly, seismic gaps can be placed on the fault side of a structure to accommodate fault movement. Finally, ground anchors can hold structures down on the footwall side of reverse faults when the ground anchors are bonded well below the expected fault rupture plane.

The development of effective geotechnical mitigation strategies of the surface fault rupture hazard demands an interdisciplinary approach that includes a comprehensive geologic characterization of the potential fault displacements including secondary faults, a thorough geotechnical investigation of site conditions and evaluation of foundation design strategies and foundation movements, and an appropriate structural design that ensures the structural system and its components will withstand the anticipated movements of the foundation. Additionally, the implementation of the proposed geotechnical mitigation strategies requires a rational legal and regulatory environment. The proposed geotechnical mitigation strategies provide rational means for addressing the hazards associated with surface fault rupture.

Table 5-1. Comparison of building performance for two mat foundation thicknesses (normal fault, 60° dip, 15 m-deep soil, 2.0 m of previous vertical fault movement, $N_{1,60}$=22, K_0=0.45, for the geometry in Fig. 3).

Fault Displacement	0.45 m-Thick Mat Foundation				1.8 m-Thick Mat Foundation			
	Angular Distortion	Tilt	β (Angular Distortion – Tilt)	Damage	Angular Distortion	Tilt	β (Angular Distortion – Tilt)	Damage
0.05 m	-0.0002	0.0021	0.0023	SD	0.0007	0.0024	0.0017	SD
0.1 m	0.0000	0.0042	0.0042	MTSD	0.0024	0.0048	0.0024	SD
0.2 m	0.0006	0.0089	0.0083	SVSD	0.0063	0.0092	0.0029	SD
0.3 m	0.0011	0.0140	0.0129	SVSD	0.0110	0.0140	0.0030	SD

Notes: 1. SD=Slight Damage, MTSD=Moderate to Severe Damage, SVSD=Severe to Very Severe Damage (from Boscardin and Cording 1989); 2. Boscardin and Cording (1989) use the value of β to estimate building damage; and 3. Induced-lateral strain was negligible for all instances.

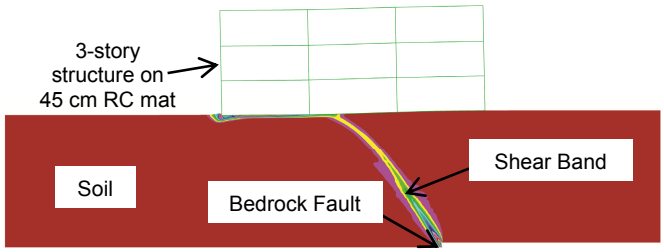

(a)

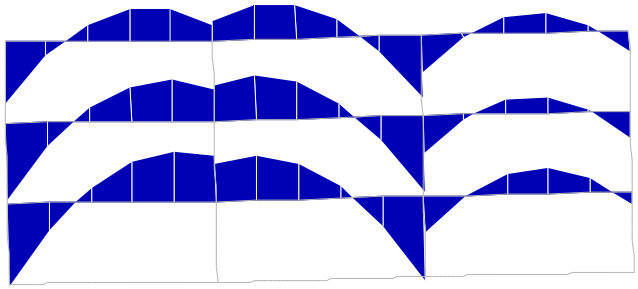

(b)

Figure 5-1. (a) Representative soil response due to underlying fault rupture (shear strain contours shown; 0.2 m x 0.2 m mesh size used); and (b) representative moments induced in the beams by fault rupture.

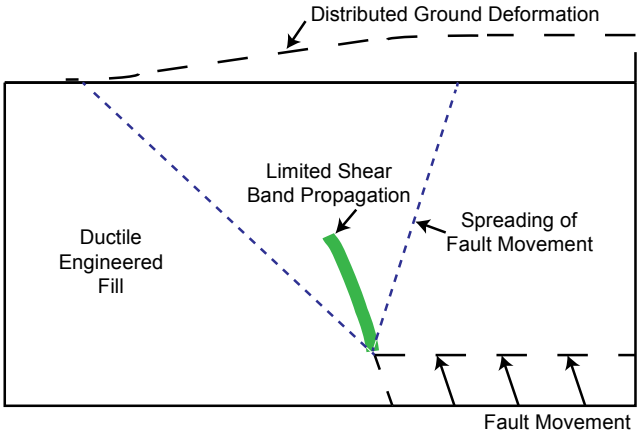

(a)

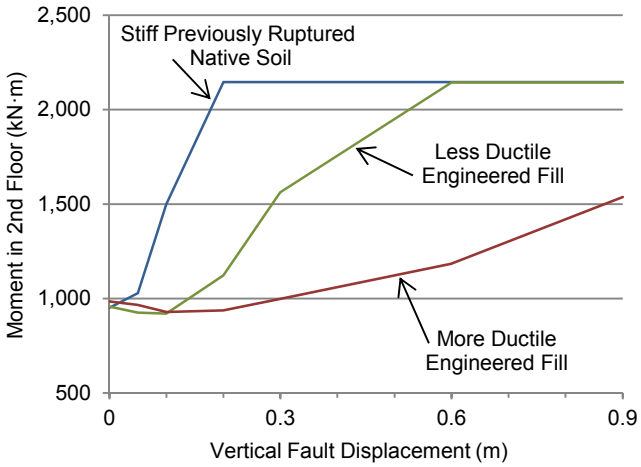

(b)

Figure 5-2. (a) Characteristic diffusion of fault rupture through engineered fill (not to scale); (b) response of native soil and two engineered fills (reverse fault, 45° dip, 10 m-thick soil deposit, 2.0 m of previous vertical fault movement, $N_{1,60}$=40, K_0=0.45, three-story structure, 0.45 m-thick mat, right edge of building 5 m left of the bedrock fault; plane-strain compression axial failure strains of 6% and 10% for less ductile and more ductile fills, respectively). Note: the second floor is defined as the beam above the ground floor.

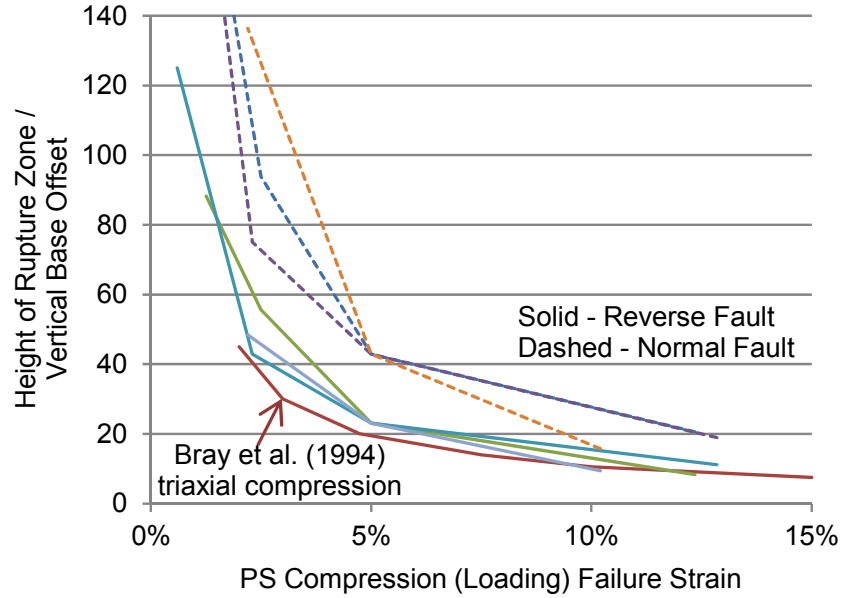

(a)

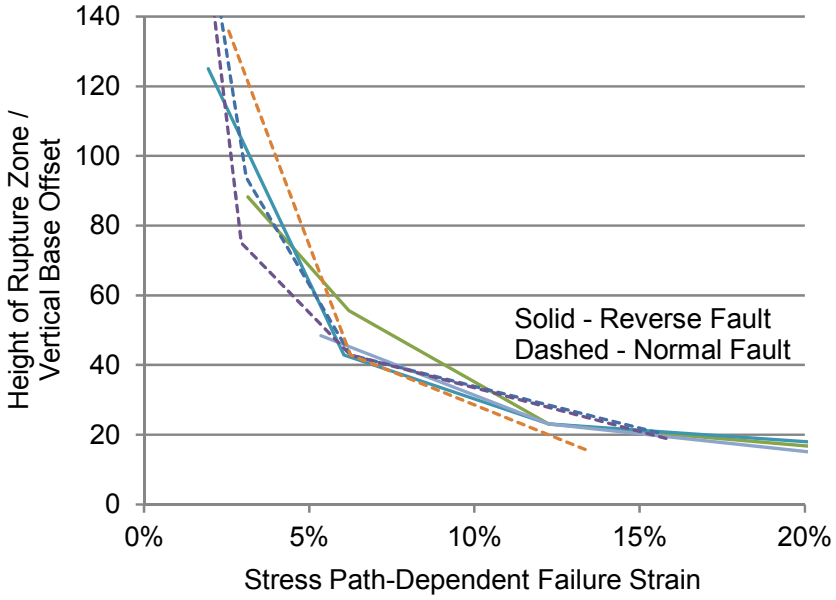

(b)

Figure 5-3. (a) Bedrock fault displacement required in previously unruptured soil for a shear band to reach the ground surface as a function of soil failure strain in plane-strain compression loading where the failure strain is varied by changing UBCSAND parameters $N_{1,60}$, R_f, and *hfac1*; and (b) in terms of the stress path-dependent failure strain (i.e., plane-strain compression unloading for a normal fault and plane-strain extension loading for a reverse fault).

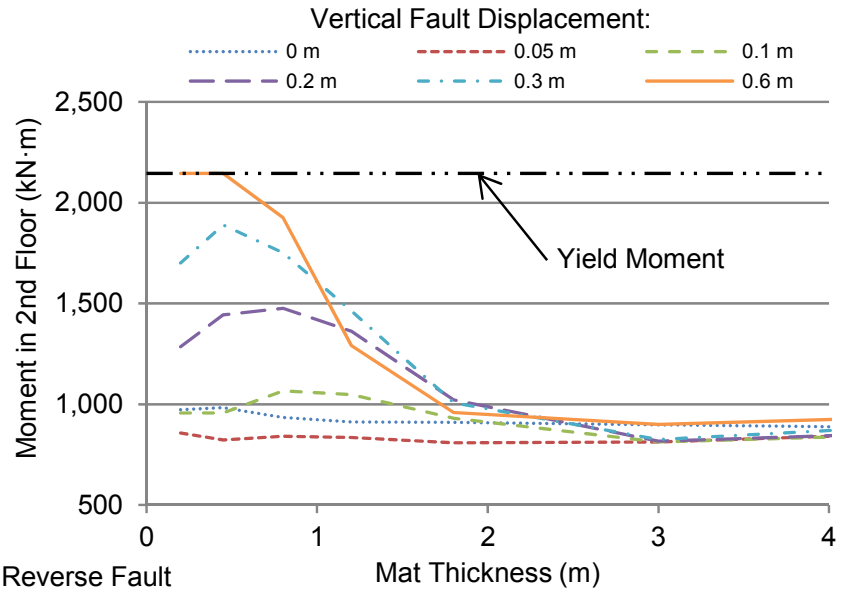

(a)

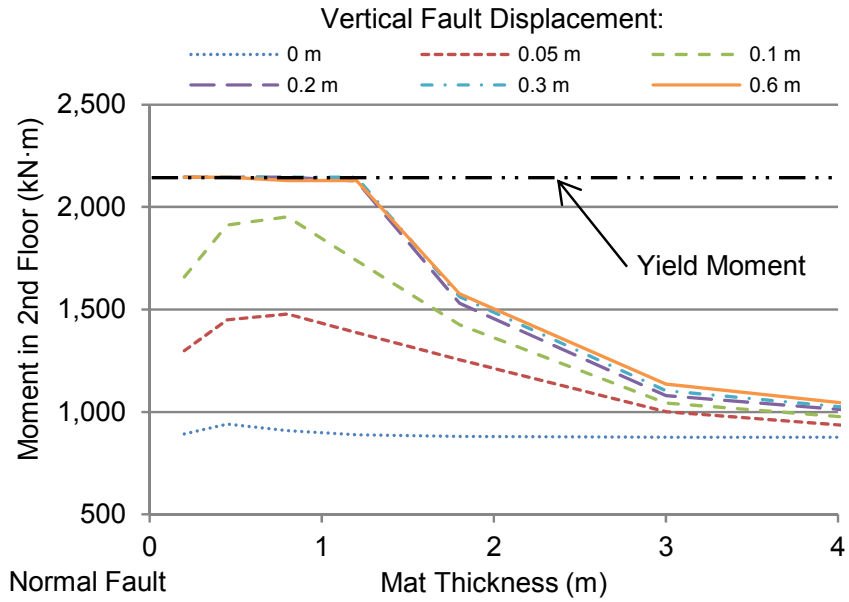

(b)

Figure 5-4. Comparison of building performance with mat foundations of varying thickness (60° dip, 15 m-thick soil deposit, 2.0 m of previous vertical fault movement, $N_{1,60}$=22, K_0 =0.45, for the geometry in Fig. 3): (a) reverse fault; and (b) normal fault.

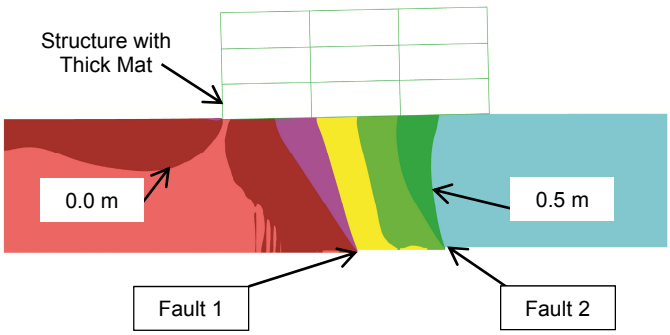

Figure 5-5. Complex fault ruptures can be mitigated by versatile mitigation strategies like thick mat foundations (shown) or engineered fill. For this analysis (60° dip, two faults 10 m apart, 15 m-thick soil deposit, 0.6 m of vertical fault movement, no previous fault movement, $N_{1,60}$=22, K_0=0.45), "very slight damage" was calculated for a 1.2 m-thick mat foundation and "moderate to severe damage" was calculated for a 0.45 m-thick mat foundation, according to the Boscardin and Cording (1989) method. Contours of vertical displacement are shown in 0.1 m increments.

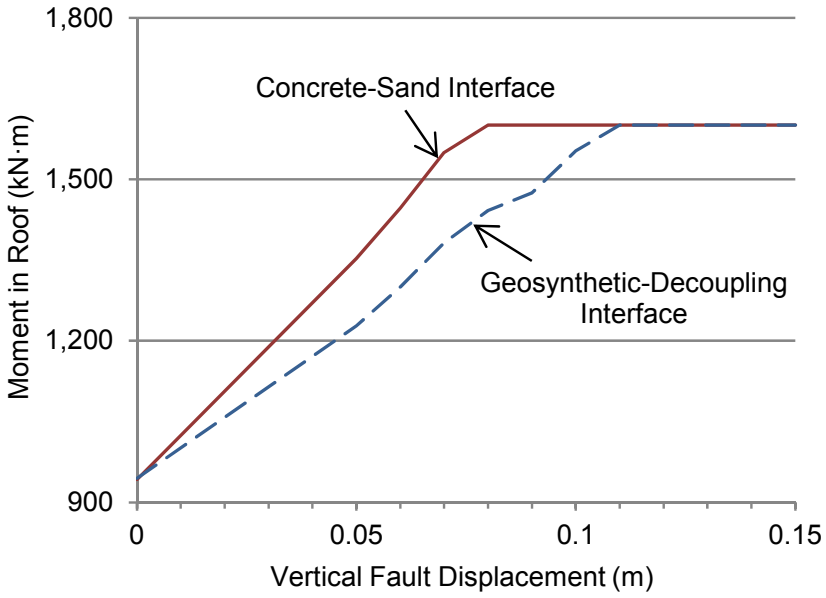

Figure 5-6. Comparison of building performance with and without a decoupling geosynthetic slip layer (normal fault, 30° dip, 15 m-thick soil deposit, no previous fault movement, $N_{1,60}$=22, K_0=0.45, 0.45 m-thick mat foundation, 11° interface friction compared to the full friction angle of the sand).

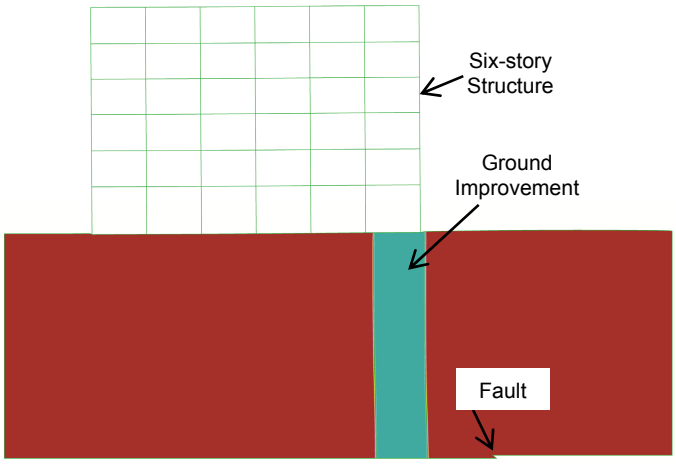

Figure 5-7. Ground improvement by densification of the soil beneath a structure results in estimated "slight damage" compared to "moderate to severe damage" according to the definitions in Boscardin and Cording (1989) for this representative situation (reverse fault, 60° dip, 25 m-thick soil deposit, 0.6 m of vertical fault movement, no previous fault movement, $N_{1,60}$=12 ($N_{1,60}$=36 in densified zone), K_0=0.45, 0.45 m-thick mat foundation).

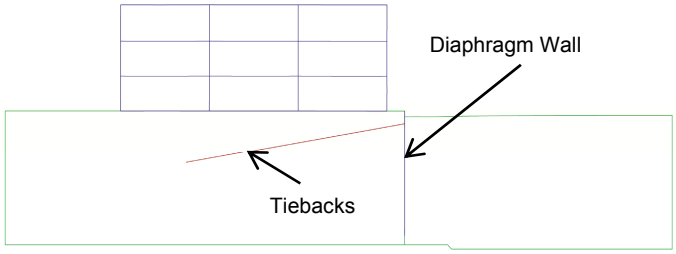

(a)

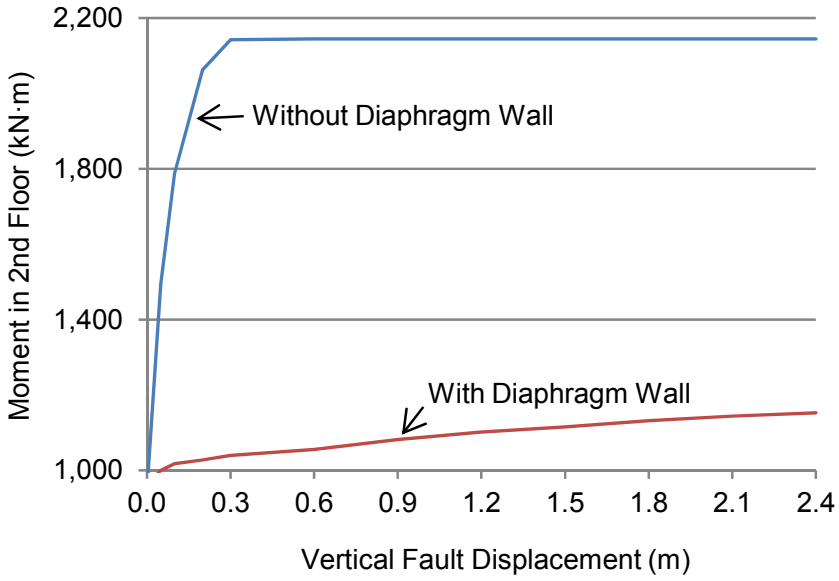

(b)

Figure 5-8. Comparison of building performance with and without a diaphragm wall on the footwall (normal fault, 60° dip, 15 m-thick soil deposit, 2.0 m of previous vertical fault movement, $N_{1,60}$=22, K_0=0.45, 0.45 m-thick mat foundation, 1.2 m-thick diaphragm wall, 1,500 kN anchor capacity, 800 kN pretensioning, 3.0 m anchor spacing): (a) model geometry; and (b) moment induced in the second floor of the building is significantly decreased with a diaphragm wall.

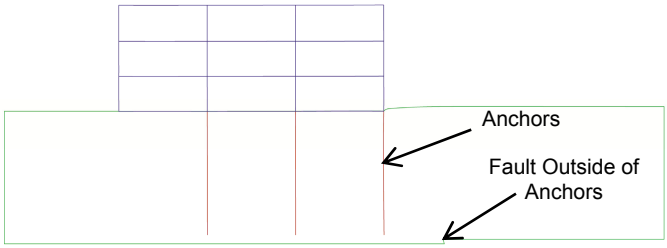

(a)

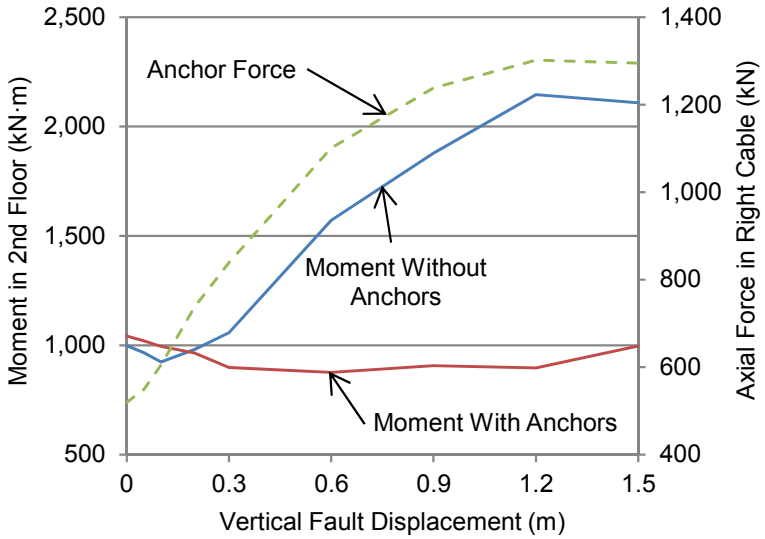

(b)

Figure 5-9. Comparison of building response with and without ground anchors (reverse fault, 60° dip, 15 m-thick soil deposit, 2.0 m of previous vertical fault movement, $N_{1,60}$=22, K_0=0.45, 0.45 m-thick mat foundation, 1,500 kN anchor capacity, 500 kN pretensioning, 5 m anchor spacing): (a) model geometry with anchors; and (b) moment in second floor is significantly decreased when anchors are in place; load in cable increases with increasing displacement.

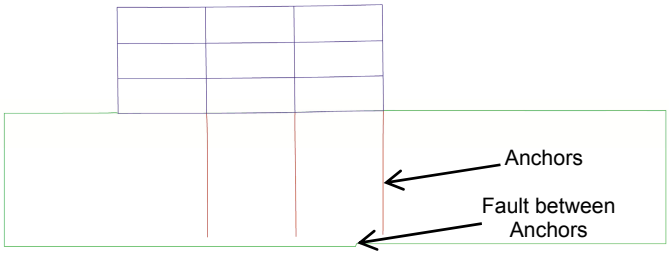

Figure 5-10. If fault zone is mischaracterized and a fault ruptures between two anchors, the building can be more significantly damaged with the anchors than it would be if no anchors were present.

CHAPTER 6: DYNAMIC EFFECTS

6.1 Introduction

To date, only pseudostatic analyses of earthquake fault rupture propagation through soil and its interaction with overlying structures have been performed. Specifically, bedrock fault displacement has been imposed without consideration of the rate of the applied fault displacement, and therefore ignoring dynamic effects. Yet, during an earthquake, permanent fault displacement occurs quite rapidly.

Previous studies indicate that the average velocity of the ground surface during fault displacement, which is commonly referred to as fling-step, is on the order of 0.5 to 1.0 m/s (e.g., Somerville et al. 1999; Abrahamson 2001; and Dreger et al. 2011). Thus, dynamic effects could be significant, and these effects should be investigated. Addressing the effects of a dynamically applied permanent fault offset will provide a more complete understanding of soil–structure interaction effects and the role that the rate of rupturing may play in building performance during a surface fault rupture event.

In this chapter, the effects of the rate at which a fault ruptures are investigated. The potential effects of the inertia of the soil and the overlying structure are considered. Rate effects on soil response are not be considered for the cases examined which all include dry sand. Furthermore, the transient portion of ground motion (i.e., due to vibratory shaking) is not included. Transient ground shaking will also occur coincident with permanent fault offset; however, the focus of these analyses is to calculate the expected permanent ground deformation taking into account dynamic soil–structure interaction rather than to calculate the total structural loads from a combination of fault offset and strong shaking. Structural loads from strong shaking could be added to the structural demands from permanent ground deformation using the approach described in Goel and Chopra (2009a,b). This work advances understanding by numerically evaluating the effects of fault rupture rate on fault rupture propagation through soil in the vicinity of structures for a variety of structural and soil conditions.

6.2 Previous Work

The effects of dynamic free-field fault rupture through soil were investigated with several geotechnical centrifuge tests conducted by Roth et al. (1981) and Scott (1983). For the dynamic centrifuge tests, a peak ground acceleration of approximately 0.5 g was applied. Transient ground shaking was not considered in these tests. Rather, they considered only the rate at which the fault rupture was applied. Both loose and dense sands were tested and compared to tests in which the base fault movement was applied pseudostatically. Unfortunately, the test setup required that the fault movement was applied on the footwall side of the reverse fault rather than the hanging wall side of the reverse fault as expected for the field case. A downward base displacement was applied to the footwall side of the reverse fault, because there was insufficient capacity to accelerate the hanging wall upwards with available laboratory equipment. This change from expected field behavior would not change the test results for pseudostatically applied fault motions; however, it does have the potential to affect the results of dynamically applied fault motion, as acknowledged by the researchers (Roth et al., 1981).

The findings of Roth et al. (1981), some of which are shown in Figure 6-1, indicated that pseudostatically applied fault displacement took additional base movement to develop fully the shear banding through the soil when compared to the case when the base movement was applied quickly. In the case shown in Figure 6-1, the shear band extends approximately to mid-height of the soil profile for the rapid base displacement case; whereas the shear band extended to the ground surface for the pseudostatic (slow) loading case. However, the deformed ground surfaces observed in the centrifuge tests for rapid and slow base displacement cases were qualitatively similar in most cases. Changes in the sand density produced larger differences in the observed ground surface deformation than changes in the base displacement rate. Soil properties play a more important role for modeling fault rupture propagation through previously unruptured soil.

Johansson and Konagai (2006) also performed physical testing of rapidly applied base fault movement without transient shaking; however, these tests were conducted to assess the effect of an undrained loading on saturated sands rather than evaluating the effects of fault slip velocity. Interpretation of these results for dynamic effects is complicated by the need to separate the inertial effects from the undrained soil response. Neither study addresses the interaction of dynamically applied fault rupture with overlying structures, which will be addressed in this chapter.

6.3 Numerical Procedures and Validation

The same numerical procedures documented in Chapter 3 were used herein with modifications for dynamic analysis, as described below. Properties used for these analyses are provided in Table 3-1. These analyses were conducted for a 60° dip fault, 15 m-thick soil deposit, 0.3 m of vertical fault movement, $N_{1,60}$=22, and K_0=0.45, unless otherwise noted. The soil is treated as engineered fill that has not been previously ruptured by past earthquakes, except for a single scenario in which the effects of prior ruptures was evaluated.

To perform dynamic analyses, damping is required to dissipate dynamic energy and prevent the model from continuously oscillating after application of the base rock fault rupture. Damping was largely accounted for in the soil constitutive model through hysteretic damping in the UBCSAND formulation. However, an additional 0.5% of Rayleigh damping was added to damp high-frequency motions. Because Rayleigh damping does not apply uniformly to all frequencies of vibration, the minimum Rayleigh damping value was applied at the small-strain site period of the soil profile (Itasca 2008). Damping within the structure was modeled using local damping (Itasca 2008) of 2% instead of Rayleigh damping to prevent a large decrease in the required time step.

The numerical model was configured initially to analyze the same fault and soil conditions reported in Roth et al. (1981) to compare results of the numerical simulations against relevant physical test results. However, these comparisons are qualitative at best, because the raw data of the Roth et al. (1981) tests are not available, and the relative density and other relevant soil properties of the centrifuge tests were not reported in Roth et al. (1981). Furthermore, the direction in which base fault displacement was applied in these laboratory tests was the opposite of that expected in the field. The results of the numerical simulations and the centrifuge tests were qualitatively similar, except the previously noted difference in the amount of base displacement required to fully develop the shear band through the soil deposit in the centrifuge tests was not observed in the numerical simulations. The overarching finding from these

numerical simulations and the geotechnical centrifuge tests described in Roth et al. (1981) is that there are only relatively minor differences in the patterns of the deformed ground surface for the dynamic and pseudostatic simulations and experiments.

Additional analyses were performed to evaluate the potential effects of the direction in which base rock displacement was applied in the Roth et al. (1981) geotechnical centrifuge tests. The UBCSAND numerical model used herein was applied for the Roth et al. (1981) test conditions for dynamic fault rupture applied to the footwall, as in the case of the centrifuge test, and applied to the hanging wall, as expected in the field. Several soil densities were simulated and compared to the available results from Roth et al. (1981) to address the issue of the unknown soil density. These results indicated that if the fault motion was applied as expected for the field condition, a slightly steeper fault dip angle was expected, although the effect was less than a one meter offset in the surface fault outcrop location.

6.4 Fault Ground Motions

There are very limited field data that describe ground motions within approximately 100 m of fault rupture (Dreger et al. 2011). A series of dynamic fault rupture simulations were conducted by Dreger et al. (2011) using a finite difference code with a supercomputer to study the ground motions expected in the very near fault region. These simulations were for an M_w 6.5 earthquake with an assumed average slip velocity (v_{ave}) of up to 1.0 m/s on the causative fault. Vibratory shaking was not included in this analysis, but the dynamic characteristics of the permanent ground offset were quantified. Fault offsets occurred in a ramp-like form in displacement. Velocity of the fault movement was a one-sided pulse. The rise time and characteristics of the calculated ground motion varied depending on the distance to the fault, rupture direction, depth of faulting, and differences in the assumed fault slip distribution. Dreger et al. (2011) recommended a simplified procedure for estimating the characteristics of the very near fault permanent offset. This simplified procedure consists of applying the expected fault displacement over a time window appropriate for the magnitude of the earthquake based on data in Somerville et al. (1999) in a form consistent with a Brune source model.

The estimates for fault displacement and rise time developed in Somerville et al. (1999) are based on seismic studies of at-depth fault rupture characteristics. Fault displacement and rise time were derived assuming self-scaling relationships, which assume constant slip velocity (i.e., the average relative velocity between the two sides of the fault when fling step is occurring). A similar model for very near fault ground motions was developed by Abrahamson (2001). The estimated average slip velocity in Somerville et al. (1999) was approximately 0.77 m/s, and the average slip velocity in Abrahamson (2001) was approximately 0.62 m/s. When a fixed slip velocity is assumed, the rise time can then be directly calculated for a given fault displacement.

Slip velocity can also vary considerably across a fault for a particular rupture event. A model of the variation in slip velocity across a fault was developed by Graves and Pitarka (2010) wherein slip velocity was assumed to be proportional to the square root of the local fault slip, with the average slip velocity over the whole fault estimated empirically (e.g., with Somerville et al. 1999). The variation in slip velocity may result in peak slip velocity across a fault as high as 5 m/s (at great depth), for at least one modeled scenario (Olsen et al. 2008). Slip velocity may also vary with depth. Rise time was increased by a factor of 2 in the top 5 km in the ground motion model of Graves and Pitarka (2010). This was based on observations of Kagawa et al. (2004) that

found that slip velocity was approximately 2 times greater for buried rupture events than surface rupture events. This corresponds to slower slip velocity in the top 5 km and faster slip velocity below 5 km, since most asperities for surface rupture events are found at depths less than 5 km, and asperities are predominately greater than 5 km deep for buried rupture events. Empirical observations of greater high-frequency ground motion from buried rupture events, resulting from higher stress drop, seem to confirm models of higher slip velocity for buried events since greater local fault displacement could correspond to higher slip velocity.

Abrahamson (2001) recommended assuming a full sine wave in acceleration for the shape of the fault rupture movement. In velocity, this is a one-sided velocity pulse, and in displacement, a smooth ramp function. This method has the advantage of slowly ramping up and ramping down fault velocity. The form of this ground motion in velocity, not considering the vibratory component of the ground motion, is (Abrahamson, 2001):

$$v(t) = v_{ave}\left[1 - \cos\left(2\pi \frac{t}{D/v_{ave}}\right)\right] \; for \; 0 \le t \le D/v_{ave} \tag{6.1}$$

where $v(t)$ is the slip velocity as a function of time (t); v_{ave} is the average slip velocity; and D is the permanent offset in the direction of interest.

Fault displacements within the range of 0.3 m and 1.0 m were imposed at the base of the model in this study. This range corresponds to the average surface fault displacement expected for earthquakes between M_w 6.5 to 7.0 (Wells and Coppersmith 1994). The assumed average slip velocity (or, conversely, rise time) is then varied to analyze the effect of slip velocity on the fault rupture process. Analyses are conducted for average slip velocities of v_{ave} = 0.4 to 1.0 m/s. The imposed velocity field of the displaced base rock block was assumed to follow Equation 6.1. The shape of the resulting ground motion qualitatively matches those simulated in Dreger et al. (2011). The ground motion of Dreger et al. (2011) is compared to the ground motion imposed to the base of the numerical simulations of this work in Figure 6-2.

Assuming a model with constant slip velocity causes the predicted acceleration from a fling-step motion to increase as the expected fault displacement is decreased. For example, using the average expected surface fault displacement for the given earthquake magnitude provided by Wells and Coppersmith (1994), a M_w 6 earthquake that ruptures the ground surface with 0.1 m of fault movement results in a peak acceleration in excess of 3 g for an assumed slip velocity of 0.7 m/s; whereas a peak acceleration of only 0.26 g is calculated for an M_w 7 event with 1.2 m of fault movement using the same assumed slip velocity. In these simulations, the slip velocity was limited to avoid producing unrealistically high peak ground accelerations. For example, the slip velocity did not exceed 1 m/s for the case with 0.3 m of fault displacement to limit the applied acceleration to no more than approximately 2 g.

6.5 Dynamic Boundary Conditions

Typical boundary conditions employed to analyze fault rupture propagation through soil are rigid displacement boundary conditions at the soil–rock interface and at lateral boundaries of the soil (e.g., Bray et al. 1994a,b). These were also the boundary conditions used in the Roth et al. (1981) centrifuge tests. Accordingly, this approach was used for a majority of the dynamic analyses conducted herein. However, using rigid displacement boundary conditions for a dynamic analysis presents additional difficulties compared to pseudostatic analysis. Free-field

soil movement during the fling-step phenomenon should be non-uniform with depth, i.e., there should be flexibility in the soil column that allows for the modal response of the soil deposit instead of a rigid response with depth. Additionally, reflected waves will be generated at a rigid lateral boundary condition, which is not representative of field conditions.

The typical method of addressing these issues for two-dimensional seismic site response and seismic soil–structure interaction analysis is to apply free-field boundary conditions at the lateral boundaries (Itasca 2008). Free-field boundary conditions apply stress at the lateral boundaries equal to that calculated from an analogous one-dimensional site-response analysis that is performed simultaneously. This boundary condition has the advantage of allowing boundary flexibility while accommodating reflected waves with viscous dashpots attached to the central part of the finite difference mesh.

Both of these boundary conditions are shown schematically in Figure 6-3. Preliminary analyses indicated that the details of the lateral boundary conditions would not significantly affect the results of the types of analyses conducted herein. This is likely a result of (a) not including the vibratory component of the ground motion; and (b) placing the lateral boundaries relatively far away from the structure and fault of interest. In some preliminary analyses, the free-field boundary conditions caused spurious permanent deformation at the lateral boundaries when high ground accelerations were applied. Therefore, the rigid displacement boundary conditions were predominately used in this study.

6.6 Fault Rupture without a Structure

A series of analyses were performed to evaluate the effects of assuming pseudostatic conditions for fault rupture propagation through a previously unfaulted soil deposit compared to performing a dynamic analysis wherein the base rock fault displacement was applied at its realistically rapid rate. In these analyses, a uniform 15 m-thick soil deposit was subjected to a 60° dip normal or reverse fault rupture with 0.3 m of vertical displacement. Pseudostatic and dynamic analyses were conducted for each fault type and compared. The results indicate that only minor differences in calculated ground deformation patterns exist for the pseudostatic and dynamic analyses for the free-field case. However, some minor to moderate differences in the calculated soil strain were observed occasionally.

Representative results are presented in Figure 6-4. For the reverse fault case, shear strain in the soil curved slightly to a shallower dip near the ground surface for the pseudostatic analysis but remained relatively straight for the dynamic analysis. Field observations indicate that reverse faults typically decrease in dip near the ground surface. At only 0.3 m of vertical base rock fault displacement, shear failure did not fully develop through the entire height of the soil profile as a result of assuming previously unruptured conditions. Simulations for larger fault displacements were performed for displacements large enough to cause complete shear failure (i.e., shear band formation) from the bedrock fault outcrop to the ground surface. This has a secondary effect of decreasing the applied ground motion acceleration as a result of assuming a constant slip velocity, as discussed previously. Numerical results for vertical fault displacements of 0.4 or 0.6 m with $N_{1,60}$=50 are presented in Figure 6-5. For these cases, the calculated soil shear strain decreases in dip closer to the ground surface, in agreement with observed field behavior. A numerical simulation was conducted for the same scenario, but with constant peak applied ground motion acceleration instead of constant velocity. The fault rupture propagation still

decreased in dip near the ground surface for this case. Therefore, it appears that curvature in fault propagation though soil requires sufficient bedrock fault displacement to generate a shear band throughout the soil profile, and thus, reach the point where kinematic effects (rather than stress effects) control the patterns of shear rupture propagation through the soil deposit (e.g., Bray et al. 1994b).

The inclination of the induced shear strain pattern was steeper for the dynamic analysis than for the pseudostatic analysis for the normal fault case. This was found to be the case for analyses at both 0.3 and 1.0 m of vertical fault displacement. For reverse faults and normal faults, the dynamic analyses calculated a somewhat broader zone of soil shear strain than the pseudostatic case. This resulted in multiple strands of rupture for the normal fault, but not for the reverse fault.

The level of stress in the soil deposit during fault rupture propagation varied significantly when dynamic forces were considered in the dynamic analyses. Time series of the normal vertical and horizontal stresses calculated in the middle of the soil deposit on the hanging wall side of the reverse fault are provided in Figure 6-6. For this case, both the horizontal stress and the vertical stress initially increased dramatically during the first quarter of the fault rupture-induced base motion. However, as the level of acceleration in the bedrock decreased, so did the horizontal and vertical soil stresses. As the bedrock acceleration switched directions, to slow the motion of the fault, horizontal and vertical soil stresses continued to decrease and developed tension for fault motions with peak vertical acceleration in excess of 1 g. After the bedrock fault motion ceased, the stress in the soil peaks at approximately 0.5 seconds as a result of the soil accelerating back downwards. The soil stresses oscillated until equilibrium was re-established.

With these significant changes in soil stress calculated in the dynamic analysis, stress-dependent behavior of the soil constitutive model was identified as being a potential source of differences between pseudostatic and dynamic free-field analyses. Dynamic fault rupture analyses were conducted employing a confining-stress independent model to investigate the influence of stress–dependent constitutive behavior. A Mohr-Coulomb model was selected with purely cohesive strength and no friction. The properties used were a mass density of 1.6 Mg/m^3, axial failure strain of 2%, Poisson ratio of 0.45, cohesion of 100 kPa, no tension failure allowed, and no dilation. The results of these analyses indicate that the Mohr–Coulomb model also predicts differences in the calculated ground deformation patterns from the pseudostatic and dynamic free-field fault rupture analyses. The calculated differences between pseudostatic and dynamic analyses were similar to those predicted when employing the stress-dependent UBCSAND model, which indicates that the change in fault rupture behavior was not solely a result of the soil's stress-dependent response.

6.7 Fault Rupture with a Structure

Baseline Analyses

The presence of a structure, with its mass and dynamic response, could potentially produce a more significant difference between the pseudostatic and dynamic fault rupture analyses than the free-field numerical simulations. Therefore, a series of numerical simulations were performed to evaluate the response of structures for the baseline soil deposit conditions (i.e., 15 m-thick deposit of dry, medium dense sand) for a range of plausible fault rupture

velocities. These simulations were conducted in four primary groups: (1) a structure placed predominately on the footwall side of a reverse fault; (2) a structure placed predominately on the hanging wall side of a reverse fault; (3) a structure placed predominately on the footwall side of a normal fault; and (4) a structure placed predominately on the hanging wall side of a normal fault. These test configurations and their corresponding results are shown in Figure 6-7 through Figure 6-11. Results from these analyses are plotted as the vertical movement of the edge of the foundation closest to the fault. This serves as a measure of the amount of fault diversion observed for a given analysis. Angular distortion is also used to estimate the effects of the analysis type on the estimated building damage. In addition to these cases analyzing fault diversion, two cases in which the structure was placed directly over a reverse or normal fault were analyzed.

The first group of simulations consisted of a three-story steel moment-frame structure placed on the footwall side of a reverse fault, as shown in Figure 6-7. The structure was placed such that the free-field outcrop of the fault was inside the footprint of the structure yet towards the edge of the structure to allow for the possibility of fault diversion (the free-field fault outcrop was approximately 5 m inside of the building edge). For the pseudostatic analysis, a moderate amount of fault diversion occurred, but the corner of the structure closest to the fault was still significantly lifted by the underlying reverse fault movement. However, for the dynamic analyses, as the slip velocity increased, the numerical model calculated increasing amounts of fault diversion. For example, at a rupture velocity of 1.0 m/s, the ratio of the movement of the edge of the foundation closest to the fault calculated for the dynamic case to the pseudostatic case was 0.06. In terms of the maximum angular distortion calculated for the structure, an angular distortion of 0.0043 was calculated for the pseudostatic case and 0.0016 for the 1.0 m/s case, as shown in Figure 6-7. This corresponds to “moderate to severe damage” and “slight damage”, respectively, per Boscardin and Cording (1989). This indicates that performing a dynamic analysis can affect the assessed damage state, although the effect is moderate.

The fact that the amount of fault diversion increased in this scenario is likely attributable, in part, to the inertia of the structure. At high slip velocity, the most efficient rupture path develops away from the structure to avoid imparting a large amount of kinetic energy to a structure that has significant mass. This is similar to fault diversion that was observed in the pseudostatic analysis as building weight increased, as shown previously. In the dynamic analysis, the inertia of the structure causes the effective building weight to increase as the dynamically imposed vertical stress increases, and therefore the amount of fault diversion increases. The results of the dynamic analyses indicate that it may be inappropriate to ignore the inertia of a heavy structure by performing a pseudostatic fault rupture analysis when attempting to estimate the magnitude of fault diversion and the actual rate of fault rupture is high (i.e., in the case analyzed, when the slip velocity exceeds 0.6 m/s, but this threshold will depend on several factors).

Another contributing factor could be the increased stress underneath the structure necessary to accelerate the structure to higher velocities. The increased soil stress could lead to increased soil strength as a result of friction and, therefore, cause the fault to avoid the zone of higher soil strength and partially divert around the structure. A cohesive Mohr–Coulomb model with no friction was employed in the same scenario for a slip velocity of 0.8 m/s to investigate the relative importance of stress-dependent constitutive model behavior. The results indicate that

fault diversion occurs even when a stress-independent model is employed. The amount of relative fault diversion calculated (i.e., movement of the structure calculated for the dynamic analysis relative to the pseudostatic analysis) was approximately 0.17 and 0.31 for two different sets of stress-independent material parameters compared to a ratio of 0.29 when using the UBCSAND model. Thus, this factor was likely not significant for the cases analyzed.

Differences between the results of the dynamic and pseudostatic analyses could also be attributed in part to differences already noted in the analyses of the free-field case. When combined with the effects of building weight observed in the pseudostatic analyses, the additional diversion of the shear rupture around the building in the dynamic analyses could have resulted from these two factors, i.e., the slightly different fault rupture pattern and additional translation of the emergence of the surface rupture outside of the building area. A series of simulations were performed of the same structural system with different building weights to investigate the effects of building weight further. The results from this series of tests are presented in Figure 6-8. They indicate that increased building weight causes increased fault diversion around a structure both for pseudostatically and dynamically applied fault rupture scenarios. At low building weight, there is an offset between the amount of fault diversion expected for pseudostatic and dynamic analysis, likely representing differences caused by changes in the free-field dynamic versus pseudostatic analyses. The change in fault diversion with increasing building weight, however, is greater for the dynamic case than the pseudostatic case by approximately 24% in the range of 25 to 55 kPa. This increase in the dependency of the amount of fault diversion as function of building weight could be attributable in part to the increased foundation contact stress for a dynamic analysis. However, it is difficult to conclusively determine that it is the inertia of the structure that increases fault diversion rather than the previously documented differences in free-field response interacting with pseudostatic fault diversion from building weight.

Considering the results of these and prior analyses of this scenario, it appears that dynamically applying the base rock fault displacement, especially at relatively high rupture velocities, could cause the shear rupture to divert more around the structure than when the fault displacement is applied pseudostatically, at least for this limited scenario. This effect increases slightly as the structure's weight increases, because the increased inertia of the structure which the dynamic analysis accounts for, but the pseudostatic analysis does not completely account for because it neglects dynamic effects.

A second group of analyses were conducted to analyze the effects of dynamic fault rupture on a structure predominately on the hanging-wall side of a reverse fault. The structure was placed close enough to the fault to be significantly affected by fault movement, thus having a strong potential for changes in expected fault diversion. The amount of fault diversion that occurs in this case does not seem to be sensitive to the slip velocity of the fault rupture, and therefore not sensitive to conducting a dynamic or pseudostatic analysis, as shown in Figure 6-9. In terms of angular distortion, 0.0070 was calculated for the pseudostatic loading case and 0.0060 for the v_{ave} = 0.8 m/s dynamic case, not indicating a significant effect from the rate of rupture. Likewise, the analysis of a normal fault on the footwall side of a fault (placed in the same location as in the first group of analyses) did not seem to induce a significant amount of fault diversion as a result of conducting a dynamic analysis, as shown in Figure 6-10. In terms of angular distortion, 0.0084 was calculated for the pseudostatic case and 0.0065 for v_{ave} = 0.8 m/s.

These two scenarios are fundamentally different from the case of a structure on the footwall side of a reverse fault. In these cases, soil is being pulled away from the edge of the structure closest to the fault. In the former case, soil is pushed into the corner of the building nearest the fault. In both cases, however, it may be that the position of the structure does not influence significantly the pattern of the shear rupture through the soil in either the dynamic or pseudostatic analysis, so the effects of the analytical method employed are insignificant.

In the fourth group of analyses, where a structure is placed on the hanging-wall side of a normal fault (i.e., placed in the same location as the second group of analyses), the results of the dynamic analyses are slightly influenced by the rate of rupturing at relatively high rupture velocities as shown in Figure 6-11, which shows a small trend of decreasing structural movement with increasing slip velocity. This results in a decrease in the amount of fault diversion because the opposite side of the structure is moving with the underlying hanging wall downward. This may occur because increasing the fault slip velocity decreases the effective stress beneath the foundation, therefore causing decreased fault diversion. However, the resulting ratio of dynamic to pseudostatic structural movement for this case was only 0.70 at v_{ave} = 1 m/s, as shown in Figure 6-11. The maximum angular distortion calculated was 0.0015 for the pseudostatic case and 0.0035 for the v_{ave} = 0.8 m/s dynamic case. Maximum angular distortion increased not only as a result of a decreased amount of fault diversion, but also due to an increase in graben formation as the slip velocity increased, as indicated by the corner of the foundation furthest from the fault increasing in downward displacement. Thus, as slip velocity increased, the left side of the building increased in elevation and the right side of the building decreased in elevation.

For the case of the structure being situated directly on top of a 60° dipping reverse or normal fault, as shown in Figure 6-12, there is little chance for the fault rupture to divert completely around the structure. Therefore, only angular distortion in the structure was used as a metric to quantify differences between the dynamic and pseudostatic analyses. For these cases, only a negligible difference between dynamic and pseudostatic analyses was observed even though a relatively high rupture velocity of 0.8 m/s was imposed in the dynamic analyses. For the reverse fault case, dynamic analysis resulted in angular distortion of 0.0063, while pseudostatic analysis resulted in 0.0068. For the normal fault, angular distortion was calculated as 0.0085 and 0.0079 for the dynamic and pseudostatic cases, respectively.

Sensitivity to Building Location

A number of alternative scenarios were analyzed to investigate whether the reverse fault footwall scenario was a special case. First, the baseline footwall reverse fault configuration was modified to include a representative six-story structure instead of the previously used three-story building. This scenario is shown in Figure 6-13. The six-story building is approximately 6 m closer to the fault than the three-story structure due to its increased width. Fault diversion on the same order of the baseline analysis was predicted by the numerical simulation for a slip velocity of 0.8 m/s. The ratio of fault diversion was approximately 0.36 (movement of the structure calculated for the dynamic analysis to the pseudostatic analysis) for the six-story structure compared to 0.29 for the three-story baseline scenario.

In another case, the three-story structure was again used but was shifted 3 m closer to the fault to assess the importance of structure–fault geometry on this analysis. In this scenario, the

ratio of fault diversion was approximately 0.56 compared to 0.29 for the baseline case, indicating less fault diversion. This scenario is shown in Figure 6-14. This indicates that the rate of fault rupture can affect structures on the footwall of a reverse fault, although the magnitude of the effect is not as great as for the case 3 m further from the fault, which was optimized to have a larger effect.

In a companion set of analyses, the structure in the baseline reverse fault hanging wall case, where a change in fault diversion was not noted, was moved 3 m to the right. The structural response in this scenario was also not sensitive to the rate of fault rupture with a recorded diversion ratio of 0.99 compared to 0.88 for the original building location. For angular distortion, 0.0051 and 0.0045 were calculated for the dynamic and pseudostatic cases, respectively. This indicates that the results for the reverse fault hanging wall case are not highly sensitive to building location. In another analysis, the structure was moved 3 m to the right of the building location in the baseline normal fault footwall case. The resulting fault diversion ratio was 0.80, compared to a fault diversion ratio of 0.90 for the baseline building location. This indicates an insignificant effect from building location.

Fully Developed Shear Rupture

Additional analyses were performed to examine cases where the shear rupture fully developed through the soil deposit and a clear surface rupture emerged. In one case, soil failure strain was decreased to cause soil failure without the need for additional fault displacement by increasing $N_{1,60}$ from 22 to 45. When the soil stiffness was increased, the amount of fault diversion in the dynamic analysis relative to the pseudostatic analysis decreased from 0.29 to 0.79, indicating only negligible fault diversion. These results are presented in Figure 6-15.

In another scenario, which is similar to the previously ruptured soil deposit cases analyzed in Section 4.3, 2.0 m of prior fault rupture was modeled to generate soil failure throughout the soil profile instead of decreasing the soil failure strain. An average slip velocity of 0.8 m/s was used to apply the prior 2.0 m of fault movement. The same slip velocity of 0.8 m/s was then used for the analysis of interest. Using the same slip velocity for each analysis results in different peak accelerations; however, it is consistent with the concept of a constant slip velocity model. The simulation was otherwise identical to the baseline reverse fault footwall scenario. The resulting foundation movement was 0.10 m for the dynamic case and 0.08 m for the pseudostatic case. These results indicate that increased fault diversion was not expected for a dynamic analysis when a prior fault rupture causing soil failure was modeled.

Analyses were also performed to analyze dynamic effects for larger magnitudes of fault displacement. Simulations were conducted for 1.0 m of vertical fault displacement for a reverse fault with the structure placed on the footwall of the fault. An average slip velocity of 0.8 m/s was used over the 1.0 m of vertical displacement. Otherwise, the scenario was identical to the baseline case. The resulting differences between dynamic and pseudostatic fault displacement were negligible (less than 10% difference in the amount of angular distortion and foundation movement). The resulting soil strain contour plots, shown in Figure 6-16, show only minor differences in the calculated soil strain between the pseudostatic and dynamic analyses.

The previous case, with 1.0 m of vertical fault displacement, was modified to increase the distance between the fault and the structure by 3 m. No other changes were made to the analysis. This case was developed to assess whether the results are sensitive to the location of the

structure. Angular distortion was calculated as 0.0049 for the 0.8 m/s case and 0.0054 for the pseudostatic case. Thus, the results for this building location do not appear to be sensitive to the rate of fault rupture.

However, because higher levels of displacement require lower peak acceleration given a constant slip velocity model, another simulation was performed in which the slip velocity was increased to maintain the same peak acceleration as for the 0.3-m vertical displacement simulation. The amount of fault diversion estimated in this case was still not increased relative to the pseudostatic case, indicating that the reason fault diversion did not increase was not a result of decreasing the applied ground motion acceleration as the amount of fault displacement was increased. Angular distortion was calculated as 0.0042 for this case, compared to 0.0049 for the case with a lower peak ground motion acceleration. Because all three cases in which the shear band was fully developed have not been significantly sensitive to the rate of fault rupture (the case of prior fault rupture, the case of decreased soil failure strain, and the case of increased vertical fault movement, even for higher slip velocity), it implies that the rate of fault rupture is not important when kinematic effects control the soil response, rather than when stress effects control soil response.

A pseudostatic analysis with twice the building weight was performed with 1 m of vertical fault displacement to assess whether the amount of fault diversion caused by increasing the building weight was similarly affected by the presence of shear band formation. The scenario was otherwise identical to the original pseudostatic 1 m fault displacement model with the structure shifted 3 m to the right. Increasing the building weight did significantly increase the amount of fault diversion and reduce angular distortion. The movement of the foundation edge closest to the fault was approximately 0.19 as a fraction of the baseline movement; likewise, the maximum angular distortion in the structure was decreased to 0.0014 from the value of 0.0054 for the original building weight. These results suggest that increasing building weight in a pseudostatic analysis can significantly affect building response, even when soil failure conditions are present.

Overall, these series of analyses indicate that in certain limited scenarios, in which soil failure conditions have not been developed previously, and a structure is situated on the footwall side of a reverse fault or the hanging wall side of a normal fault, performing a dynamic analysis can change to some extent the expected ground surface response to fault rupture and the calculated maximum angular distortion in the structure. However, for most scenarios, including scenarios in which the structure is placed directly on top of the fault, for cases with significant shear band formation, or for cases with lower ground motion intensity, the effect of performing a dynamic analysis rather than a pseudostatic analysis has a relatively minor effect on the expected foundation movement and structural damage.

6.8 Conclusions

Dynamic effects in soil–structure–fault interaction have typically not been accounted for in most physical or numerical research on this subject. Yet, most surface fault rupture occurs fairly rapidly. A numerical model was employed to assess the potential effects of fault rupture dynamics on the analysis of ground surface deformation of soil deposits overlying bedrock faults. Characteristics of potential fault ground motions were drawn from limited experimental and numerical studies on very near fault ground motions. Appropriate boundary conditions for

dynamic analyses of surface fault rupture were determined. A very limited experimental dataset of dynamically applied fault ground motion and soil–structure–fault interaction were used to validate parts of the numerical approach used herein.

The available experimental work and the numerical results presented herein appear to indicate that the dynamics of surface fault rupture have only a minor to moderate effect on fault-induced free-field ground surface deformation. Minor effects from high slip velocity include a slightly modified fault propagation path through the unruptured soil, especially for normal faults, and a somewhat broader zone of soil strain. However, the overall effect of fault dynamics on ground surface deformation, in the free-field, is minor compared to other parameters such as soil properties and fault characteristics.

A series of analyses were conducted to compare the expected performance of structures in the vicinity of a fault zone using pseudostatic and dynamic fault rupture analyses. For a structure placed on the footwall of a reverse fault, the amount of fault diversion increased moderately. The corresponding maximum angular distortion decreased and a moderately lower level of structural damage was expected. For a structure placed on the hanging wall of a normal fault, the amount of fault diversion decreased slightly and a graben structure developed more distinctly. The modified ground deformation response caused the calculated angular distortion to increase. However, for structures placed either on the footwall of a normal fault or the hanging wall of a reverse fault, a significant trend in the amount of fault diversion with the rate of fault rupture was not observed nor was there a significant change in the calculated angular distortion.

A number of other scenarios were developed to assess whether the results for cases with somewhat significant fault diversion were a special case or more broadly applicable. When the structure was moved several meters or when a different representative structure was used, a similar level of fault diversion was still expected; however, it often had a smaller effect than in the baseline scenario, which was often optimized for maximizing changes to the amount of fault diversion. For dense sand, pre-ruptured conditions, and larger amounts of fault displacement, only negligible differences between dynamic and pseudostatic fault rupture analysis were observed. In each of these scenarios, failure conditions had been developed throughout the soil profile. This suggests that dynamic fault rupture effects are not significant enough to change the kinematic constraints of the problem, which develop when failure conditions are met. Prior to the development of kinematic effects, the stress controlled problem appears to be influenced by the rate of fault rupture. This is in contrast to increasing the actual weight of the structure, which affects fault diversion even for higher levels of displacement.

Overall, the impact of considering dynamic fault rupture on the calculation of permanent ground deformation beneath a structure and the expected structural damage state is a secondary effect for most scenarios. It can, however, be a moderate to significant effect for certain soil and structure conditions when a rapid fling-step fault-induced displacement is expected and when the geometry is optimized to promote dynamic-induced fault diversion. However, because rapid fling-step is necessary to expect a significant change in the amount of fault-induced ground surface deformation, relying on high slip velocity to provide a beneficial effect on structural performance is inadvisable, especially with the limited research and field data available for very near fault ground motions. The case of a normal fault with a structure on the hanging wall side of the fault did noticeably increase the expected angular distortion of the structure when a dynamic fault rupture analysis was performed instead of the conventional pseudostatic analysis. Thus,

there are cases, when ignoring dynamic fault rupture effects can be unconservative. However, the differences between dynamic and pseudostatic analyses for most cases are relatively minor. Therefore, for the most part, dynamic fault rupture effects can be ignored when evaluating structural damage as a result of fault-induced ground deformation.

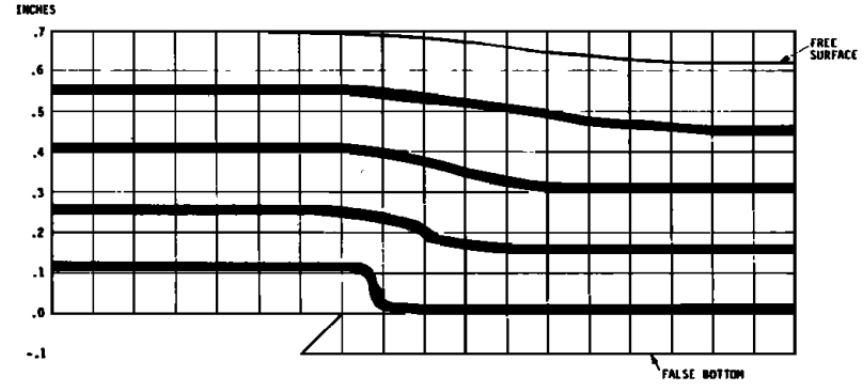

(a)

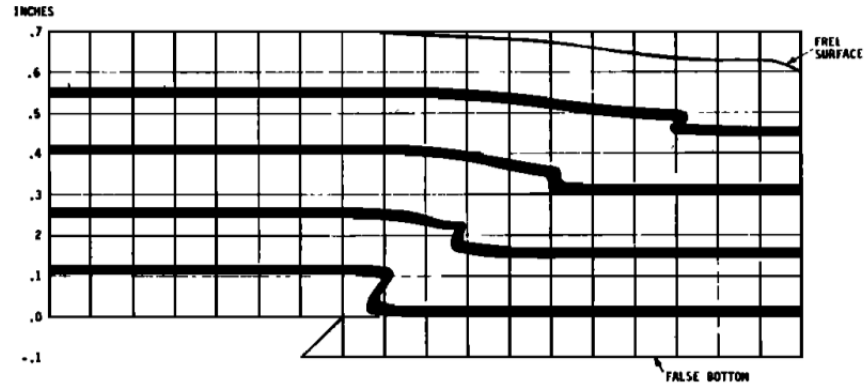

(b)

Figure 6-1. Centrifuge test results for dense sand from Roth et al. (1981) and Scott (1983): (a) fast fault movement; and (b) slow fault movement. For these tests the footwall was lowered rather than the hanging wall moved upwards. Slow fault movement resulted in more extensive shear band propagation and slightly shallower fault propagation dip compared to faster fault slip.

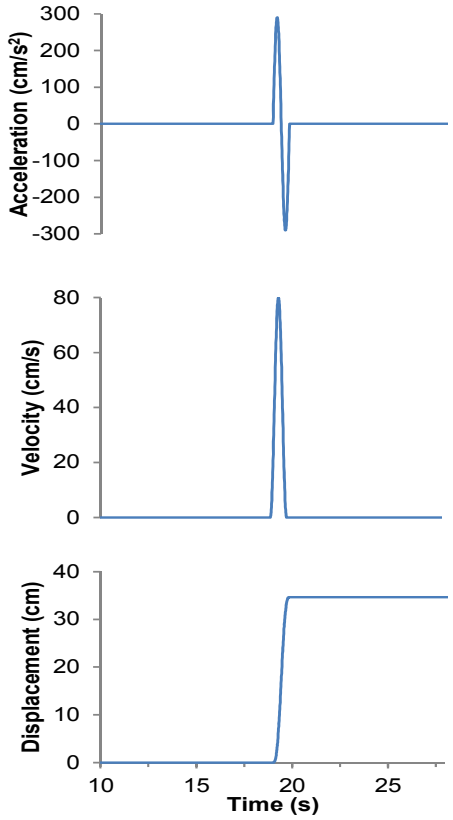

(a)

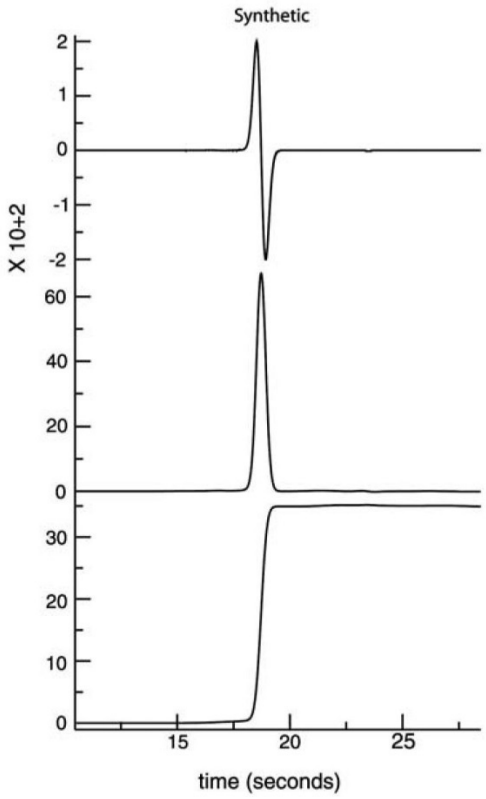

(b)

Figure 6-2. Comparison of fling-type ground motions (acceleration, velocity, displacement) in the direction of fault movement, without vibratory shaking: (a) sinusoidal pulse ground motions used in this study (for 0.4 m/s average slip velocity); (b) horizontal ground motions calculated in Dreger et al. (2011) for an M_w 6.5 strike-slip fault. Units shown here are centimeters and seconds. Note: 0.3 m of vertical displacement is the equivalent of approximately 0.35 m of along strike displacement (for a 60° dip fault), which is plotted here.

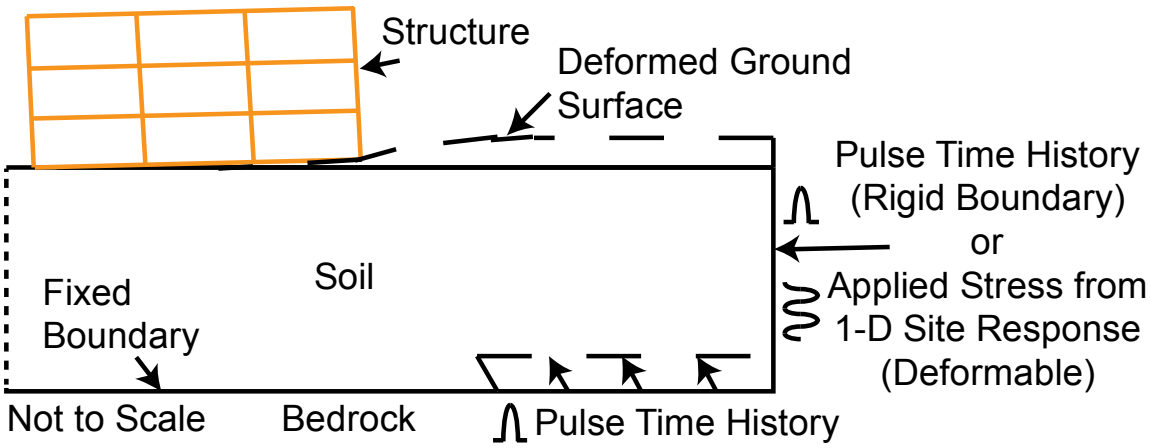

Figure 6-3. A schematic of the boundary conditions used in the analyses performed in this work. Note that the schematic is not to scale and the boundaries are placed further away from the fault in the actual analysis.

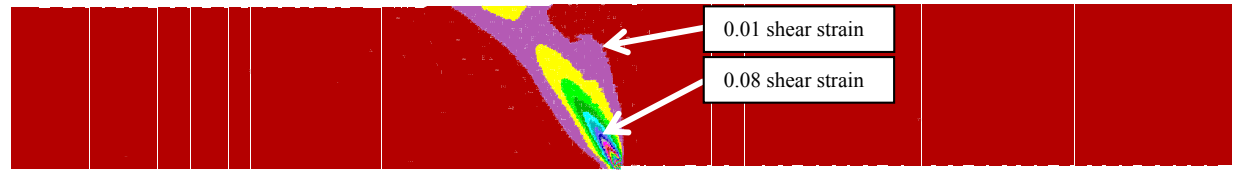

(a)

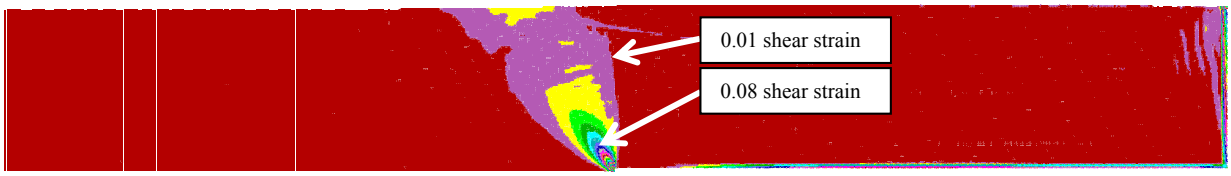

(b)

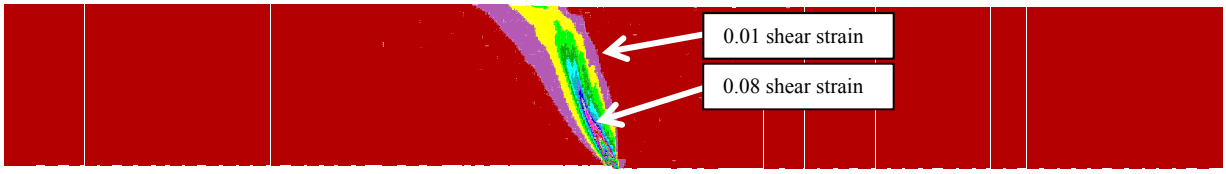

(c)

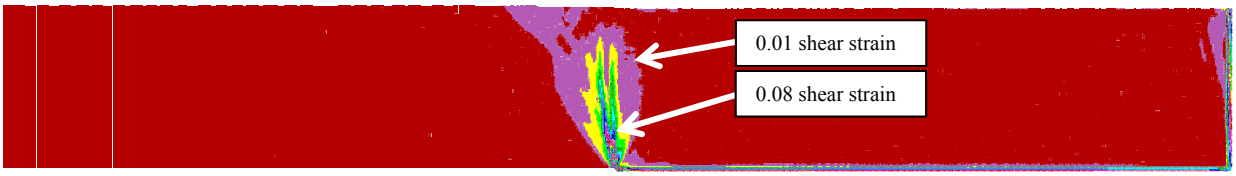

(d)

Figure 6-4. Differences between calculated ground surface deformation for dynamic (v_{ave} = 0.8 m/s) and pseudostatic analysis for free-field cases of reverse and normal faults with medium dense sand ($N_{1,60}$=22, 0.3 m of vertical fault movement) where shear bands do not reach the ground surface. (a) Pseudo-static, reverse fault; (b) dynamic, reverse fault; (c) pseudo-static, normal fault; and (d) dynamic, normal fault. Shear strains are plotted with an increment of 0.01 shear strain.

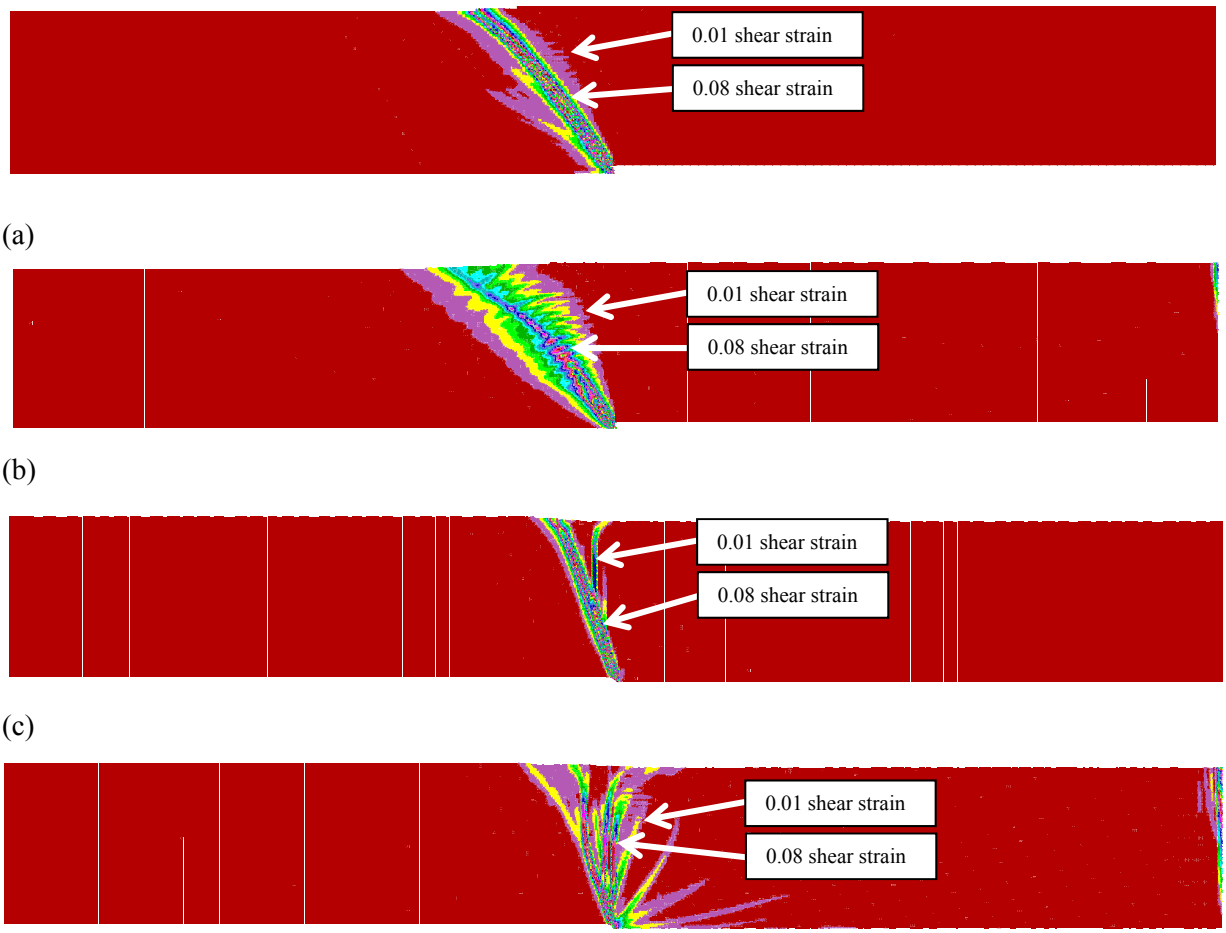

Figure 6-5. Differences between calculated ground surface deformation for dynamic (v_{ave} = 0.8 m/s) and pseudostatic analysis for free-field cases of reverse and normal faults with dense sand ($N_{1,60}$=50, 0.4 m of vertical fault movement for the normal fault and 0.6 m of vertical fault movement for the reverse fault) where the shear bands do reach the ground surface. (a) Pseudo-static, reverse fault; (b) dynamic, reverse fault; (c) pseudo-static, normal fault; and (d) dynamic, normal fault. Shear strains are plotted with an increment of 0.01 shear strain.

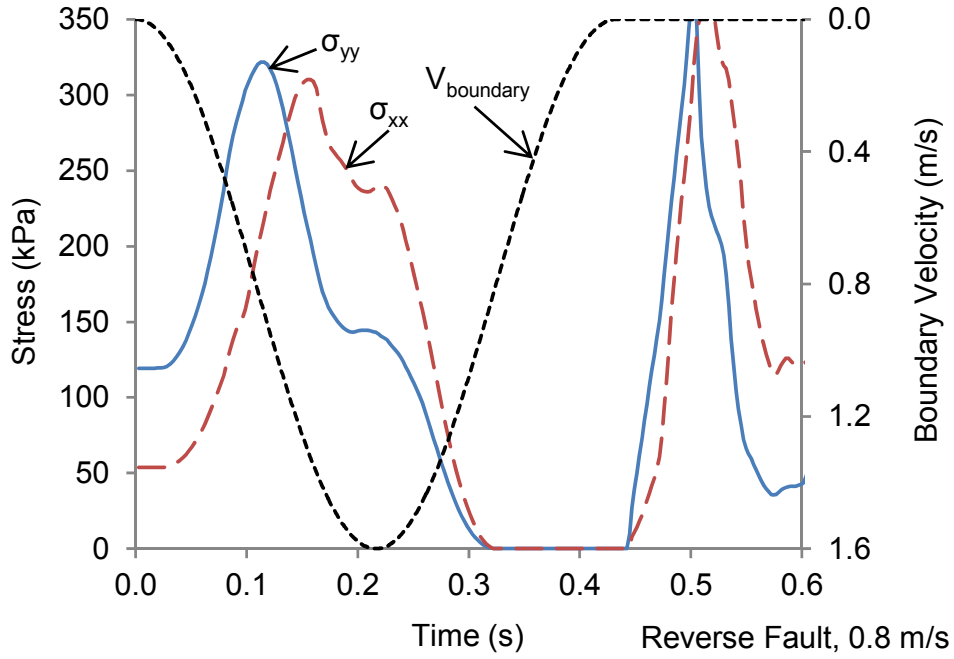

Figure 6-6. Stress change in the free-field as a result of reverse fault movement with an average slip velocity of 0.8 m/s applied as a sinusoidal pulse. The spike in stress at approximately 0.5 s is a result of the soil falling back downwards after having been accelerated upwards. Stress changes are shown for the hanging-wall side of the fault, 40 m away from the bedrock fault, 8 m above bedrock.

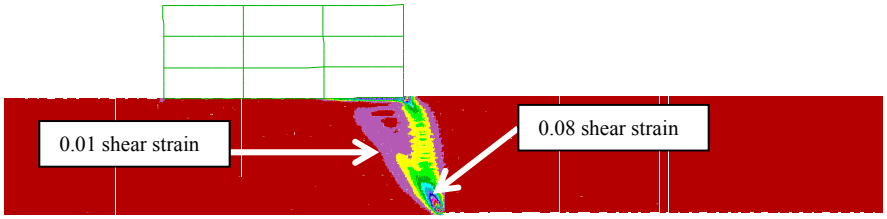
0.01 shear strain
0.08 shear strain

(a)

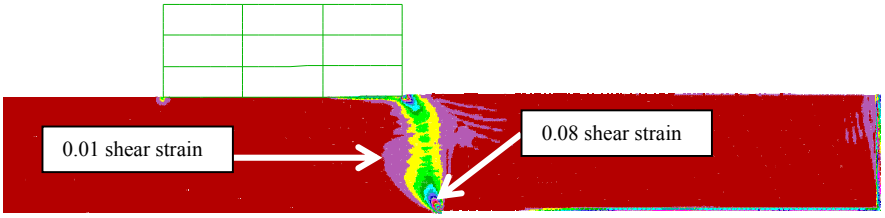
0.01 shear strain
0.08 shear strain

(b)

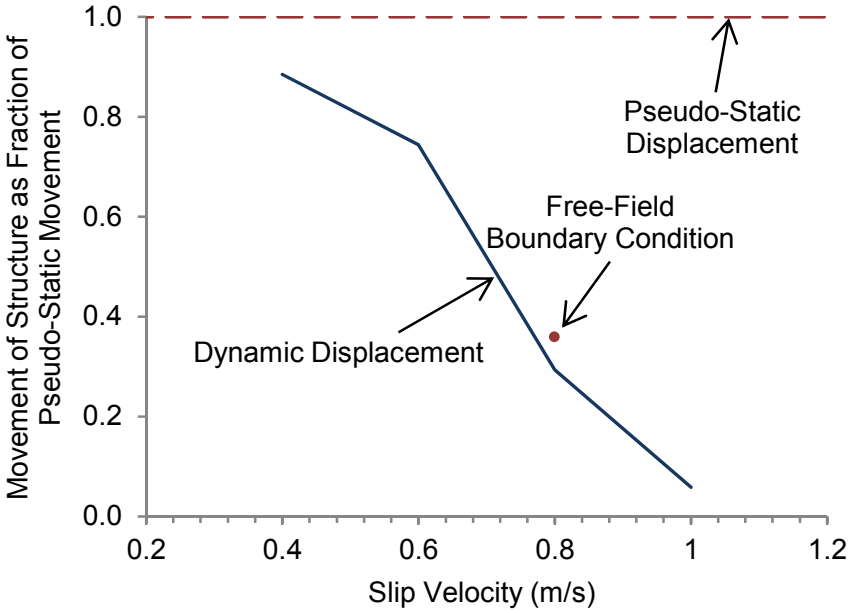
Movement of Structure as Fraction of Pseudo-Static Movement
1.0
0.8
0.6
0.4
0.2
0.0
0.2
0.4
0.6
0.8
1
1.2
Slip Velocity (m/s)
Pseudo-Static Displacement
Free-Field Boundary Condition
Dynamic Displacement

(c)

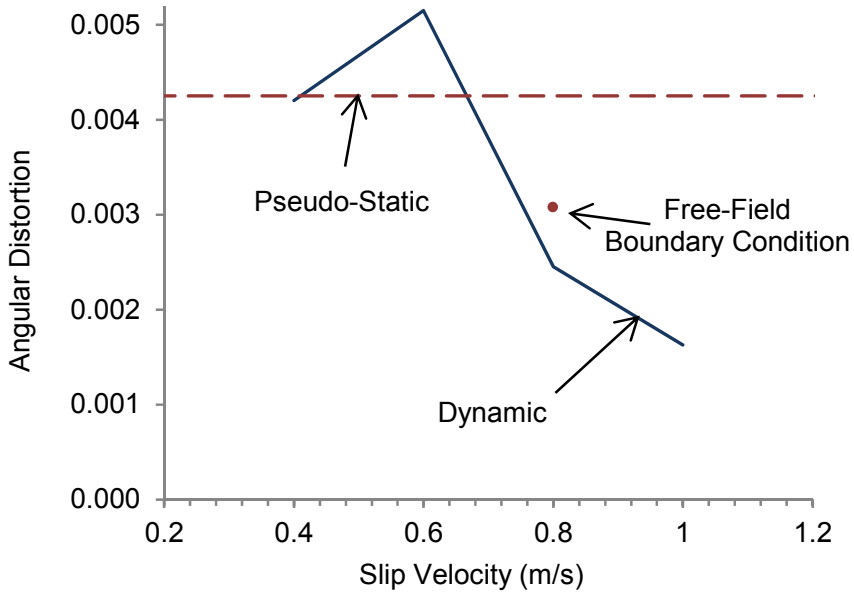

(d)

Figure 6-7. Comparison of structural response for a range of slip velocities for a building on the footwall of a reverse fault. (a) Calculated shear strain contours for the pseudostatic case; (b) calculated shear strain contours for the 0.8 m/s average slip velocity case; (c) structural movement as a function of slip velocity; and (d) maximum angular distortion of the structure as a function of slip velocity. Shear strain is plotted in contours of 0.01 shear strain. Note: movement of the structure is the vertical displacement of the foundation edge closest to the fault, which serves as an index of fault diversion.

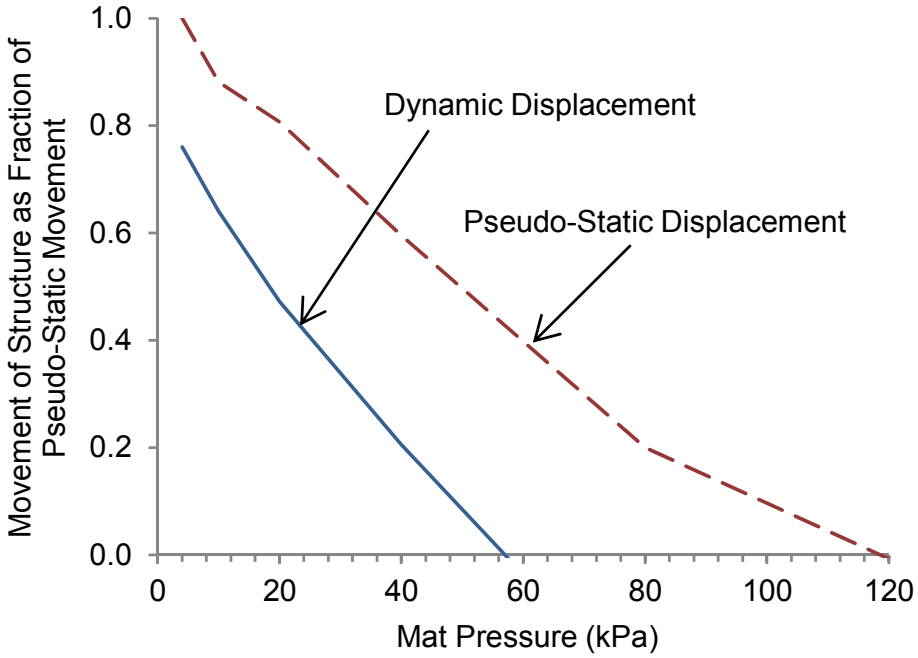

Figure 6-8. Comparison between pseudostatic and dynamic analyses (v_{ave} = 0.8 m/s) for a range of structural weights. Note: movement of the structure is the vertical displacement of the foundation edge closest to the fault, which serves as an index of fault diversion. Here, it is normalized to the pseudostatic case in which the structure has a weight that causes an average mat contact pressure of 4 kPa.

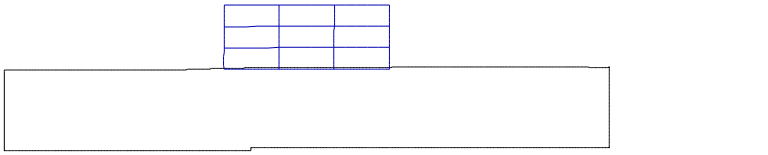

(a)

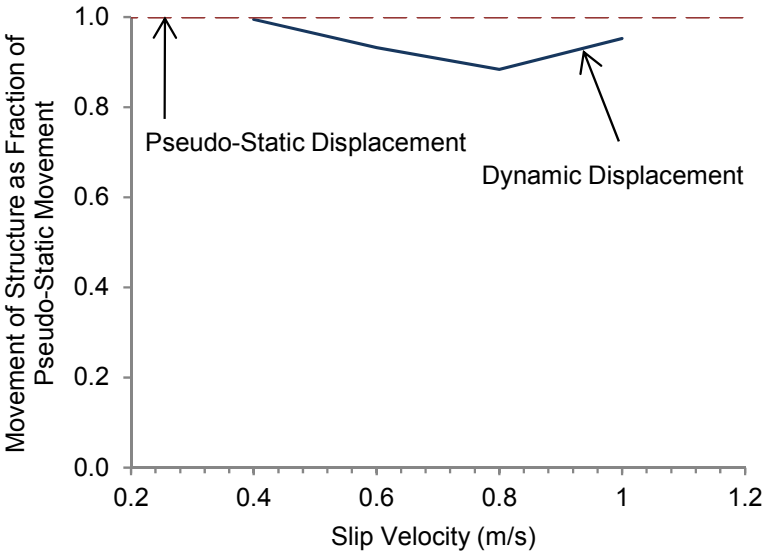

(b)

Figure 6-9. Comparison of structural response for a range of slip velocities for a building on the hanging wall of a reverse fault: (a) schematic for this analysis; (b) structural movement as a function of slip velocity. Note: movement of the structure is the vertical displacement of the foundation edge closest to the fault, which serves as an index of fault diversion.

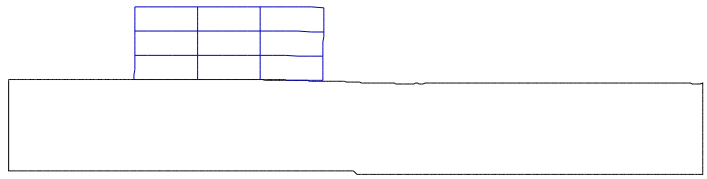

(a)

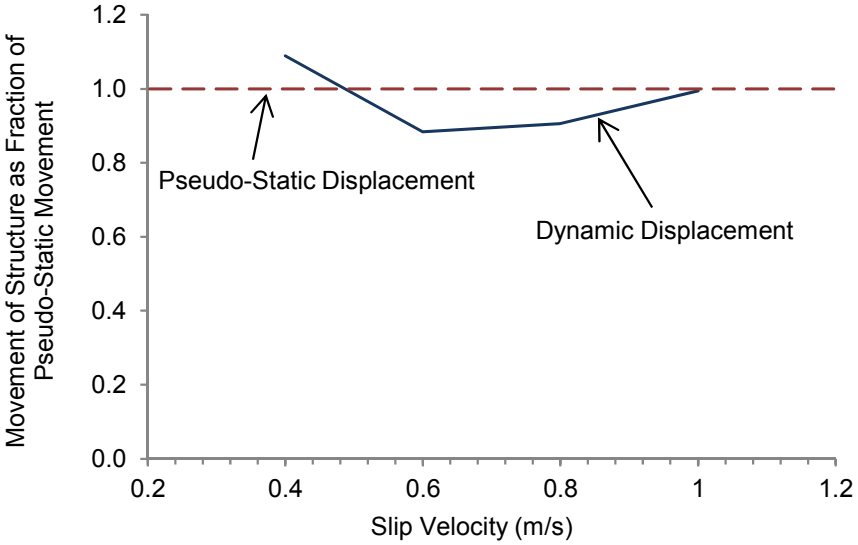

(b)

Figure 6-10. Comparison of structural response for a range of slip velocities for a building on the footwall of a normal fault: (a) schematic for this analysis; (b) structural movement as a function of slip velocity. Note: movement of the structure is the vertical displacement of the foundation edge closest to the fault, which serves as an index of fault diversion.

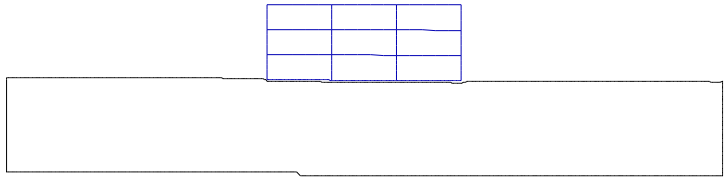

(a)

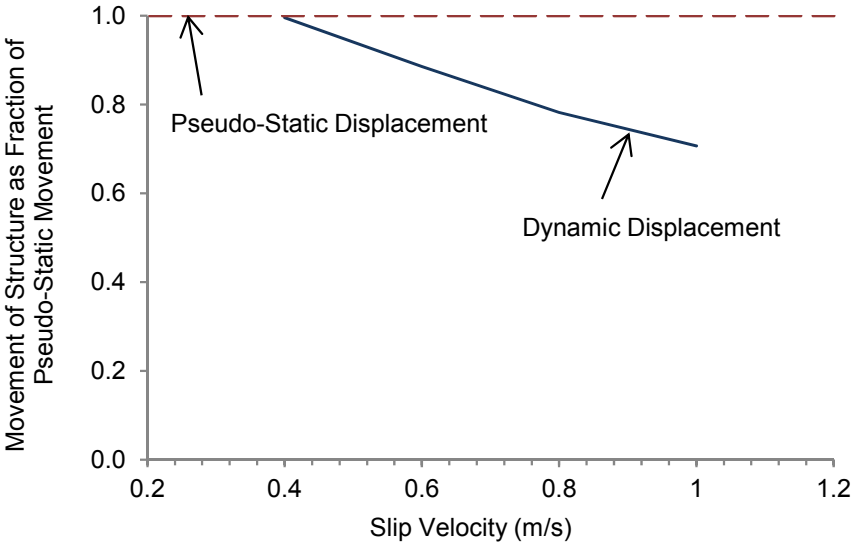

(b)

Figure 6-11. Comparison of structural response for a range of slip velocities for a building on the hanging wall of a normal fault: (a) schematic for this analysis; (b) structural movement as a function of slip velocity. Note: movement of the structure is the vertical displacement of the foundation edge closest to the fault, which serves as an index of fault diversion.

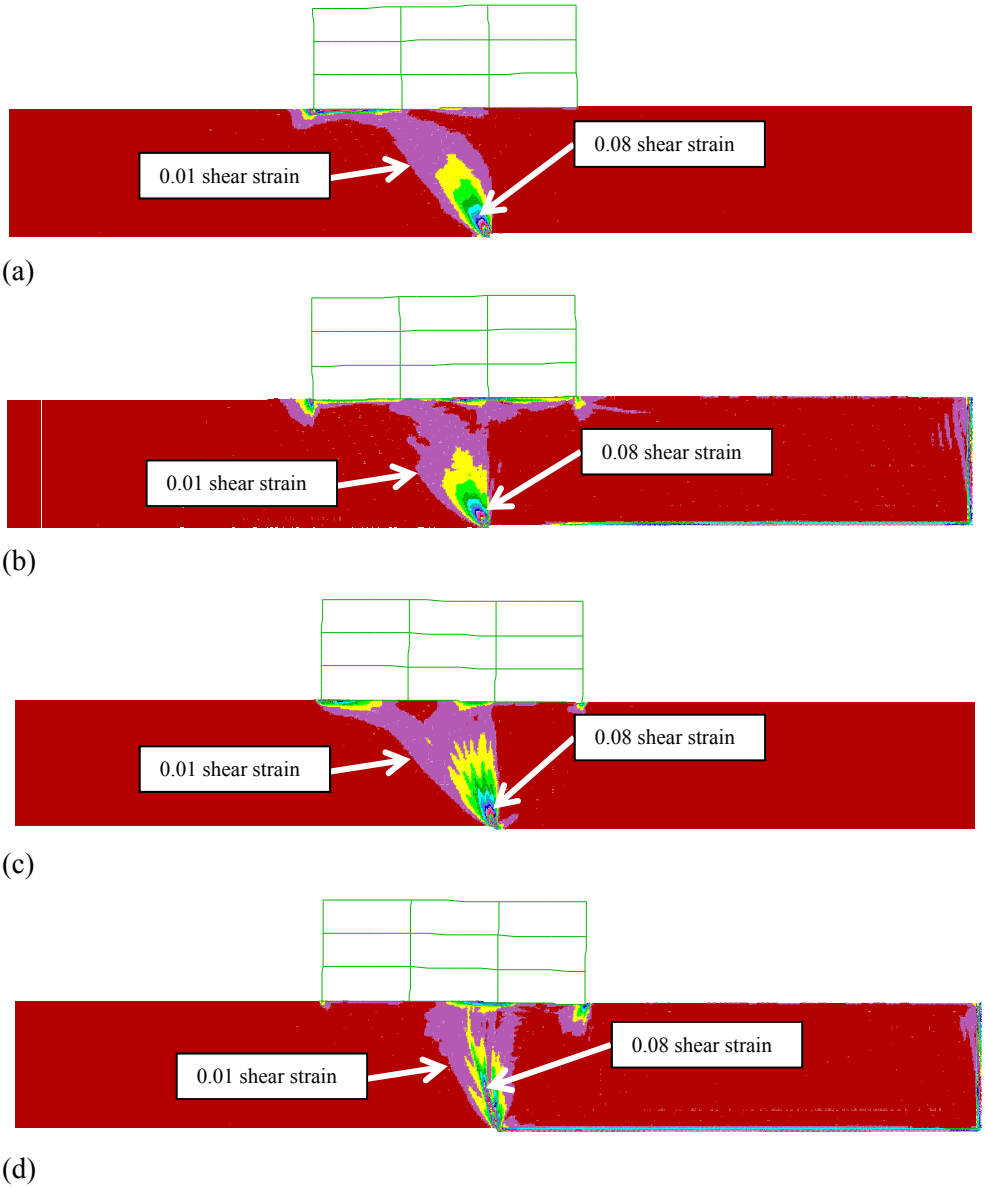

Figure 6-12. Comparison of structural response for a structure placed over the center of a fault: (a) reverse fault, pseudostatic analysis; (b) reverse fault, dynamic analysis (v_{ave} = 0.8 m/s); (c) normal fault, pseudostatic analysis; and (d) normal fault, dynamic analysis (v_{ave} = 0.8 m/s). Shear strain is plotted in contours of 0.01 shear strain.

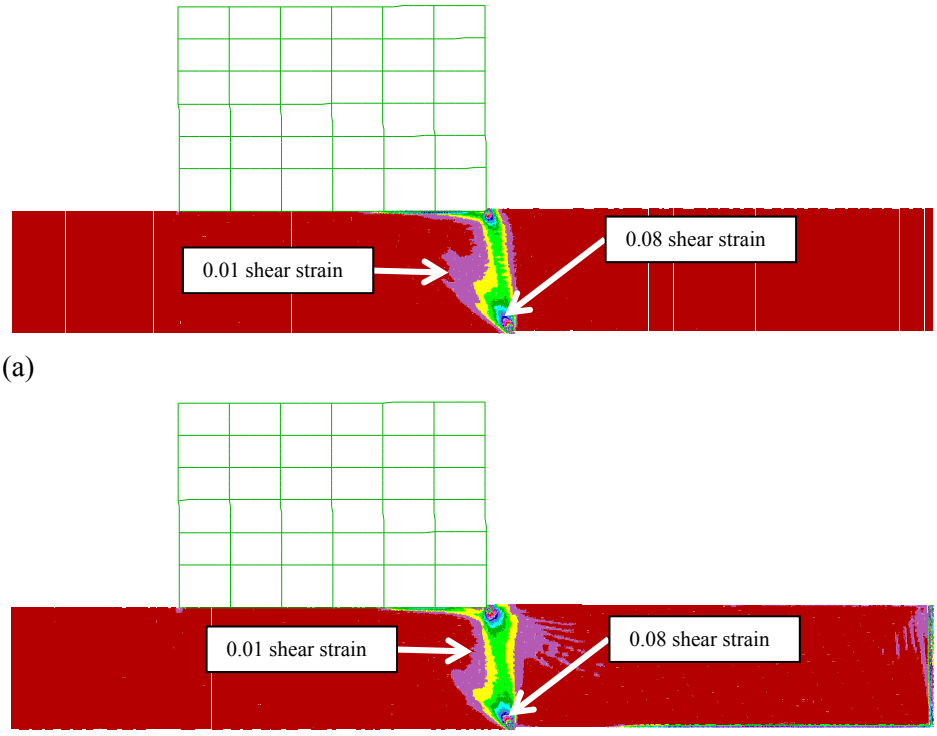

Figure 6-13. Comparison of structural response for a six-story structure near a reverse fault: (a) pseudostatic analysis; and (b) dynamic analysis (v_{ave} = 0.8 m/s). Shear strain is plotted in contours of 0.01 shear strain.

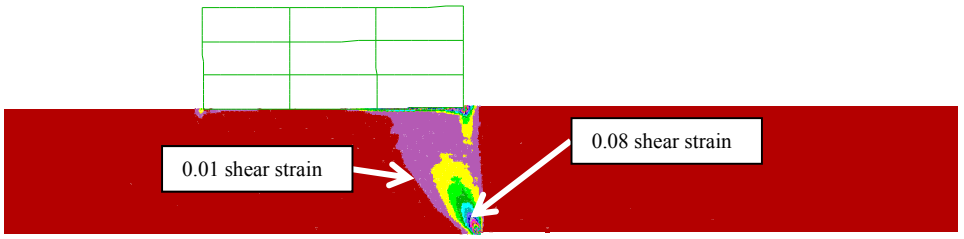

(a)

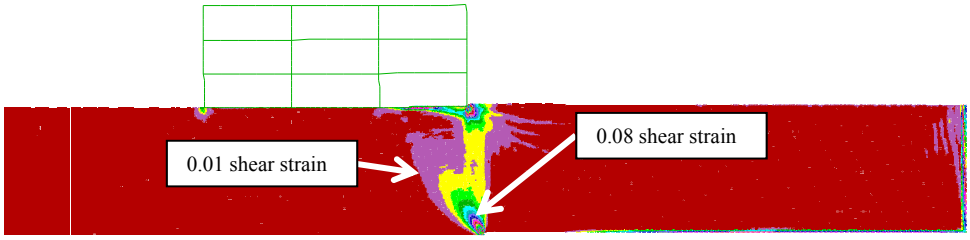

(b)

Figure 6-14. Comparison of structural response for the three-story structure shifted 3 m to the right in comparison to Figure 6-7: (a) pseudostatic analysis; and (b) dynamic analysis (v_{ave} = 0.8 m/s). Shear strain is plotted in contours of 0.01 shear strain.

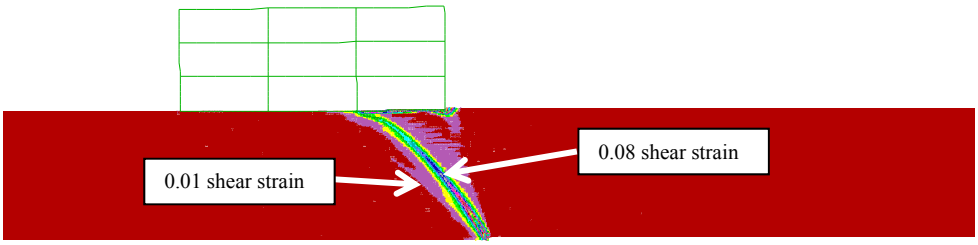

(a)

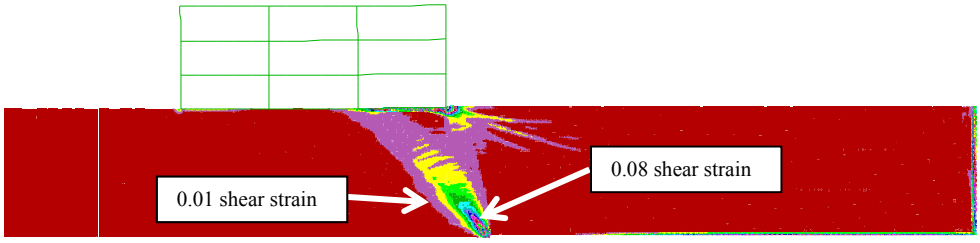

(b)

Figure 6-15. Comparison of structural response for dense sand ($N_{1,60}$=45): (a) pseudostatic analysis; and (b) dynamic analysis (v_{ave} = 0.8 m/s). Shear strain is plotted in contours of 0.01 shear strain.

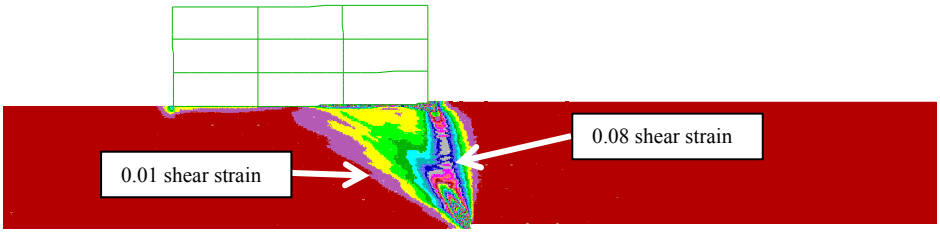

(a)

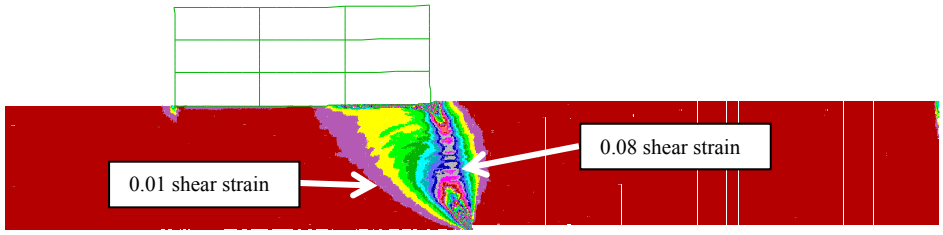

(b)

Figure 6-16. Comparison of structural response for 1 m of fault displacement: (a) pseudostatic analysis; and (b) dynamic analysis (v_{ave} = 0.8 m/s). Shear strain is plotted in contours of 0.01 shear strain.

CHAPTER 7: CONCLUSIONS

7.1 Summary

Recent earthquakes have provided examples of structures being damaged severely as a result of surface fault rupture. However, during these events, many structures have also performed well. A comprehensive study was completed to assess the damage expected in structures as a result of surface fault rupture. The problem was address as a soil–structure–fault interaction problem using an elasto-plastic effective-stress soil constitutive model. The results of these simulations were compared with an extensive set of centrifuge test results that often considered the effects of structures.

The developed model was compared and validated against the available experimental geotechnical centrifuge tests. Insights were developed into the aspects of soil response necessary to capture the response of soil over a bedrock fault displacement. Next fundamental aspects of the change in stress and state within the soil overlying a displaced bedrock fault were explored. This included the stress paths in various fault zones and the effects of prior ruptures on structural response. Potential geotechnical mitigation strategies were then assessed in a comprehensive framework. Novel and existing mitigation strategies were explored. Lastly, the potential effects of fault rupture dynamics were explored to evaluate how the rate of fault rupturing might affect building performance.

7.2 Findings

Finite difference simulations using the program FLAC with a modified soil constitutive model based on UBCSAND were employed to analyze soil–structure–fault interaction. The numerical simulations were able to capture well key trends observed in the experimental results. These key trends include an increased amount of fault diversion as the structural weight, an increased amount of fault diversion for stiff structures, fault propagation dependence on the location of the structure, and significant dependence on the width of the building. The centrifuge test results and the corresponding numerical simulation results show that structures can have a significant effect on the propagation of dip-slip fault rupture through engineered fill. In general, free-field test results were also matched well with experimental data in terms of the calculated ground deformation.

Therefore, the proposed finite-difference analysis technique using the modified UBCSAND constitutive model was judged to be reasonable. These findings are similar to those of previous researchers that demonstrated that nonlinear soil models with a well-defined failure strain and post-peak drop in shear strength can capture the key features of fault rupture propagation through previously unruptured soil. The validated numerical simulations were utilized to investigate various key aspects of the soil–structure–fault interaction problem.

A thorough examination of the primary modes of soil shearing during fault rupture and its effects on the soil deposit's stress state were studied. The numerical results demonstrate that the stress paths in the rupture zone are analogous to plane-strain extension (loading) and plane-strain compression (unloading) element tests for reverse and normal faults, respectively. The stress paths in vertical faults were found to be similar to a simple shear mode. In all cases, the state of

stress in the fault rupture zone and the surrounding region were found to have evolved after the occurrence of bedrock fault ruptures, and distinct shear bands were formed during fault rupture if the soil was dilatant.

Although previous researchers have studied how surface fault rupture might affect structures, the potential effects of prior fault ruptures through the underlying soil deposit have not been investigated. Given that faults typically rupture multiple times in a semi-periodic manner and given that soil response is affected by stress history and by the formation of shear bands, the potential effects of prior earthquake fault ruptures on fault rupture interaction with structures warranted investigation. Therefore, the effect of prior fault ruptures on soil response and structural damage was assessed using the developed numerical framework.

The soil response to underlying bedrock fault rupture occurs in two distinct stages. First, broad deformation occurs before strain localization, which is followed by more localized deformation after shear band formation. Given the potential for prior fault ruptures, the first stage of broad deformation may no longer occur for many dip-slip faults, or may occur to a lesser extent, during subsequent events. Ground deformation at sites with prior ruptures was found to be more localized (i.e., angular distortion was greater at the fault outcrop but lower away from the fault trace compared to previously unruptured soil). As a result, structural damage is more severe if the structure is located directly above the surface projection of the bedrock fault, but damage is less severe if the structure is located adjacent to the fault.

Thus, previous rupture events can significantly affect soil and structural responses to earthquake fault rupture. The effects of prior fault rupture events can be potentially detrimental or beneficial from the standpoint of structural performance in the near-fault vicinity. Therefore, the potential effects of prior fault ruptures need to be considered in evaluations of the response of structures to surface fault rupture when previous events have likely ruptured through an existing soil deposit.

Surface fault rupture can be damaging to structures built near active faults for both the case of prior fault rupture and the unruptured case. Therefore, geotechnical mitigation strategies for improving the performance of structures were examined. These strategies are categorized into three broad groups: (1) diffusing fault displacement over a large area; (2) causing the structure to respond with rigid-body movement; and (3) diverting the fault rupture. The effectiveness of each of these strategies can vary from protecting life safety to preventing significant damage and can be effective for a range of dip-slip fault movement.

Structural response was significantly improved using the fault movement diffusion strategy when the previously ruptured soil was replaced by ductile compacted earth fill, because the fault movement was spread over a wide zone in distributed shear. For the rigid-body rotation strategy, reinforced-concrete mat foundations mitigated effectively the surface fault rupture hazard. This strategy was effective for both reverse and normal faults for many site and structural conditions. Specifying a mat of at least minimal thickness may be prudent in areas where a fault zone is known to exist but is concealed or poorly defined and thus cannot be located with confidence. Thicker mat foundations provide superior performance and are recommended in areas where shallow active faults are known to exist.

Several fault diversion strategies proved effective at protecting structures from bedrock fault movement. These strategies are limited, however, to structures placed on one side of a bedrock fault, which should in most cases be the footwall side of a dip-slip fault. Thus, these

strategies are not as versatile as using a thick reinforced-concrete mat foundation or ductile compacted earth fills. These diversion strategies included ground improvement, diaphragm walls, and basements to "shield" a structure and concentrate shear strains adjacent to the building. Similarly, seismic gaps can be placed on the fault side of a structure to accommodate fault movement. Ground anchors can also hold structures down on the footwall side of reverse faults when the ground anchors are bonded well below the expected fault rupture plane.

Dynamic fault rupture effects in soil–structure–fault interaction have typically not been accounted for in most physical or numerical research on this subject. Yet, surface fault rupture typically occurs rapidly. The dynamic fault rupture has a minor to moderate effect on the expected free-field ground surface deformation. These effects, which occur at high slip velocities, include slightly modifying the propagation path of fault rupture through unruptured soil, especially for normal faults, and causing somewhat broader zones of soil strain.

A series of analyses were conducted to compare the expected performance of structures in the vicinity of a fault zone using pseudostatic and dynamic fault rupture analyses. For a structure placed on the footwall of a reverse fault, the amount of fault diversion increased moderately, and the corresponding maximum angular distortion decreased. For a structure placed on the hanging wall of a normal fault, the amount of fault diversion decreased slightly and a graben structure developed more distinctly, causing the calculated angular distortion to increase. However, for structures placed either on the footwall of a normal fault or on the hanging wall of a reverse fault, the amount of fault diversion and angular distortion was not significantly changed.

For dense sand, pre-ruptured conditions, and larger amounts of fault displacement, only negligible differences between dynamic and pseudostatic fault rupture analysis were observed. In each of these scenarios, failure conditions had been developed throughout the soil profile. This suggests that dynamic fault rupture effects are not significant enough to change the kinematic constraints of the problem, which develop when failure conditions are met.

The impact of considering dynamic fault rupture on the calculation of permanent ground deformation beneath a structure can be a moderate to significant effect for certain soil and structure conditions when a rapid fling-step fault-induced displacement is expected and when the geometry is optimized to promote dynamic-induced fault diversion. However, most realistic scenarios will have either less optimized fault and structure geometry, a higher level of fault displacement, developed soil failure conditions, or less significant fling-step ground motion. Therefore, dynamic fault rupture effects are a secondary concern for most scenarios. Dynamic fault rupture effects can, for the most part, be ignored when evaluating structural damage as a result of fault-induced ground deformation.

7.3 Future Research

One of the major research needs related to surface fault rupture is to expand the work completed herein to strike-slip faults. This would require the use of three-dimensional numerical analysis. Another limitation of this research is that it explored largely the response of dry sand deposits. Issues such as the potential effects of pore water pressure response of saturated soils on the response of structures during fault rupture were not addressed. Similarly, sites underlain by clay may have a different response to fault rupture due to differences in the way that soil strength is gained beneath a structure for cohesive versus cohesionless deposits. Assessment of the effects

of transient (strong motion) ground shaking on the calculated permanent ground deformation is also needed.

Structural-based mitigation methods may be feasible. Collaborations between geotechnical and structural engineers on developing appropriate structural mitigation strategies may be beneficial and provide additional design options. Ultimately, for mitigating surface fault rupture, field tests and case histories need to be developed and regulators need to be convinced that fault-ruptured mitigation strategies are safe. Extension of much of the work of this thesis, and similar work by other authors, should be extended to other types of non-building constructed systems which often must be sited in active fault zones. These systems include pipelines, bridges, railways, and tunnels.

Earth science research is required primarily in two areas: (1) very-near fault ground motions; and (2) off-fault deformation. Very-near fault motions have begun to be studied; however, without field recordings, a high degree of confidence in assumed ground motions cannot be obtained. Off-fault deformation is the broad distributed ground movement that can occur near primary fault breaks. Discerning off-fault deformation in trenches, and even during field reconnaissance, can be difficult. Yet it is important for certain sensitive structures located off of the primary fault strand. New techniques like aerial LIDAR offer promise to measure these types of movement. However, the somewhat sporadic development of secondary fault features makes this type of research complex. It is nevertheless an important topic in seismically active regions.

REFERENCES

Abelev, A.V., and Lade, P. V. (2003). "Effects of cross anisotropy on three-dimensional behavior of sand. I: Stress–strain behavior and shear banding." *Journal of Geotechnical and Geoenvironmental Engineering*, 129(2), 160–166.

Abrahamson, N.A. (2001). "Development of fling model for Diablo Canyon ISFSI." *Calc. No. GEO.DCPP.01.12*, Pacific Gas and Electric Company, Geosciences Department.

American Institute of Steel Construction (2005). "Steel construction manual." 13th Ed., AISC, Chicago.

Anastasopoulos I. (2009). "Closure to fault rupture propagation through sand: Finite-element analysis and validation through centrifuge experiments." *Journal of Geotechnical Engineering*, 133(8), 943–958.

Anastasopoulos I., and Gazetas G. (2007a). "Foundation-structure systems over a rupturing normal fault: Part I. Observations after the Kocaeli 1999 earthquake." *Bulletin of Earthquake Engineering*, 5(3), 253–275.

Anastasopoulos I., and Gazetas G. (2007b). "Behaviour of structure–foundation systems over a rupturing normal fault: Part II. Analysis of the Kocaeli case histories." *Bulletin of Earthquake Engineering*, 5(3). 277–301.

Anastasopoulos I., and Gazetas G. (2009). "Analysis of cut-and-cover tunnels against large tectonic deformation." *Bulletin of Earthquake Engineering*, 8(2).

Anastasopoulos I., Gazetas G., Bransby M.F., Davies M.C.R., and El Nahas A. (2007) "Fault rupture propagation through sand: Finite element analysis and validation through centrifuge experiments." *Journal of Geotechnical and Geoenvironmental Engineering*, 133(8), 943–958.

Anastasopoulos, I., Callerio, A., Bransby, M.F., Davies, M.C.R., El. Nahas, A., Faccioli, E., Gazetas, G., Masella, A., Paolucci, R., Pecker, A., Rossignol, E. (2008a). "Numerical analyses of fault–foundation interaction." *Bulletin of Earthquake Engineering*, 6(4), 645–675.

Anastasopoulos I., Gazetas G., Drosos V., Georgarakos T., and Kourkoulis R. (2008b). "Design of bridges against large tectonic deformation." *Earthquake Engineering and Engineering Vibration*, 7(4), 345–368.

Anastasopoulos I., Gerolymos N., Gazetas G., and Bransby M. F. (2008c). "Simplified approach for design of raft foundations against fault rupture. Part I: Free-field", *Earthquake Engineering and Engineering Vibration*, 7, 147–163.

Anastasopoulos I., Gerolymos N., Gazetas G., and Bransby M. F. (2008d), "Simplified approach for design of raft foundations against fault rupture. Part II: Soil–structure interaction." *Earthquake Engineering and Engineering Vibration*, 7, 165–179.

Anastasopoulos I., Gazetas G., Bransby M.F., Davies M.C.R., and El Nahas A. (2009), "Normal fault rupture interaction with strip foundations." *Journal of Geotechnical and Geoenvironmental Engineering*, 135(3), 359–370.

Athanasopoulos, G., (2009). "Discussion of "Fault rupture propagation through sand: Finite-element analysis and validation through centrifuge experiments" by I. Anastasopoulos, G.

Gazetas, M. F., Bransby, M. C. R. Davies, and A. El Nahas." *Journal of Geotechnical and Geoenvironmental Engineering,* 135(6), 844–850.

Athanasopoulos, G., Leonidou, E., and Pelekis, P. (2007). "Fault-rupture related hazard to engineered structures-parametric numerical analyses." *4th International Conference on Earthquake Geotechnical Engineering.*

Barrell, D.J.A., Litchfield, N.J., Townsend, D.B., Quigley, M., Van Dissen, R.J., Cosgrove, R., … Cox, S.C. (2011). "Strike-slip ground-surface rupture (Greendale Fault) associated with the 4 September 2010 Darfield earthquake, Canterbury, New Zealand." *Quarterly Journal of Engineering Geology and Hydrogeology,* 44, 283–291.

Berrill, J.B. (1983). "Two-dimensional analysis of the effect of fault rupture on buildings with shallow foundations." *Soil Dynamics and Earthquake Engineering,* 2(3), 156–160.

Boscardin, M.D., and Cording, E.J. (1989). "Building response to excavation-induced settlement." *Journal of Geotechnical Engineering,* 115(1), 1–21.

Boulanger, R.W. (2010). "A sand plasticity model for earthquake engineering applications." *Report number: UCD/CGM-10/01*. Davis: Center for Geotechnical Modeling, Department of Civil and Environmental Engineering, University of California.

Bransby, M.F., Davies, M.C.R., and El Nahas, A. (2008a). "Centrifuge modeling of normal fault–foundation interaction." *Bulletin of Earthquake Engineering*, 6(4), pp. 585–605.

Bransby, M.F., Davies, M.C.R., El Nahas, A., and Nagaoka, S. (2008b). "Centrifuge modeling of reverse fault–foundation interaction." *Bulletin of Earthquake Engineering*, 6(4), pp. 607–628.

Bray, J.D. (1989). "The effects of tectonic movements on stresses and deformations in earth embankments." Thesis. University of California, Berkeley.

Bray, J.D. (2001). "Developing mitigation measures for the hazards associated with earthquake surface fault rupture." *A Workshop on Seismic Fault-Induced Failures – Possible Remedies for Damage to Urban Facilities,* Japan Society for the Promotion of Science, 55–79.

Bray, J.D. (2009). "Designing buildings to accommodate earthquake surface fault rupture." *Improving the Seismic Performance of Existing and Other Structures*, ASCE, Reston, VA, 1269–1280.

Bray, J.D. and Kelson, K.I. (2006). "Observations of surface fault rupture from the 1906 earthquake in the context of current practice." *Earthquake Spectra*, 22(S2), S69–S89.

Bray, J.D., Seed, R.B., and Seed, H.B. (1992). "On the response of earth dams subjected to fault rupture." *Stability and Performance of Slopes and Embankments - II*, ASCE, Reston, VA, 608-624.

Bray, J. D., Ashmawy, A., Mukhopadhyay, G., and Gath, E. M. (1993). "Use of geosynthetics to mitigate earthquake fault rupture propagation through compacted fill." *Geosynthetics '93 Conference Proceedings,* Industrial Fabric Assn Intl, Roseville, MN, 379–392.

Bray, J.D., R.B., Seed, and H.B., Seed (1993). "1g small-scale modelling of saturated cohesive soils." *Geotechnical Testing Journal*, 16(1), 46–53.

Bray, J.D., R.B., Seed, L.S., Cluff, and H.B., Seed (1994a). "Earthquake fault rupture propagation through soil." *Journal of Geotechnical Engineering*, 120(3), 543–561.

Bray, J.D., R.B., Seed, and H.B., Seed (1994b). "Analysis of earthquake fault rupture propagation through cohesive soil." *Journal of Geotechnical Engineering*, 120(3), 562–580.

Bryant, W.A. (2012). "History of the Alquist-Priolo Earthquake Fault Zoning Act, California, USA." *Environmental & Engineering Geoscience,* 16(1), 7–18.

Byrne, P.M., Park, S.S., Beaty, M., Sharp, M.K., Gonzalez, L., and Abdoun, T. (2004). "Numerical modeling of liquefaction and comparison with centrifuge tests" *Canadian Geotechnical Journal,* 41(2), 193–211.

Canora, C., Martinez-Diaz, J.J., Villamor, P., Berryman, K., Alvarez-Comez, J.A., Pullinger, C., Capote, R. (2010). "Geological and seismological analysis of the 13 February 2001 M_w 6.6 El Salvador earthquake: Evidence for surface rupture and implications for seismic hazard." *Bulletin of the Seismological Society of America,* 100(6), 2873–2890.

Cluff, L.S., R.A. Page, D.B. Slemmons, and C.B. Crouse (2003). "Seismic hazard exposure for Trans-Alaska Pipeline." *Proc. 6th U.S. Conf. on Lifeline Earthquake Engineering*, ASCE, Reston, VA.

Cole, D.A., Jr. and Lade, P.V. (1984). "Influence zones in alluvium over dip-slip faults." *Journal of Geotechnical Engineering,* 110(5), 599–615.

Department of Conservation Resources Agency (2009). "A survey of lead agencies affected by the Alquist-Priolo earthquake fault zoning act." *SMGB Information Report 2009-06*, Department of Conservation Resources Agency, Sacramento, CA.

Dong, J.J., Wang, C.D., Lee, C.T., Liao, J.J., Pan, Y.W. (2003). "The influence of surface ruptures on building damage in the 1999 Chi-Chi earthquake: A case study in Fengyuan City." *Engineering Geology,* 71, 157–179.

Dreger, D., Hurtado, G., Chopra, A., and Larsen, S. (2011). "Near-field across-fault seismic ground motions." *Bulletin of the Seismological Society of America*, 101(1), 202–221.

Du, Y., Xie, F., and Wang, Z. (2012). "Wenchuan earthquake surface fault rupture and disaster: A lesson on seismic hazard assessment and mitigation." *International Journal of Geophysics,* 2012.

Duffy, B., Quigley, M., Barrell, D.J.A., Van Dissen, R., Stahl, T., Leprince, S., … McInnes, C. (2013). "Fault kinematics and surface deformation across a releasing bend during the 2010 M_w 7.1 Darfield, New Zealand, earthquake revealed by differential LiDAR and cadastral surveying." *GSA Bulletin,* 125(3/4), 420–431.

Duncan, J.M., and Lefebvre, G. (1973). "Earth pressures on structures due to fault movement." *Journal of the Soil Mechanics and Foundations Division*, 99(12), 1153–1163.

Duncan, J.M., Byrne, P., Wong, K.S., and Mabry, P. (1980). "Strength, stress-strain and bulk modulus parameters for finite element analyses of stresses and movements in soil masses." *Report No. UCB/GT/80-01,* University of California, Berkeley, California.

Faccioli, E., Anastasopoulos, I., Callerio, A., and Gazetas, G. (2008). "Case histories of fault–foundation interaction." *Bulletin of Earthquake Engineering*, 6(4), 557–583.

Fialko, Y., Sandwell, D., Agnew, D., Simons, M., Shearer, P., Minster, B. (2002). "Deformation on nearby faults induced by the 1999 Hector Mine Earthquake." *Science,* 297. 1858–1862.

Fraser, J.G., Hubert-Ferrari, A., Verbeeck, K., Garcia-Moreno, D., Avsar, U., Maricq, N., Coudijzer, A., Vlamynck, N., and Vanneste, K. (2012). "A 3000-year record of surface-rupturing earthquakes at Gunalan: variable fault-rupture lengths along the 1939 Erzincan earthquake-rupture segment of the North Anatolian Fault, Turkey." *Annals of Geophysics,*55(5), 895–927.

Gasperini, L., Polonia, A., Bortoluzzi, G., Henry, P., Le Pichon, X., Tryon, M., … Geli, L. (2011). "How far did the surface rupture of the 1999 Izmit earthquake reach in Sea of Marmara?" *Tectonics,* 30.

Gazetas G., Pecker A., Faccioli E., Paolucci R., and Anastasopoulos I. (2008). "Design recommendations for fault–foundation interaction." *Bulletin of Earthquake Engineering*, 6(4), 677–687.

GEER (1999). "Preliminary geotechnical earthquake engineering observations of the September 21, 1999, Ji-Ji, Taiwan earthquake" Geotechnical Extreme Events Reconnaissance (GEER) Association, Berkeley, CA.

GEER (2010). "Preliminary report on seismological and geotechnical engineering aspects of the April 4 2010 M_w 7.2 El Mayor-Cucapah (Mexico) earthquake." *Report GEER-023*, Geotechnical Extreme Events Reconnaissance (GEER) Association, Berkeley, CA.

GEER (2011). "Preliminary observation of surface fault rupture from the April 11, 2011 M_w 6.6 Hamadoori earthquake, Japan." *Report GEER-025*, Geotechnical Extreme Events Reconnaissance (GEER) Association, Berkeley, CA.

Goel, R.K., and Chopra, A.K. (2009a). "Linear analysis of ordinary bridges crossing fault-rupture zones." *Journal of Bridge Engineering*, 14(3), 203–215.

Goel, R.K., and Chopra, A.K. (2009b). "Nonlinear analysis of ordinary bridges crossing fault-rupture zones." *Journal of Bridge Engineering*, 14(3), 216–224.

Graves, R. W., and Pitarka, A. (2010). "Broadband ground-motion simulation using a hybrid approach." *Bulletin of the Seismological Society of America*, 100(5A), 2095–2123.

Guerrieri, L., Baer, G., Hamiel, Y., Amit, R., Blumetti, A.M., Comerci, V., … Vittori, E. (2010). "InSAR data as a field guide for mapping minor earthquake surface ruptures: Ground displacements along the Paganica Fault during the 6 April 2009 L'Aquila earthquake." *Journal of geophysical Research,* 115.

Gursoy, H., Tatar, O., Akpinar, Z., Polat, A., Mesci, L., and Tuncer, D. (2010). "New observations on the 1939 Erzincan earthquake surface rupture on the Kelkit Valley segment of the North Anatolian Fault Zone, Turkey." *Journal of Geodynamics,* 65(1), 259–271.

Ha, D., Adboun, T.H., O'Rourke, M.J., Symans, M.D., O'Rourke, T.D., Palmer, M.C., and Stewart. H.E. (2008). "Centrifuge modeling of earthquake effects on buried high-density polyethylene (HDPE) pipelines crossing fault zones." *Journal of Geotechnical Engineering*, 134(10), 1501–1515.

Itasca (2008). FLAC – Fast Lagrangian Analysis of Continua, Version 6.0. Itasca Consulting Group, Minneapolis, MN.

Jacques, E., Kidane, T., Tapponnier, P., Manighetti, I., Gaudemer, Y., Meyer, B., Ruegg, J.C., Audin, L., and Armijo, R. (2011). "Normal faulting during the August 1989 earthquakes in Central Afar: Sequential triggering and propagation of rupture along the Dobi Graben." *Bulletin of the Seismological Society of America,* 101(3), 994–1023.

Johansson, J., and Konagai, K. (2006). "Fault induced permanent ground deformation – an experimental comparison of wet and dry soil and implications for buried structures." *Soil Dynamics and Earthquake Engineering*. 26(1), 45–63.

Kagawa, T., Irikura, K., Somerville, P. G. (2004). "Differences in ground motion and fault rupture process between the surface and buried rupture earthquakes." *Earth Planets Space*, 56(1), 3–14.

Kalkan, E., and Kunnath, S.K. (2006). "Effects of fling step and forward directivity on seismic response of buildings." *Earthquake Spectra,* 22(2), 367–390.

Kelson, K., Bray, J., Cluff, L., Harder, L., Kieffer, S., Lettis, W., … Yashinsky, M. (2001a). "Fault-related surface deformation." *Earthquake Spectra,* 17(S1), 19–36.

Kelson, K., Kang, K.-H., Page, W.D., Lee, C.-T., and Cluff, L.S. (2001b). "Representative styles of deformation along the Chelungpu Fault from the 1999 Chi-Chi (Taiwan) earthquake: Geomorphic characteristics and responses of man-made structures." *Bulletin of the Seismological Society of America,* 91(5), 930–952.

Kelson, K.I., Konagai, K., Bray, J., Ryder, I., Streig, A., Harder, L., and Kishida, T. (2012). "Onshore surface fault rupture and crustal deformation from the April 11, 2011 M_w 6.6 Hamadoori earthquake, Japan." *Annual Meeting of the Seismological Society of America,* Poster.

Koehler, R.D., Personius, S.F., Schwarz, D.P., Haeussler, P.J. and Seitz, G.G. (2011). "A paleoseismic study along the Central Denali Fault, Chistochina Glacier Area, South-Central Alaska." *Division of Geological & Geophysical Surveys,* Report of Investigation 2011-1, State of Alaska.

Koerner, G.R., and Narejo, D. (2005). "Direct shear database of geosynthetic-to-geosynthetic and geosynthetic-to-soil interfaces." *Geosynthetic Research Institute Report #30*, Folsom, Pennsylvania.

Konagai, K. (2005). "Data archives of seismic fault-induced damage." *Soil Dynamics and Earthquake Engineering,* 25(7–10), 559–570.

Kratzsch, H. (1983). "Mining Subsidence Engineering." Springer Verlag, Berlin.

Lade, P. V., and Abelev, A.V. (2003). "Effects of cross anisotropy on three-dimensional behavior of sand. II: Volume change behavior and failure." *Journal of Geotechnical and Geoenvironmental Engineering*, 129(2), 167–174.

Lade, P. V., and Cole, D. A., Jr. (1984). "Influence zones in alluvium over dip-slip faults." *Journal of Geotechnical Engineering*, 110(5), 599–615.

Lade, P.V., and Ibsen, L.B. (1997). "A study of the phase transformation and the characteristic lines of sand behavior." *Soil Mechanics Paper No 12,* Geotechnical Engineering Group Aalborg, University Denmark.

Lade, P.V., Nam, J., and Liggio, C.D. (2010). "Effects of particle crushing in stress drop-relaxation experiments on crushed coral sand." *Journal of Geotechnical and Geoenvironmental Engineering,* 136(3), 500–509.

Lazarte, C.A. (1996). "The response of earth structures to surface fault rupture." Thesis. University of California, Berkeley.

Lazarte, C.A, Bray, J.D., Johnson, A.M., and Lemmer, R.E. (1994). "Surface breakage of the 1992 Landers earthquake and its effects on structures." *Bulletin of the Seismological Society of America,* 84(3), 547–561.

Lee, S-S., Goel, S.C., and Chao, S-H. (2004). "Performance-based seismic design of steel moment frames using target drift and yield mechanism." *13th World Conference on Earthquake Engineering*.

Lettis, W., Bachhuber, J., Barka, A., Brankman, C., Lettis, W., Somerville, P., and Witter, R. (2000a). "Geology and seismicity." *Earthquake Spectra*, 16(S1), 1–9.

Lettis, W., Bachhuber, J., Witter, R., Bachhuber, J., Barka, A., Bray, J., … Cakir, Z. (2000b). "Surface fault rupture." *Earthquake Spectra*, 16(S1), 11–53.

Lettis, W., Bachhuber, J., Witter, R., Brankman, C., Randolph, C.E., Barka, A., … Kaya, A. (2002). "Influence of releasing step-overs on surface fault rupture and fault segmentation: Examples from the 17 August 1999 Izmit Earthquake on the North Anatolian Fault, Turkey." *Bulletin of the Seismological Society of America*, 92(1), 19–42.

Lienkaemper, J.J., Baker, B., and McFarland, F.S. (2006). "Surface slip associated with the 2004 Parkfield, California, earthquake measured on alinement arrays." *Bulletin of the Seismological Society of America,* 96(4B), S239–S249.

Lin, A., Rao, G., Jia, D., Wu, X., Yan, B., and Ren, Z. (2011). "Co-seismic strike-slip surface rupture and displacement produced by the 2010 M_w 6.9 Yushu earthquake, China, and implications for Tibetan tectonics." *Journal of Geodynamics,* 52, 249–259.

Loli, M., Anastasopoulos, I., Bransby, M.F., Ahmed, W., and Gazetas, G. (2011). "Caisson foundations subjected to reverse fault rupture: centrifuge testing and numerical analysis." *Journal of Geotechnical and Geoenvironmental Engineering,* 137(10), 914–925.

Loli, M., Bransby, M.F., Anastasopoulos, I., and Gazetas, G. (2012). "Interaction of caisson foundations with a seismically rupturing normal fault: centrifuge testing versus numerical simulation." *Geotechnique,* 62(1), 29–43.

Loukidis, D., Bouckovalas, G.D., and Papadimitriou, A.G. (2009). "Analysis of fault rupture propagation through uniform soil cover*." Soil Dynamics and Earthquake Engineering*. 29, 1389-1404.

Mu, C.-H., Angelier, J., Lee, J.-C., Chu, H.-T., and Dong, J.-J. (2011). "Structure and Holocene evolution of an active creeping thrust fault: The Chihshang fault at Chinyuan (Taiwan)." *Journal of Structural Geology,* 33, 743–755.

Murbach, D., Rockwell, T.K., and Bray, J.D. (1999). "The relationship of foundation deformation to surface and near-surface faulting resulting from the 1992 Landers earthquake." *Earthquake Spectra*. 15, 121–144.

Namikawa, T., and Mihira, S. (2007). "Elasto-plastic model for cement-treated sand." *International Journal for Numerical and Analytical Methods in Geomechanics,* 31(1), 71–107.

Niccum, M.R., Cluff, L.S., Chamorro, F., and Wyllie, L. (1976). "Banco Central de Nicaragua: A case history of a high-rise building that survived surface fault rupture." *Engineering Geology and Soils Engineering Symposium No. 4*, Idaho Transportation Department, Division of Highways, Boise, ID, 133–144.

Nikolinakou, M.A., Whittle, A.J., Savidis, S., and Schran, U. (2011). "Prediction and interpretation of the performance of a deep excavation in Berlin sand." *Journal of Geotechnical and Geoenvironmental Engineering,* 137(11), 1047–1061.

Oettle, N.K., and Bray, J.D. (2012). "Soil shearing during earthquake surface fault rupture." *15th World Conference on Earthquake Engineering*.

Oettle, N.K., and Bray, J.D. (2013a). "Fault rupture propagation through previously ruptured soil." *Journal of Geotechnical and Geoenvironmental Engineering*, in press.

Oettle, N.K., and Bray, J.D. (2013b). "Geotechnical mitigation strategies for earthquake surface fault rupture." *Journal of Geotechnical and Geoenvironmental Engineering*, in press.

Oettle, N.K., Bray, J.D., Konagai, K., and Kelson, K. (2013). "Surface fault rupture through a ridge in an aftershock of the 2011 Tohoku earthquake." *GeoCongress 2013,* ASCE, Reston, VA, 1574–1577.

Olsen, K. B., Day, S. M., Minster, J. B., Cui, Y., Chourasia, A., Okaya, D., Maechling, P., and Jordan, T. (2008). "TeraShake2: Spontaneous rupture simulations of Mw 7.7 earthquakes on the Southern San Andreas Fault." *Bulletin of the Seismological Society of America*, 98(3), 1162–1185.

Oskin, M.E., Arrowsmith, J.R., Hinojosa, A., Elliott, A.J., Fletcher, J.M., Fielding, E.J., … Teran, O.J. (2012). "Near-field deformation from the El Mayor-Cucapah earthquake revealed by differential LIDAR." *Nature,* 335, 702–705.

Park, S.W., Chasemi, H., Shen, J., Somerville, P.G., Yen, W.P., and Yashinsky, M. (2004). "Simulation of the seismic performance of the Bolu Viaduct subjected to near-fault ground motions." *Earthquake Engineering and Structural Dynamics,* 33, 1249–1270.

Priestley, M.J.N., and Calvi, G.M. (2002). "Strategies for repair and seismic upgrading of Bolu Viaduct 1, Turkey." *Journal of Earthquake Engineering*, 6(S1), 157–184.

Puebla, H., Byrne, P. M., and Philips, R. (1997) "Analysis of CANLEX liquefaction embankments: Prototype and centrifuge models," Canadian Geotechnical Journal, 34(5), 641-657.

Quigley, M., Van Dissen, R., Litchfield, N. Villamor, P., Duffy, B., Barrell, D., … Noble, D. (2012). "Surface rupture during the 2010 M_w 7.1 Darfield (Canterbury) earthquake: Implications for fault rupture dynamics and seismic-hazard analysis." *Geology,* 40, 55–58

Ran, Y., Shi, X., Wang, H., Chen, L., Chen, J., Liu, R., and Gong, H. (2010). "The maximum coseismic vertical surface displacement and surface deformation pattern accompanying the M_s 8.0 Wenchuan earthquake." *Chinese Science Bulletin,* 55(9), 841–850.

Roth, W.H., Scott R.F., and Austin, L. (1981). "Centrifuge modeling of fault propagation through alluvial soils." *Geophysical Research Letters*, 8(6), 561–564.

Scott R.F. (1983). "Centrifuge model testing at Caltech." *Soil Dynamics and Earthquake Engineering*, 2(4), 188–198.

Sibson, R.H. (1997). "Fault rocks and fault mechanisms." *Journal of the Geological Society of London,* 133(3), 191–213.

Simo, J.C., Oliver, J., and Armero, F. (1993). "An analysis of strong discontinuities induced by strains-softening in rate-independent inelastic solids." *Computational Mechanics,* 12(5), 277–296.

Somerville, P. G., Irikura, K., Graves, R., Sawada, S., Wald, D., Abrahamson, N., Iwasaki, Y., Kagawa, T., Smith, N., and Kowada, A. (1999). "Characterizing crustal earthquake slip models for the prediction of strong ground motion." *Seismological Research Letters*, 70(1), 59–80.

Son, M. and Cording, E.J. (2005). "Estimation of building damage due to excavation-induced ground movements." *Journal of Geotechnical and Geoenvironmental Engineering,* 131(2), 162–177.

Sorensen, S.P., and Meyer, K.J. (2003). "Effect of the Denali Fault rupture on the Trans-Alaska Pipeline." *Sixth U.S. Conference and Workshop on Lifeline Earthquake Engineering,* ASCE, Reston, VA.

Tobita, M., Nishimura, T., Kobayashi, T., Hao, K.X., and Shindo, Y. (2011). "Estimation of coseismic deformation and a fault model of the 2010 Yushu earthquake using PALSAR interferometry data." *Earth and Planetary Science Letters,* 307, 430–438.

Toda, S., and Tsutsumi, H. (2013). "Simultaneous reactivation of two, subparallel, inland normal faults during the M_w 6.6 11 April 2011 Iwaki earthquake triggered by the M_w 9.0 Tohoku-oki, Japan, Earthquake." *Bulletin of the Seismological Society of America,* 103(2B), 1584–1602.

Ulusay, R., Aydan, O., Hamada, M. (2001). "The behavior of structures built on active fault zones: Examples from the recent earthquakes of Turkey." *1st Workshop on Seismic Fault-Induced Failures,* University of Tokyo, 1–26.

Van Dissen, R., Barrell, D., Litchfield, N. Villamor, P., Quigley, M., King, A., … Mote, T. (2011). "Surface rupture displacement on the Greendale Fault during the M_w 7.1 Darfield (Canterbury) earthquake , New Zealand, and its impact on man-made structures." *Proceedings of the Ninth Pacific Conference on Earthquake Engineering,* NZSEE.

Van Dissen, R., Hornblow, S., Quigley, M., Litchfield, N., Villamor, P., Nicol, A., Barrell, D., Sasnett, P., and Newton, K. (2013). "Towards the development of design curves for characterizing distributed strike-slip surface fault rupture displacement: an example from the 4 September, 2010, Greendale Fault rupture, New Zealand" *Proceedings of the 19th NZGS Geotechnical Symposium*, NZGS.

Vidale, J.E., and Li, Y.-G. (2003). "Damage to the shallow Landers fault from the nearby Hector Mine earthquake." *Nature,* 421, 524–526.

Vignos, R., Walters, M., Bomba, G., and Friedman, D. (2009). "UC Berkeley's California Memorial Stadium seismic strengthening of an historic structure residing over an active fault." *Conference on Improving the Seismic Performance of Existing Buildings and Other Structures,* ASCE, Reston, VA, 1295–1304.

Villamor, P., Litchfield, N., Barrell, D., Van Dissen, R., Hornblow, S., Quigley, M., … Grant, H. (2012). "Map of the 2010 Greendale Fault surface rupture, Canterbury, New Zealand: application to land use planning." *New Zealand Journal of Geology and Geophysics*, 55(3), 223–230.

Wood, D.M. (1990). "Soil behavior and critical state soil mechanics," Cambridge University Press.

Zhou, Q., Xu, X., Yu, G., Chen, X., He, H., Yin, G. (2010). "Width distribution of the surface ruptures associated with the Wenchuan earthquake: Implication for the setback zone of the seismogenic faults in postquake reconstruction." *Bulletin of the Seismological Society of America,* 100(5B), 2660–2668.

APPENDIX A: Additional Validation Results

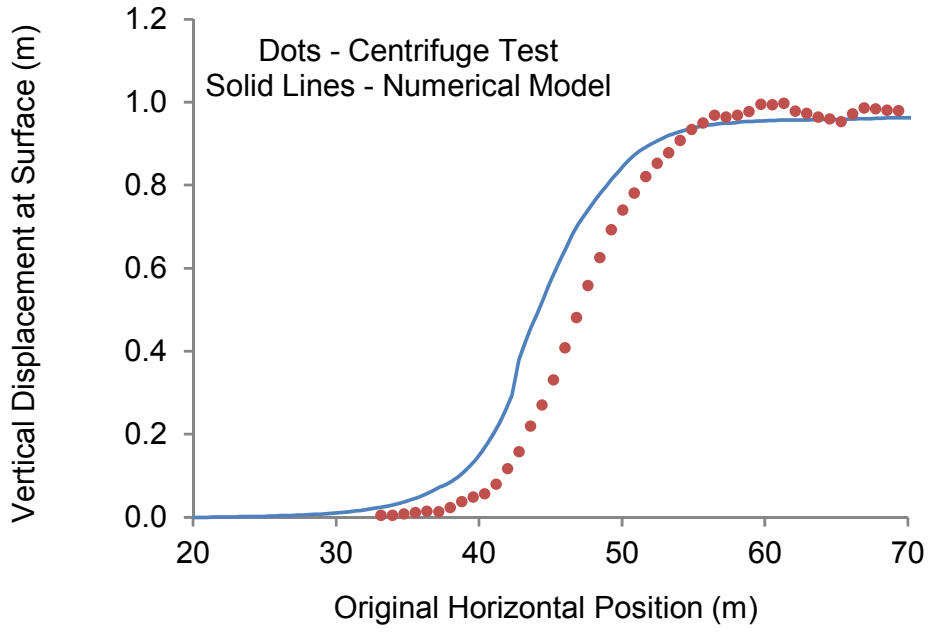

(a)

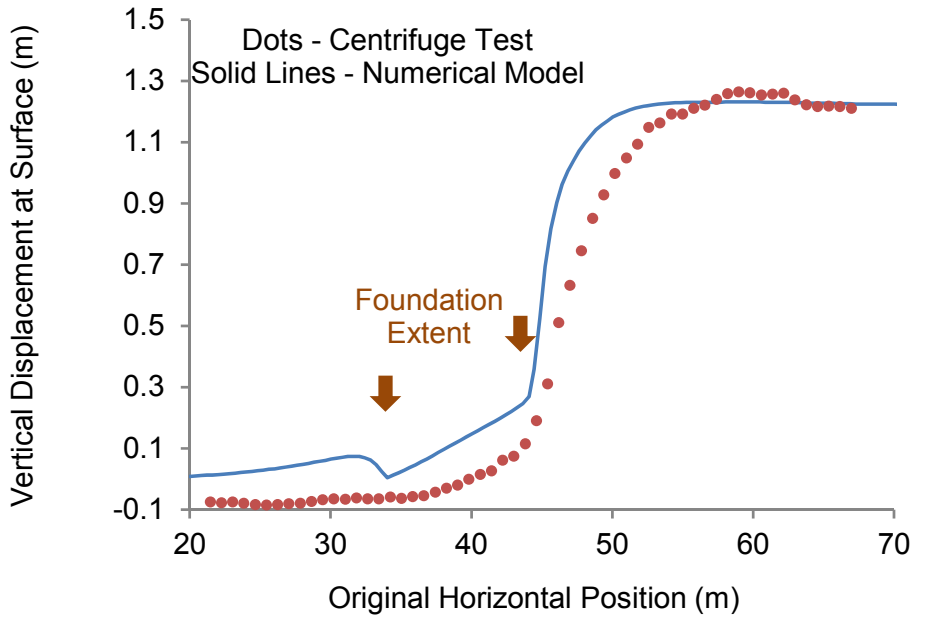

(b)

Figure A-1. Comparison of free-field response and response with a structure for a reverse fault (a) Test 28 (free field); and (b) Test 29 (with structure).

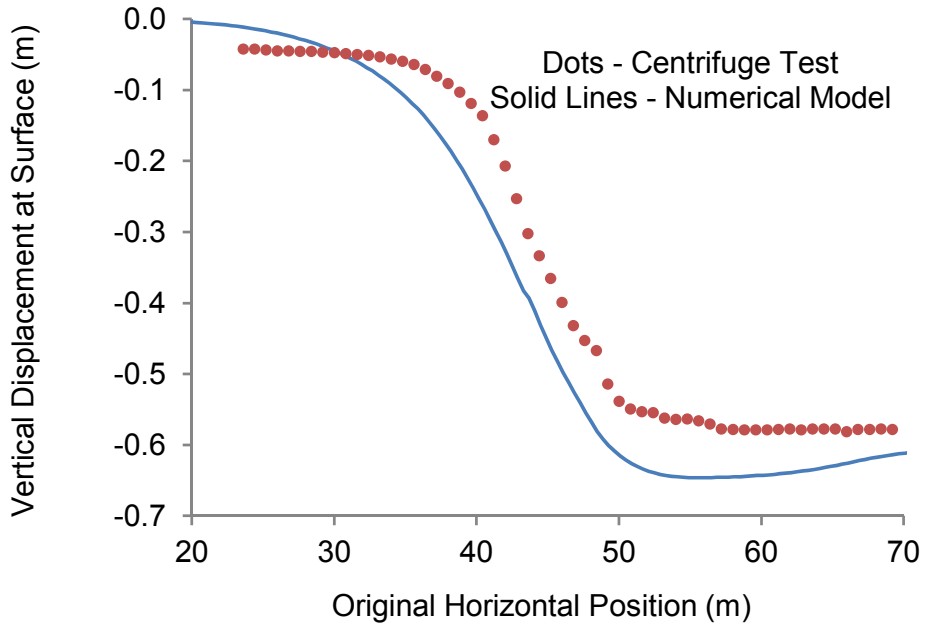

(a)

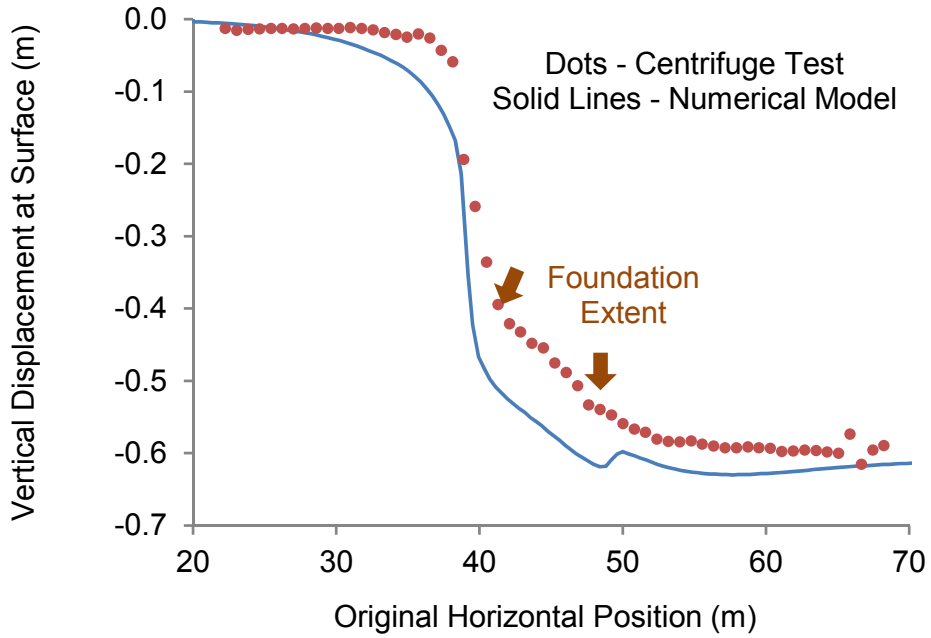

(b)

Figure A-2. Comparison of free-field response and response with a structure for a normal fault (a) Test 12 (free field); and (b) Test 14 (with structure).

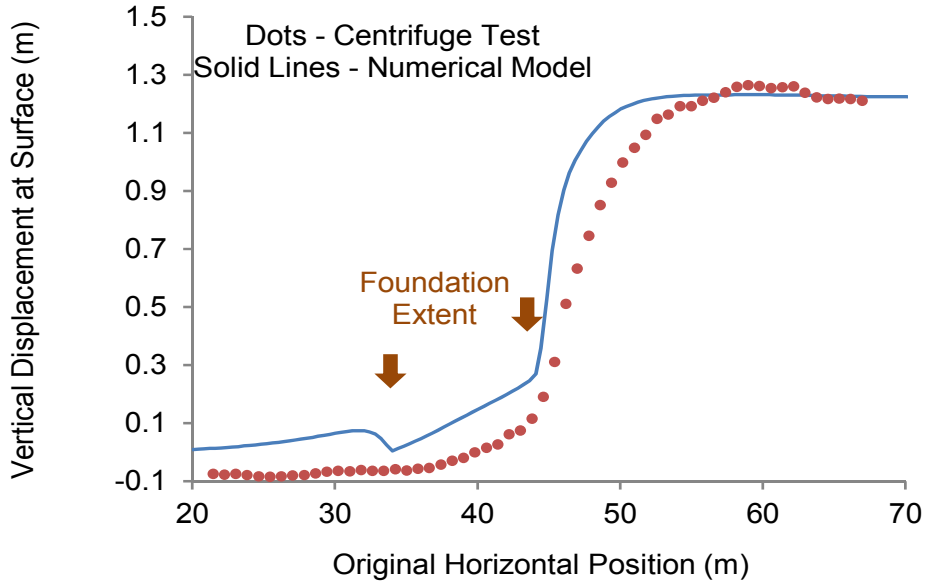

(a)

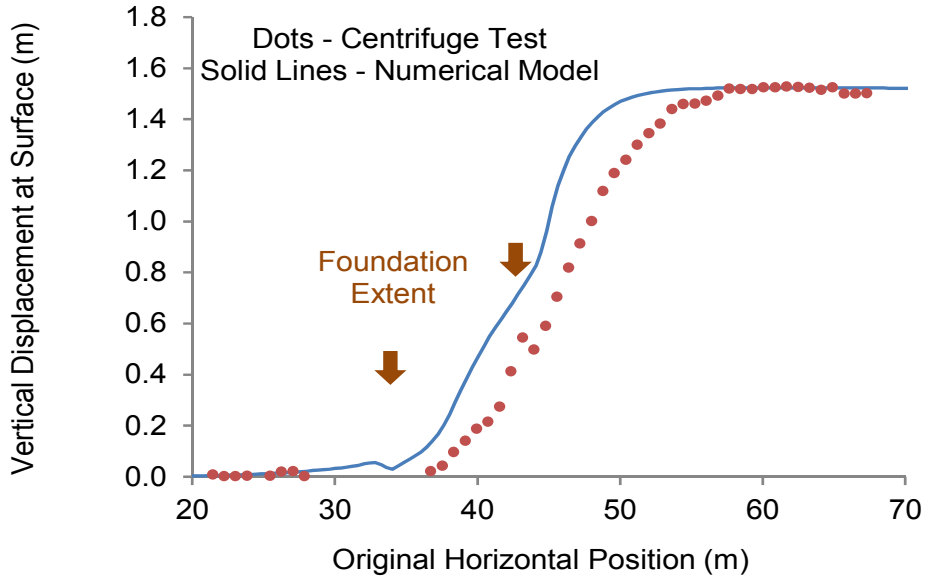

(b)

Figure A-3. Comparison of response with a reference structure and a lighter structure for a reverse fault (a) Test 29 (reference structural configuration: 91 kPa); and (b) Test 30 (light structure: 37 kPa).

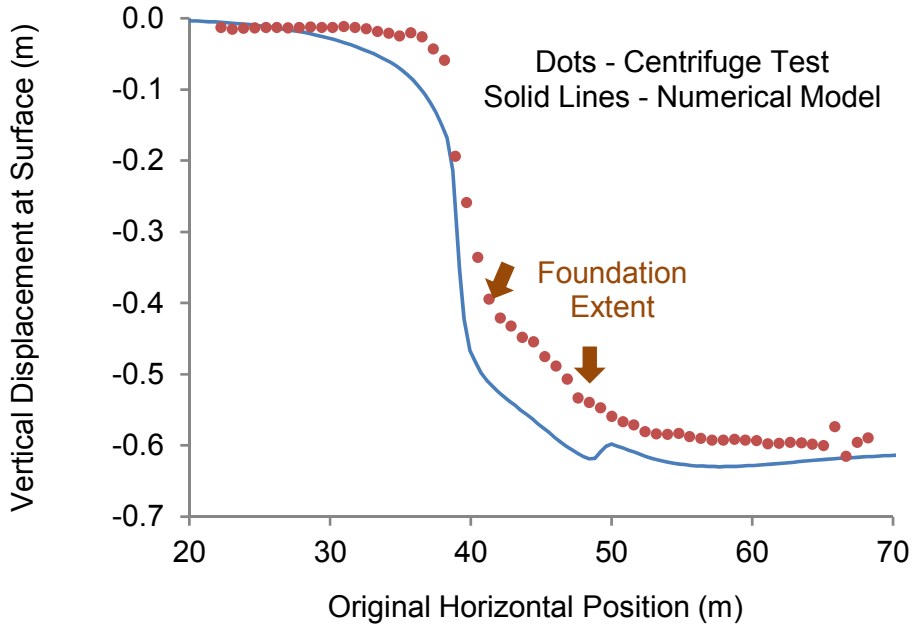

(a)

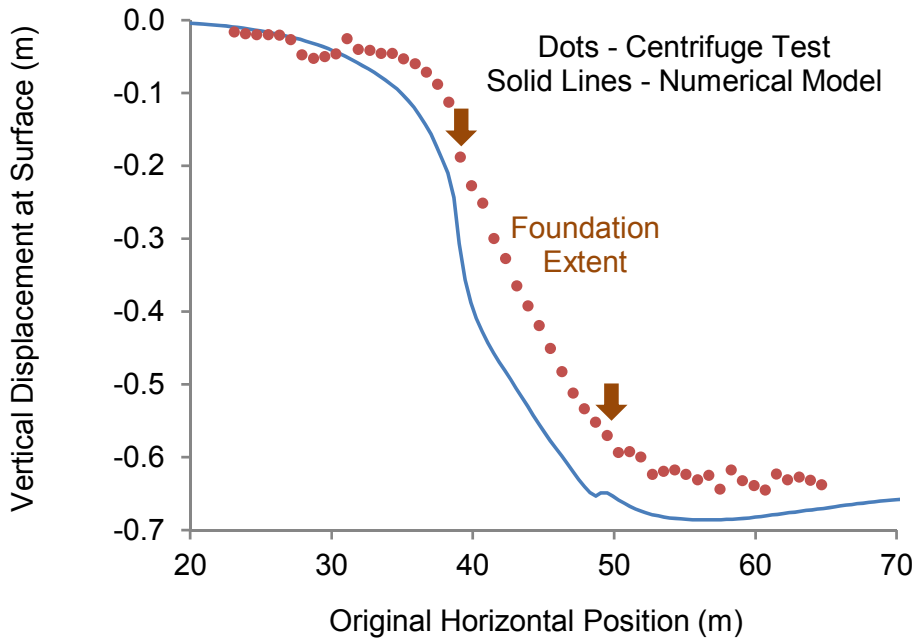

(b)

Figure A-4. Comparison of response with a reference structure and a lighter structure for a normal fault (a) Test 14 (reference structural configuration: 91 kPa); and (b) Test 15 (light structure: 37 kPa).

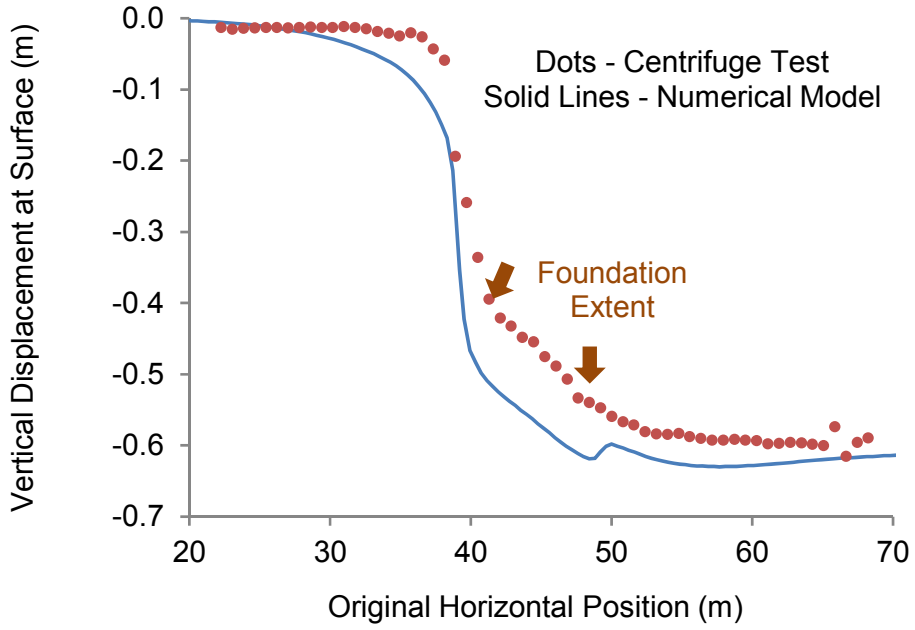

(a)

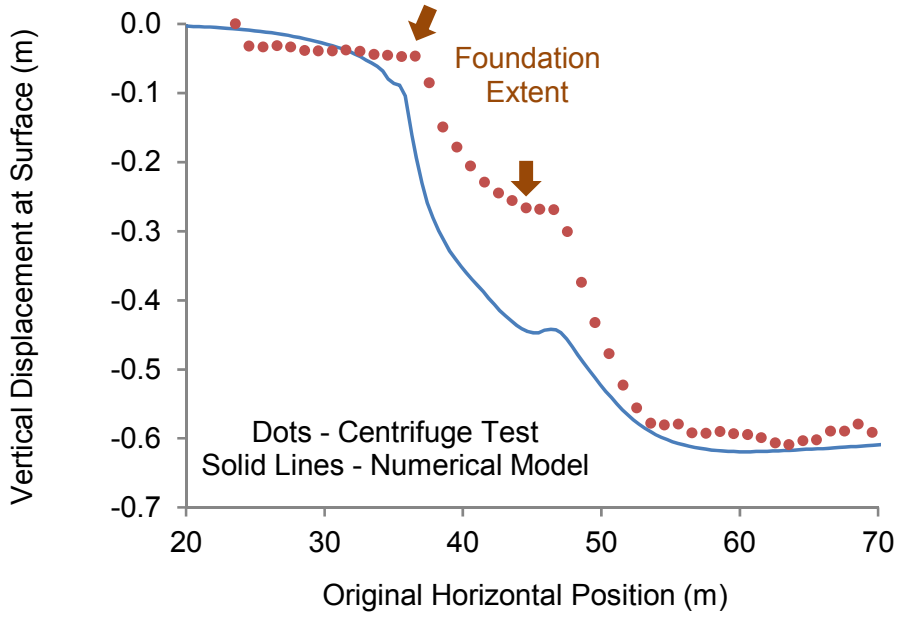

(b)

Figure A-5. Comparison of response with a reference structure and a structure moved 5 m to the left for a normal fault (a) Test 14 (reference structural configuration); and (b) Test 18 (structure moved 5 m to the left).

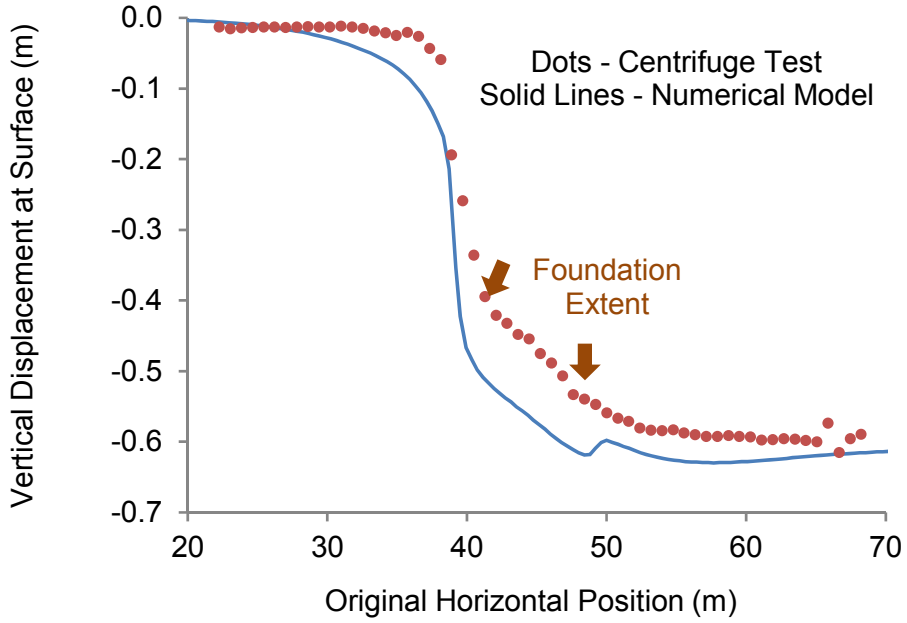

(a)

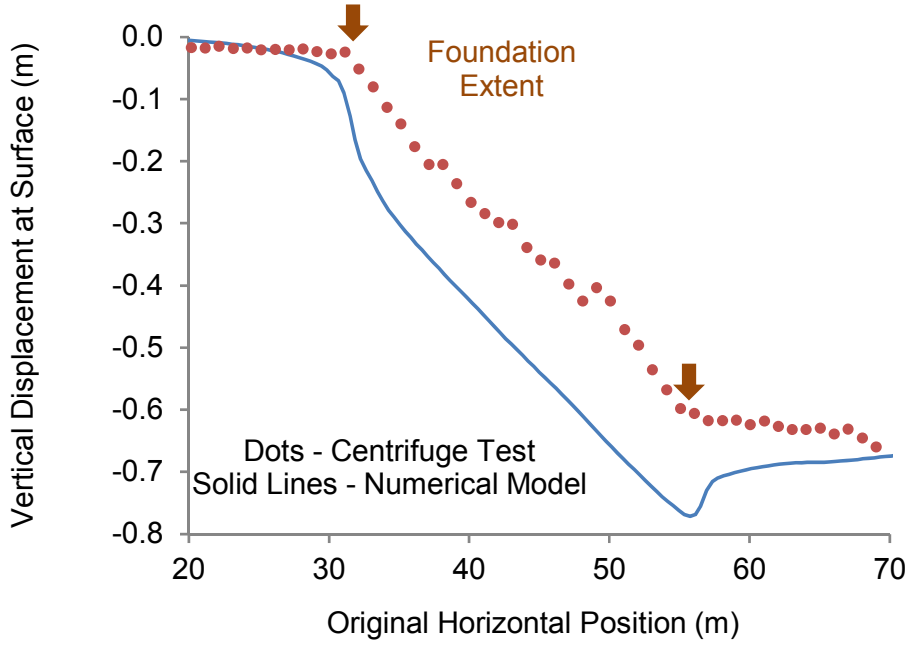

(b)

Figure A-6. Comparison of response with a reference structure and a structure with a wider foundation for a normal fault (a) Test 14 (reference structural configuration: 10 m wide foundation); and (b) Test 20 (25 m wide foundation).

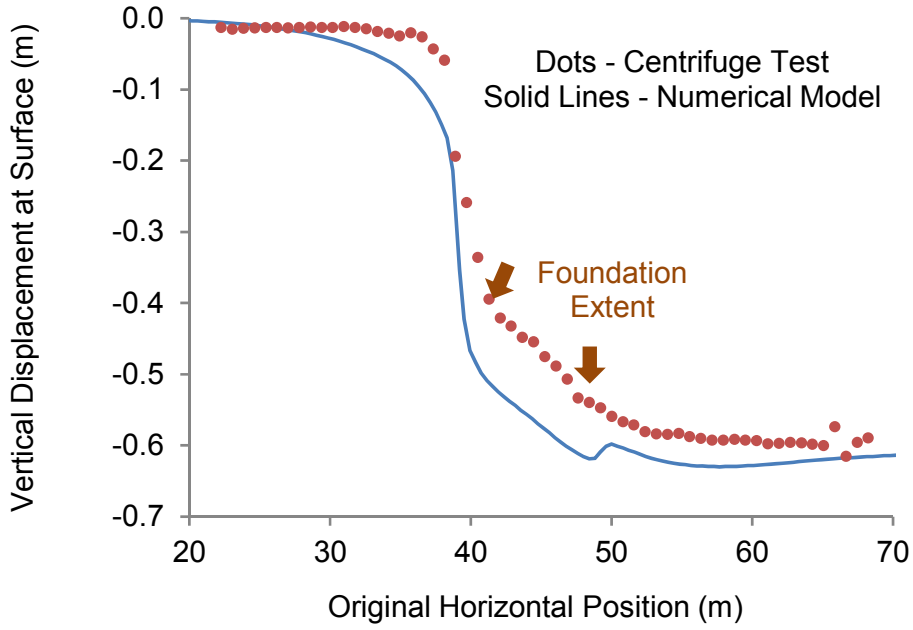

(a)

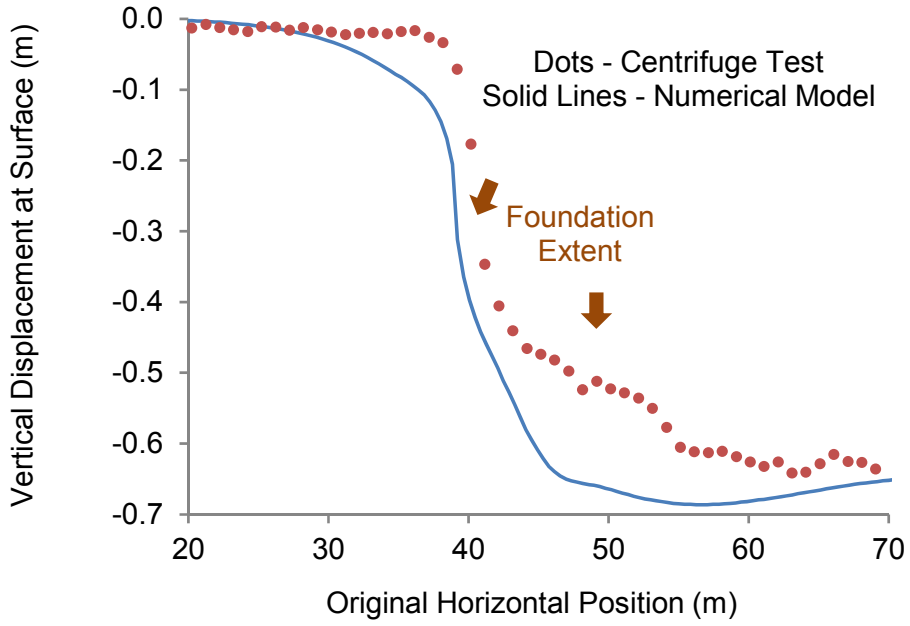

(b)

Figure A-7. Comparison of response with a reference structure and a structure with a more flexible foundation for a normal fault (a) Test 14 (reference structural configuration that has a mostly rigid foundation); and (b) Test 22 (structure with a mostly flexible foundation).